



HAL
open science

Construction and Validation of a Statistical 3D Atlas of Human Carpal Bones

Emilie Buessler

► **To cite this version:**

Emilie Buessler. Construction and Validation of a Statistical 3D Atlas of Human Carpal Bones. Geometric Topology [math.GT]. Université Grenoble Alpes, 2019. English. NNT : 2019GREAM060 . tel-02950975

HAL Id: tel-02950975

<https://theses.hal.science/tel-02950975>

Submitted on 28 Sep 2020

HAL is a multi-disciplinary open access archive for the deposit and dissemination of scientific research documents, whether they are published or not. The documents may come from teaching and research institutions in France or abroad, or from public or private research centers.

L'archive ouverte pluridisciplinaire **HAL**, est destinée au dépôt et à la diffusion de documents scientifiques de niveau recherche, publiés ou non, émanant des établissements d'enseignement et de recherche français ou étrangers, des laboratoires publics ou privés.

THÈSE

Pour obtenir le grade de

DOCTEUR DE LA COMMUNAUTÉ UNIVERSITÉ GRENOBLE ALPES

Spécialité : Mathématiques et Informatique

Arrêté ministériel : 25 mai 2016

Présentée par

Emilie BUESSLER

Thèse dirigée par **Lionel REVERET**, CR
et codirigée par **Franck QUAINÉ**, Université Grenoble Alpes

préparée au sein du **Laboratoire Laboratoire Jean Kuntzmann**
dans **l'École Doctorale Mathématiques, Sciences et**
technologies de l'information, Informatique

Construction et validation d'un atlas statistique 3D des os carpiens humains

Construction and Validation of a Statistical 3D Atlas of Human Carpal Bones

Thèse soutenue publiquement le **16 décembre 2019**,
devant le jury composé de :

Monsieur XAVIER PENNEC

DIRECTEUR DE RECHERCHE, INRIA CENTRE S. ANTIPOLIS -
MEDITERRANEE, Rapporteur

Monsieur SEBASTIEN VALETTE

CHARGE DE RECHERCHE HDR, CNRS DELEGATION RHONE
AUVERGNE, Rapporteur

Monsieur PIERRE PORTERO

PROFESSEUR, UNIV. PARIS-EST-CRETEIL-VAL-DE-MARNE,
Examineur

Monsieur YOHAN PAYAN

DIRECTEUR DE RECHERCHE, CNRS DELEGATION ALPES, Président

Monsieur LIONEL REVERET

CHARGE DE RECHERCHE, INRIA CENTRE DE GRENOBLE RHÔNE-
ALPES, Directeur de thèse

Monsieur FRANCK QUAINÉ

MAITRE DE CONFERENCES, UNIVERSITE GRENOBLE ALPES, Co-
directeur de thèse



REMERCIEMENTS

Faire une thèse est un exercice compliqué et de longue haleine, et je ne suis arrivée au bout de la mienne que parce que j'ai été bien entourée tout du long. Je tiens donc à remercier toutes les personnes qui m'ont aidé et soutenu que ce soit un peu ou beaucoup.

Pour commencer, je voudrais remercier chaleureusement mes directeurs de thèse : monsieur Lionel Reveret de l'Inria Grenoble et monsieur Franck Quaine du laboratoire Gipsa à Grenoble, pour la confiance qu'ils m'ont accordée en acceptant d'encadrer ce travail doctoral et en me proposant de prendre part à ce projet passionnant. Leur aide m'a été précieuse pour mener le travail à son terme et ils m'ont beaucoup appris au fil des années.

J'adresse tous mes remerciements aux membres de mon jury. Monsieur Xavier Pennec de l'Inria Sophia-Antipolis et monsieur Sébastien Valette du laboratoire Creatis à Lyon m'ont fait l'honneur d'être les rapporteurs de cette thèse, et je les en remercie, ainsi que pour leurs remarques constructives. Je remercie également monsieur Pierre Portero de l'université Paris-Est qui a accepté d'être examinateur de mon travail ; j'ai apprécié cette participation qui souligne la perspective pluridisciplinaire, encore à ses prémises dans cette thèse. Enfin, je sais gré à monsieur Yohan Payan du laboratoire TIMC à Grenoble d'avoir été le président de mon jury.

J'exprime ma gratitude pour tous les membres du Laboratoire Jean Kuntzmann. Que ce soit d'ordre scientifique, administratif et surtout humain, j'y ai trouvé de nombreux interlocuteurs formidables qui ont rendu mon séjour dans le laboratoire agréable. Je salue tout particulièrement les doctorants que j'ai côtoyé au fil de ces années avec lesquels on a tant partagé.

Je tiens également à remercier mes amis, toujours présents et sources constantes de soutien. Je veux notamment citer Adrien, Alex, Agathe et JR à leur demande insistante, mais que cela ne laisse pas croire que je pense moins aux autres, ils me sont tous importants.

Et finalement "last but not least" je voudrais dire toute la reconnaissance que j'ai pour mes parents, qui ont été là du tout début à la toute fin et à qui je dois tant, que ce soit pour la thèse comme pour le reste.

CONTENTS

Remerciements	iii
List of Figures	ix
List of Tables	xi
List of Abbreviations	xiii
I Introduction	3
1 Construction of anatomical atlases of carpal bones	7
1.1 Introduction	9
1.2 Wrist anatomy and biomechanics	10
1.2.1 The bones	10
1.2.2 Movement of the wrist	12
1.3 Existing databases	18
1.3.1 Imaging modalities	18
1.3.2 Wrist movements capture : static vs dynamic	21
1.3.3 NIH database	22
1.3.4 Brown U. - Stanford CMC database	23
1.4 Similarity and correspondence of 3D meshes	26
1.4.1 3D meshes geometry	26
1.4.2 From CT scans to 3D meshes	26
1.4.3 Measures of similarity between meshes	28
1.4.4 Correspondence between meshes	30
1.4.5 Correspondence: quality assessment	32
1.4.6 Correspondence: computation	35
1.5 Dense correspondence for wrist bones	39
1.5.1 Existing technique	39
1.5.2 The problem of validation	41

1.6	Conclusion	42
2	Wrist modeling with dense correspondence	45
2.1	Introduction	47
2.2	Method presentation	49
2.2.1	Method overview	49
2.2.2	Preprocessing	49
2.2.3	Template set creation (4)	55
2.2.4	Dense correspondence mapping	56
2.2.5	Results	60
2.3	Numerical Validation	62
2.3.1	Preprocessing	62
2.3.2	Template set creation (4)	65
2.3.3	Dense correspondence mapping	67
2.4	Conclusion	72
3	Applications using dense correspondence properties	77
3.1	Introduction	78
3.2	Statistical Shape Model	79
3.2.1	State of the art	79
3.2.2	Principal Component Analysis	81
3.2.3	Gaussian Processes	92
3.2.4	Discussion	101
3.3	NIH reparameterization	103
3.3.1	Dense correspondence mapping of the NIH using the SSMs	103
3.3.2	Numerical Validation	105
3.3.3	Discussion	109
3.4	Anatomical Joint Coordinate Systems	111
3.4.1	State of the art	111
3.4.2	Coordinate System Computation	113
3.4.3	Comparison with Halilaj's results	114
3.4.4	Discussion	115
3.5	Conclusion	117
4	Statistical Movement Model	121
4.1	Introduction	122
4.2	State-of-the-art	123
4.3	Parametric model of the wrist motion	125
4.3.1	Multiple regression analysis	125
4.3.2	Parametric model	126
4.3.3	Model application	126
4.3.4	Model validation	127
4.4	Conclusion	134
C	Conclusion and perspectives	137
X	Appendix	141

X.1	Volume dissimilarity: CMC resampling	142
X.2	Volume dissimilarity: template set creation	143
X.3	Volume dissimilarity: Laplacian deformation	144
X.4	Volume dissimilarity: Laplacian + projection registration	145
X.5	Statistical Movement Model: Generalization	146

LIST OF FIGURES

1.1	The carpal bones	10
1.2	The structure of the radius distal end	11
1.3	The carpal bones mean sizes	11
1.4	TMC joint	12
1.5	Human anatomy planes	13
1.6	Human anatomy planes in the hand	14
1.7	Wrist flexion-extension	14
1.8	Wrist radial-ulnar deviation	15
1.9	Thumb flexion-extension	16
1.10	Thumb abduction-adduction	16
1.11	Use of coordinate systems in an articular chain	17
1.12	Projectional radiography of a wrist	19
1.13	CT scan of a wrist	20
1.14	A wrist from the NIH database	23
1.15	Functional poses	24
1.16	Extreme thumb poses	25
1.17	A wrist from the CMC database	25
1.18	Composition of a 3D mesh	26
1.19	From CT scan to 3D mesh	27
1.20	Output 3D mesh of a marching cube algorithm	27
1.21	Shape correspondence: sparse vs dense	31
1.22	The influence of bad shape correspondence on shape model	33
1.23	Three different shape correspondence results	34
1.24	Correspondence based on proximity criterion	36
1.25	Influence of the reference on the registration results	37
1.26	Two models of group-wise registration	38
2.1	Mesh notations	50
2.2	Flowchart towards dense correspondence	51
2.3	Initial input mesh	52

2.4	Anomalies in initial input meshes	53
2.5	The radius-based coordinate system.	55
2.6	Example of the features points used to initialize the radius smooth deformation algorithm.	59
2.7	Similarity between final and target meshes in wireframe view	72
2.8	Similarity between final and target meshes as colored surfaces	73
3.1	Example of a Principal Component Analysis	82
3.2	PCA results on the whole wrist	86
3.3	Influence of the number of modes used for SSM registration - individual models - mean distance	87
3.4	Influence of the number of modes used for SSM registration - individual models - Hausdorff distance	88
3.5	Influence of the number of modes used for SSM registration - whole wrist model - mean distance	89
3.6	Influence of the number of modes used for SSM registration - whole wrist model - Hausdorff distance	90
3.7	Joint Coordinate System of the TMC joint	116
4.1	Wrist pose variations simulated by the model for the two extreme values of the wrist flexion-extension parameter	128
4.2	Wrist pose variations simulated by the model for the two extreme values of the wrist deviation parameter	129
4.3	Wrist pose variations simulated by the model for the two extreme values of the thumb flexion-extension parameter	129
4.4	Wrist pose variations simulated by the model for the two extreme values of the thumb abduction-adduction parameter	129
4.5	Wrist pose variations simulated by the model for the boolean <i>loaded</i> parameter	130
4.6	Computation of a pose with the movement model from the predictor values	132

LIST OF TABLES

1.1	The CMC database poses	24
2.1	Distance between initial and resampled meshes	64
2.2	The number of vertices of each template $M_{T,\{b\}}$	65
2.3	Distance between the templates and database meshes	66
2.4	Distance between Laplacian deformed templates and database meshes	69
2.5	Distance between final deformed templates and database meshes	70
3.1	Generalization, Specificity and Compactness of the SSMs	91
3.2	GPMM registration with posterior information	99
3.3	Parametric registration of GPMM	101
3.4	Distance between original and resampled meshes of the NIH database	106
3.5	Distance between resampled meshes of the NIH database and the SSMs mean shapes	107
3.6	Distance between resampled meshes of the NIH database and the registered SSMs	108
3.7	Distance between resampled meshes of the NIH database and the final resulting deformed templates	109
3.8	Joint coordinate systems steadiness across the database	115
4.1	Computation of the statistical movement model parameters	127
4.2	Generalization capacity of the statistical movement model for the MC1	131
4.3	Average transformation from neutral pose to all other for the MC1 and MC3	133
X.1	Volumetric dissimilarity between initial and resampled meshes	142
X.2	Volumetric dissimilarity between the templates and the database meshes	143
X.3	Volumetric dissimilarity indexes between Laplacian deformed templates and database meshes	144
X.4	Volumetric dissimilarity indexes between final deformed templates and database meshes	145
X.5	Generalization capacity of the statistical movement model for the MC3	146

- X.6 Generalization capacity of the statistical movement model for the LUN . 146
- X.7 Generalization capacity of the statistical movement model for the HAM . 147
- X.8 Average transformation from neutral pose to all other for the LUN and HAM147

LIST OF ABBREVIATIONS

Bone name

CAP	Capitate
HAM	Hamate
LUN	Lunate
MC1	Metacarpal 1
MC2	Metacarpal 2
MC3	Metacarpal 3
MC4	Metacarpal 4
MC5	Metacarpal 5
PIS	Pisiform
RAD	Radius
SCA	Scaphoid
TPD	Trapezoid
TPM	Trapezium
TRQ	Triquetrum

ULN Ulna

Joint name

CMC	Carpometacarpal joint
TMC	Trapeziometacarpal joint

Image Acquisition Technique

CT	Computed Tomography
MRI	Magnetic Resonance Imaging

Method name

GPMM	Gaussian Process Morphable Model
ICP	Iterative Closest Point
MDL	Minimum Description Length
PCA	Principal Component Analysis
PDM	Point Distribution Model
SSM	Statistical Shape Model

INTRODUCTION

The human hand plays an important role in a person's everyday life for it is required for many varied tasks. The incredible variety of functions of the hand is due to its combination of strength, precision and mobility. The reduction of any of these features can prove to be incapacitating. The wrist is the source of the large range of motion of the hand. Fully apprehend this articulation is essential to be able to make diagnosis, prevent and treat any injury. The wrist is a very complex joint, composed of eight small bones, connected to five metacarpal bones on the hand side and to the two forearm bones. The complexity of the joint is not only due to the high number of interconnected bones (15 in total), but also to the small size of the carpal bones and their elaborate shapes interlocked with each other, that move in an intricate way around each other.

In this thesis we are interested in modeling the 3D wrist bone shapes. Computer models can be used to take measurements, serve as basis for the creation of automated IT tools, or else be integrated into software for diagnosis support for example. They can provide the required prior information to automate some tasks, such as segmentation of images or inferring 3D volumes from 2D images. The quality of the results of such applications depends on the quality of the model. We therefore attach a special importance to the validation of our work, while such assessment cannot directly be measured and must be proven by indirect metrics. Not many works on wrist bones modeling have been conducted yet, which is mostly due to the little data that have been collected into databases exploitable for computer models.

We have taken interest in tools for the modeling of 3D shapes, especially in techniques of correspondence between 3D meshes, and propose a method to transform raw data extracted from Computed Tomography (CT) scans into corresponding bone representations. As discussed in the literature, it is not trivial to define the resampling procedure, and neither is its quality assessment. The dense correspondence relations that we compute make possible many applications. We propose several utilizations. Variability among bones is analyzed with statistical procedures such as the Principal Component Analysis (PCA) and another one based on Gaussian Processes. While the PCA-based model has already been introduced for wrist bones, the second has never

been used before for carp modeling. The registration capacities of the first model are employed for defining correspondence with a second database. We propose a method to easily transfer systems of coordinates or other landmarks from a few example towards the rest of the database, a convenient function for biomechanical wrist motion study. In a last phase, we are concerned with modeling wrist bones motions with a parametric model based on meaningful and easily measurable predictors.

The work realized is presented in this document and structured as follow:

The first chapter introduces the context of the work. It is composed of three main themes: the wrist anatomy and biomechanics, image databases from CT scans and tools for 3D modeling. Our work focuses both on carpal bones shapes and wrist motion, a rough overview of the wrist functioning is essential for a better comprehension of the issue. The presentation of the database we are using is similarly important, a statistical model can only be as good as the data it is based on. In a large part of the chapter are detailed a type of data representation, 3D meshes, and related properties that are of interest for our work such as shape similarity evaluation and correspondence between shapes characteristics. We explore the literature about similar issues, and particularly detail works focusing on wrist shape modeling.

In a second chapter, we present our work to define correspondence relations between bones of a database. A first step creates common reference templates of the wrist bones from the set of data. These templates represent the mean bone shapes. In a second step, the common templates are deformed to match accurately the individual data extracted from CT scans. This method preserves corresponding relations between the vertices. We attach importance to the reproducibility of the method. We prove that the new mesh parameterization causes limited loss of information compared to the initial shapes extracted from the scans. The generated meshes can therefore be used for shape analysis, without biasing the results with bad shape encoding.

In a third chapter, we introduce applications of the data previously generated. All these operations depend on correspondence between meshes previously calculated. Two statistical models are computed, one based on a Principal Component Analysis and one on Gaussian Processes. The capacities of registration of these models to new shapes are evaluated. Correspondence is defined with the wrists of another database using the first statistical model, and we prove again that the similarity between the raw shapes and the reparameterized achieves results with a high accuracy, enabling the use of the second ones without introducing bias. Finally we propose to use correspondence relations to transfer point locations across bones. This can be used to define any systems of coordinates without having to rely on any anatomical or mathematical landmarks while being sure to reproduce them, important condition for definition of joint systems of coordinates.

In the fourth and last chapter, we introduce a preliminary work about wrist motion modeling. In the literature very few parametric models of wrist motion exist, and they are only based on a principal component analysis. We propose a parametric model resting on meaningful predictors: the degrees of freedom of the articulations. Correlation between pose characteristics and meshes locations and orientations are

identified with a linear regression. We test these parameters and show that they are indeed correct predictors for a model, which reacts as expected. We test the accuracy of new poses generated from predictors values. We explain why more appropriate data are required for further investigation and validation.

CHAP. 1

CONSTRUCTION OF ANATOMICAL ATLASES OF CARPAL BONES

Contents

1.1	Introduction	9
1.2	Wrist anatomy and biomechanics	10
1.2.1	The bones	10
1.2.2	Movement of the wrist	12
1.2.2.a	Anatomical planes for movement description	12
1.2.2.b	Wrist movements	13
1.2.2.c	Thumb movements	15
1.2.2.d	Kinematic description of joint movement	16
1.3	Existing databases	18
1.3.1	Imaging modalities	18
1.3.2	Wrist movements capture : static vs dynamic	21
1.3.3	NIH database	22
1.3.4	Brown U. - Stanford CMC database	23
1.4	Similarity and correspondence of 3D meshes	26
1.4.1	3D meshes geometry	26
1.4.2	From CT scans to 3D meshes	26
1.4.3	Measures of similarity between meshes	28
1.4.4	Correspondence between meshes	30
1.4.5	Correspondence: quality assessment	32
1.4.6	Correspondence: computation	35

1.5 Dense correspondence for wrist bones	39
1.5.1 Existing technique	39
1.5.2 The problem of validation	41
1.6 Conclusion	42

1.1 Introduction

In a first part we introduce the anatomy of the wrist. This articulation is unique and very complex, composed of many interlocked small bones. We are interested in modeling these bones, we therefore have to understand the main characteristics of the joint, for example the sizes of the bones: the size of a carpal bone is in the order of a few centimeters at max, a submillimetric precision in its representation is required. We pay attention to the specific anatomy of the trapeziometacarpal joint at the base of the thumb. It is an important source of the great thumb mobility and many investigations of this joint kinematics have been conducted over the years. We explain how such studies often rely on definitions of system of coordinates, who require to be easily reproducible. We later will propose a method to define such systems and test it on the trapeziometacarpal joint. The degrees of freedom of both the wrist and the thumb are presented, these degrees of freedom will be suggested as predictors of a parametric model of the wrist motion.

In a second part, we present the data on which the work is based. Different imaging modalities are introduced, in particular CT scans, used to capture the wrists bones. The understanding of how the data are acquired, the precision that can be expected are of uttermost importance. A model can never reach a better accuracy than the data upon which it was constructed. The two databases used in the following work are presented. Capture of movement using static or dynamic acquisition systems is discussed as well as the potential bias introduced by static acquisition, for we use such static data, only the extreme poses of a movement were captured.

The third part focuses on 3D meshes and their properties. At first the description of a 3D shape with a mesh made of vertices, edges and faces is explained. The construction of 3D meshes extracted from stacks of scans by human detouring and volumetric structuring is described. Different approaches to measure similarity between surfaces or volumes delineated by meshes are introduced. It is essential to assess that two meshes characterize a same volume, in particular for operations of mesh resampling whose aim is to describe the same implicit 3D volume but with different vertex and edge distributions. A section is dedicated to the definition of correspondence between meshes. Examples of applications of this property are given. We review existing methods to compute correspondence between shapes, as well as criteria suggested in the literature to quantify correspondence quality.

Finally, the last part completes the literature review with existing applications of wrist bones modeling, especially ones concerned with correspondence between carpal bones and the validations proposed for these methods. This state-of-the-art is the context of a large portion of the work realized for this thesis.

1.2 Wrist anatomy and biomechanics

1.2.1 The bones

The wrist articulation, also named carpus, is composed of eight small bones, called carpal bones. Carpal is a derivative from the greek word *καρπός* and the latin one *carpus*, meaning "wrist".

The carpal bones are usually classified in two sets : the proximal row and the distal row. The proximal row is composed of four bones : the **Scaphoid** (sca), **Lunate** (lun), **Triquetrum** (trq) and **Pisiform** (pis) bones. The distal row consists of the **Trapezium** (tpm), **Trapezoid** (tpd), **Capitate** (cap) and **Hamate** (ham) bones. The position of the carpal bones in the hand and in relation to each other is illustrated in Fig. 1.1.

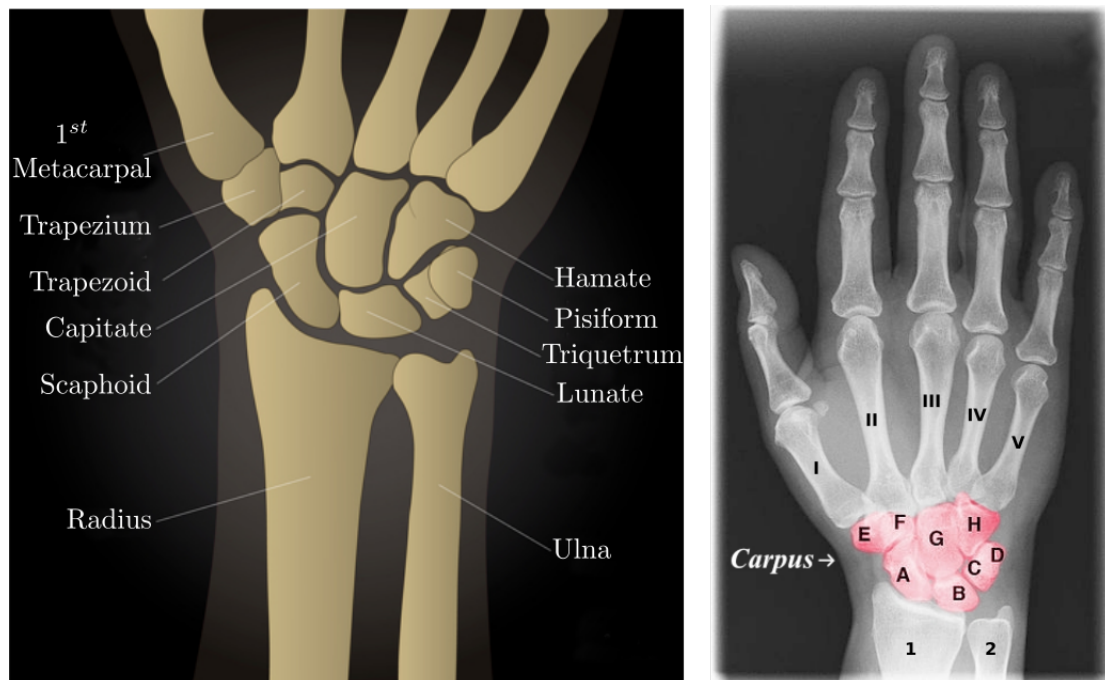


Figure 1.1: The carpal bones: on the left a drawing (image from Radiopaedia; Dr S. Hapugoda). On the right an annotated XRay image. The bones are: A. Scaphoid; B. Lunate; C. Triquetrum; D. Pisiform; E. Trapezium; F. Trapezoid; G. Capitate; H. Hamate; 1. Radius; 2. Ulna; From I to V: 1st to 5th Metacarpals (image from Wikipedia).

The proximal row is on the side of the forearm and articulates with the two forearm bones: the Radius (rad) and the Ulna (uln). Some vocabulary connected to the radius structure is introduced in Fig. 1.2. The distal row articulates with the five Metacarpals numbered from 1 on the thumb side to 5 on the little finger side (mc1 to mc5). These metacarpals are situated in the palm of the hand, and each one is related to a finger, composed of three phalanges, except for the thumb which only has two of them, as pictured in Fig. 1.1.

The wrist bones are really small, a few centimeters at max in every directions. Crisco et al. [CCMU05] measured the mean dimensions of each carpal bones along their three

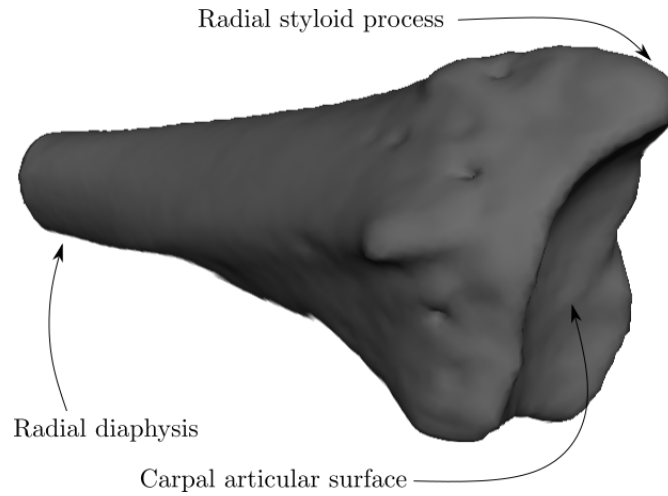


Figure 1.2: The structure of the radius distal end (near the wrist).

principal inertial axes, for 28 volunteers of both genders. Their results are illustrated in Fig. 1.3. It is essential to have a global idea of the size of the carpal bones when modeling them, to be able to interpret the influence that a 1 mm error can have for example.

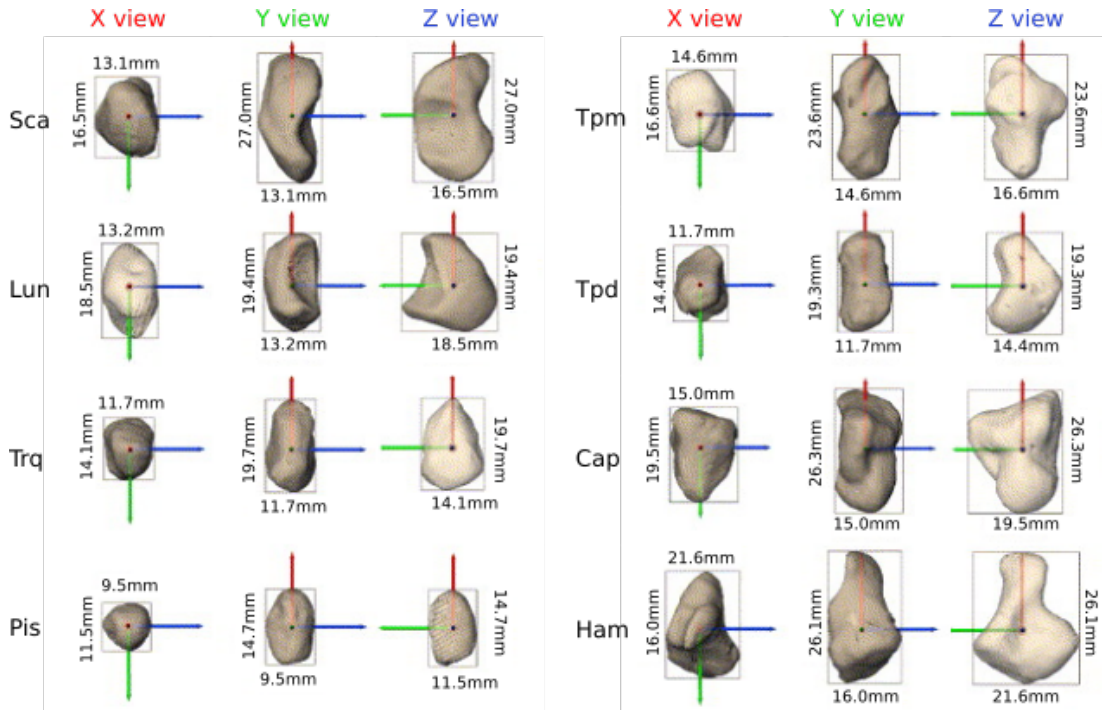


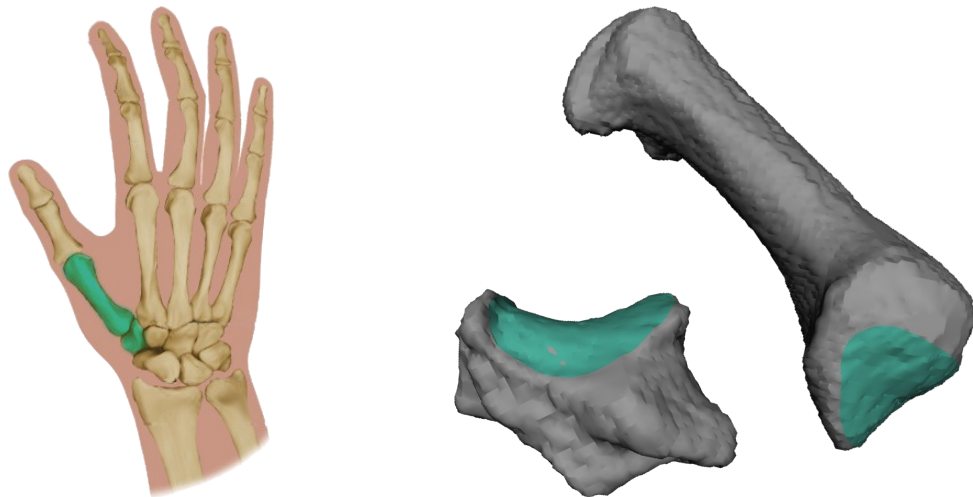
Figure 1.3: Mean sizes of the carpal bones (from [CCMU05]).

The sex of the person has some influence on the carpal bones, as reported in [CCMU05, CLW+14, JLBC16]. The carpal bone size is gender dependent, the bones dimensions are significantly smaller in women than in men. There are however no

gender-related differences in the relative sizes of the carpal bones when the volume of the bone is normalized with the total carpus volume, even though significant sex-based carpal bone shapes differences exist. There are no shape differences between the left and right wrists bones.

The Trapeziometacarpal joint

The trapeziometacarpal (TCM) joint, also sometimes referred to as carpometacarpal (CMC) joint is situated at the base of the thumb, as illustrated in Fig. 1.4a. It is the articulation between one of the carpal bones, the trapezium and the 1st metacarpal. It has distinctive articular surfaces, shaped as two saddles moving around each other, as depicted in Fig. 1.4b. The articular surface shape is the source of the two degrees of liberty of the thumb movement, and is also the source of the great range of motion of the latter .



(a) The location of the TMC joint in the wrist

(b) The articulation surfaces of the TMC joint. The two bones are differently scaled for visualization purposes.

Figure 1.4: The TMC joint

1.2.2 Movement of the wrist

1.2.2.a Anatomical planes for movement description

In order to precisely and unambiguously describe human and more generally vertebrate anatomy and movement, three orthogonal reference plans have been defined. They are described for human body in standard anatomical position, which refers to a standing position, with arms at the side and palms facing forward. The three anatomical planes can be observed in Fig. 1.5.

The anatomical planes are:

- **The coronal plane:** also called frontal plane, it divides the body into dorsal (in the back of the plane) and ventral (in front of the plane) portions.

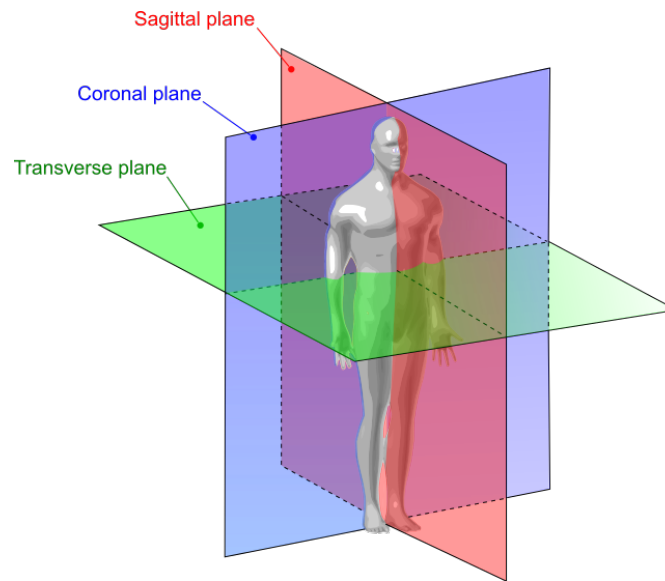


Figure 1.5: The three human anatomy planes (from commons.wikimedia.org)

- **The axial plane:** it is a horizontal plane that isolates the upper part of the body from the lower part.
- **The sagittal plane:** the third orthogonal plane is vertical and separates the body into two symmetrical parts (left and right).

The same planes can be defined for the human hand, as can be seen in Fig. 1.6. Then, the coronal plane separates the hand into the palmar and the dorsal sides. The axial plane isolates the upper side linked to the forearm from the lower side composed of the finger tips. And the sagittal plane divides the hand into the radial side (side of the radius bone and the thumb) from the ulnar side (side of the ulna bone and the little finger).

1.2.2.b Wrist movements

Wrist movement is a combination of motions, that can be decomposed as rotations around two axes of the articulation defining flexion-extension and radial-ulnar deviation. This combination of movement allows a rotational movement of the hand called circumduction.

Sometimes, the pronation-supination movement, which describes the rotation of the forearm into palm up or down position, is wrongly thought to be a part of wrist movement. But this motion caused by the revolution of the radius around the ulna happens in the forearm and is considered to be an elbow degree of freedom.

Wrist flexion - extension

The flexion-extension movement of the wrist is a rotation in the sagittal plane. Flexion consists in bending the hand downwards, while reducing the angle between

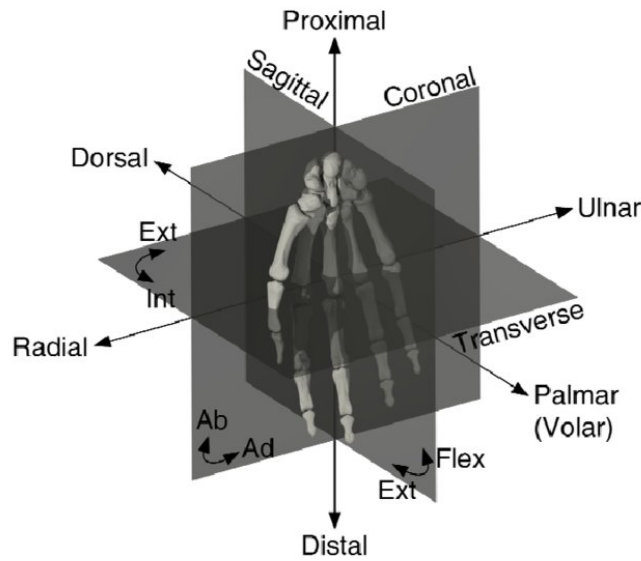


Figure 1.6: The three anatomy planes defined for the human hand (from [BBD12])

the palm of the hand and the forearm. Extension consists in bending the hand upwards, the angle between the back of the hand and the forearm is reduced. Both movements are illustrated in Fig. 1.7. It is the wrist movement with the biggest ranges of motion, normal wrist flexion is approximately 70 to 90 degrees, while normal wrist extension ranges between 65 to 85 degrees.

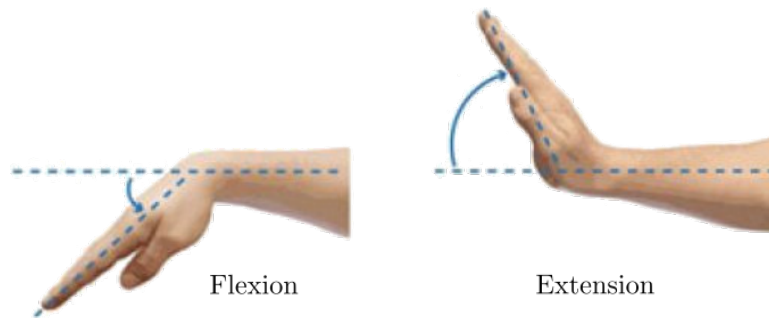


Figure 1.7: The wrist movement of flexion - extension

Wrist radial - ulnar deviation

The radial-ulnar deviation is a rotation in the coronal plane. The radial deviation tilts the wrist toward the thumb side of the hand, which is also the side of the radius. On the opposite, ulnar deviation tilts the wrist toward the little finger side of the hand, which is the side of the ulna in the forearm. Both movements are illustrated in 1.8. Maximal amplitudes of both deviations depend on the flexion-extension angle of the wrist. Deviation amplitude is maximal when the flexion-extension angle is zero, while it is greatly limited when the wrist is either in flexion or extension. Radial deviation

motion ranges between 15 to 25 degrees, while ulnar deviation ranges from 25 to 40 degrees approximately.

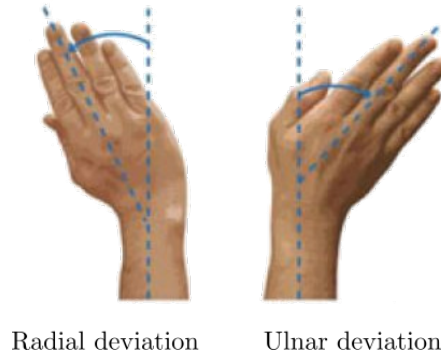


Figure 1.8: The wrist movement of radial - ulnar deviation

Wrist neutral position

The neutral position of the wrist is the position from which posture angles are measured. It consists in a straight alignment of the wrist with the forearm. The forearm is at mid-point between pronation and supination. The angles of flexion-extension and radial-ulnar deviation are zero.

1.2.2.c Thumb movements

Similarly to the wrist, the thumb has two principal axes of motion: flexion-extension and abduction-adduction. These primary motions can be combined into complex movements, such as making circles in a circumduction movement.

In addition to flexion-extension and abduction-adduction the thumb can rotate around its long axis in a movement referred to as pronation-supination. However it cannot be controlled and happens only as a side effect of the two principal motions. It is therefore not considered as a thumb degree of liberty.

The thumb wide range of motion is often considered to be achieved mostly at the articulation between the wrist and the thumb phalanges: the TMC joint.

Thumb flexion - extension

The flexion movement of the thumb refers to the rotation of the finger in the direction of the palm. In full flexion the thumb extremity is near the base of the little finger. The extension movement consists in rotating the finger away from the palm. An illustration of such a movement is presented in Fig. 1.9.

Thumb abduction - adduction

The abduction movement consists in a rotation of the thumb away from the other fingers. In full abduction, the thumb points straight out of the palm, forming a 90° angle with the rest of the fingers, if the latter are joined. On the opposite, adduction brings

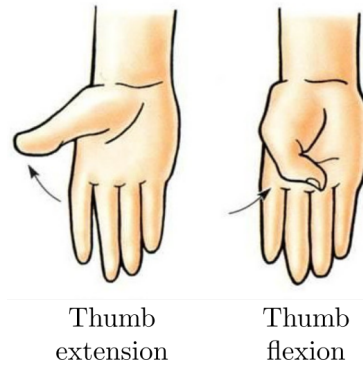


Figure 1.9: The thumb movement of flexion-extension

the fingers close to each other. The thumb abduction-adduction movement is illustrated in Fig. 1.10.

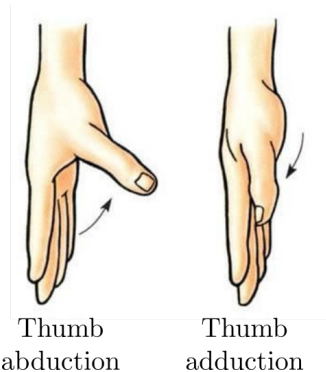


Figure 1.10: The thumb movement of abduction-adduction

1.2.2.d Kinematic description of joint movement

Kinematics is a branch of mechanics that describes the motion of bodies independently of the forces causing the motion. It is used to analyze position, velocity and acceleration of bodies in a system.

For each solid, motion is described with six degrees of freedom (DoF): 3 directions of translation and 3 angles of rotation in space. However, articulations movements are restricted, and some coordinates are always zero. For instance, the complex wrist motion is often simplified as an articulation with two DoF (Flexion-extension and radial-ulnar deviation). This representation of the wrist considers the joint as a whole, yet it is composed of 8 bones, which all have 6 DoF. The movement of the wrist is different from the movement of the carpal bones.

Anatomical description of movement uses the anatomical planes to characterize motion. Kinematic description of movement is described according to a frame of reference. This frame of reference is most often a Cartesian coordinate system defined by an origin and 3 orthonormal axes. The reference coordinate system can be absolute,

when it is a global reference frame, such as Earth. It can on the opposite be attached to a moving object, the motion of the object of interest is then described relatively to the reference object movement. The position and orientation of the object of interest are necessary to characterize the object motion. They themselves can be computed using a coordinate system attached to it. Thereby, a joint movement can be described by attaching two coordinate systems on the two bones of the joint, and by analyzing their relative movements. This method of joint movement characterization using two coordinate systems was first introduced by Grood and Suntay [GS83]. In Fig. 1.11 is illustrated an example of a leg's articular chain: a system of coordinates is defined for each bone of the chain and the movement of each bone is described as the rotation and translation of its system of coordinates relatively to the one of its proximal neighbor bone.

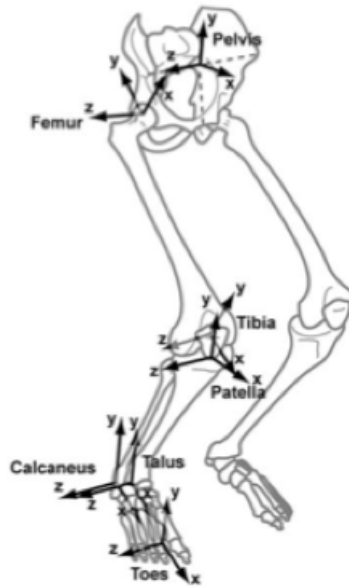


Figure 1.11: Example of the use of system of coordinates for the characterization of the leg articular chain movement. (from simtk-confluence.stanford.edu)

1.3 Existing databases

In statistical modeling, like in training based approaches, results can only be as good as the data it relies on. The work pertinence depends a lot on the database, particularly on the number of elements. Yet, especially when working with medical images, lack of data is a very common and major constraint. It is due to medical secrecy preventing collection of existing data. Moreover, new database creation needs to be validated by an ethic committee, in particular when it requires exposure of individuals to intrusive or ionizing methods. In addition to these factors, building a database takes a lot of time. In some domains means were put to gather numerous annotated data, such as for brains or liver cells [ASM⁺19]. In other domains databases are still rare and composed of limited numbers of elements for now.

The case of wrist databases is unfortunately a good example to illustrate the few available data. For the moment, only one database is public [MCTL07], composed of 60 wrists from 30 subjects. A few other databases are used in some papers (for example in [vdGFV⁺11, CGHM12]), but there are never more than a few tens of wrists at max composing the databases (25 subjects for both previously cited papers). These databases are not publicly available and cannot be used for other works or results comparisons. In this thesis we present works on a new database of 46 subjects including all carpal bones but also the totality of the five metacarpals and a portion of the radii and ulna. We use information learned from this database to process the public NIH database, to later enable operations on all data, for enriched results.

Many characteristics are essential when a database is being created. The imaging technique should offer the best possible resolution and a high contrast between the objects of interest (the bones in our case) and the surroundings, to limit as much as possible errors of segmentation. The 3D object construction procedure should also be cautiously chosen. Diversity between individuals should be favored, to restrict bias.

In this thesis, two databases of carpal bones have been used. They are described in the following section. At first, we present the imaging modality that was used in both cases, for a better understanding of the data. Computed Tomography scanner is currently the modality that has the best contrast for bone images while composed of 3D information. We introduce other modalities that have been used as alternatives, though they do not present as good characteristics for bone imaging. We argue that even for movement analysis, static CT scans are the most precise imaging modality. The characteristics of both databases creation are detailed afterwards.

1.3.1 Imaging modalities

Medical imaging refers to all methods used to capture pictures of the inside of a body. In a large majority, these methods are noninvasive, no instrument needs to be introduced in the subject's body to take a snapshot.

This science is quite recent, the first picture ever taken of the inside of a body was captured by Wilhelm Röntgen in 1895 only, during his research on X-Rays. Since then, medical imaging has evolved a lot, and recent progresses in computer science

enabled new 3D imaging techniques. Multiple modalities exist nowadays, and are very commonly used either for diagnostic or research.

Any type of tissue, whether bone, tendon, organ, muscle, etc... can now be examined underneath the skin of a body. However, it requires to use the appropriate imaging technique. The choice of method is crucial, as many procedures exist, and each is sensitive to some tissue properties only. In the case of 3D bones analysis, Computed Tomography (CT) scanning is the appropriate imaging technique, due to its high sensitivity to bones dense structures and its volumetric results. CT scans are a 3D extension to 2D projectional radiography, relying on computer processing to generate the volumetric information. These two methods are briefly introduced, for a better understanding of the data.

Radiography



Figure 1.12: Example of projectional radiography imaging: a X-Ray image of a wrist in postero-anterior view. Image from [BKA11]

The oldest and probably most wide-spread imaging technique is radiography. Radiography uses the properties of some rays, mostly X-rays or Gamma-rays to produce an image.

The acquisition system consists in a ray generator, that projects a beam of rays onto a detector, that captures them. The object that is being radiographed is put between the generator and the detector. Depending on the internal structure of the object, and more precisely on the density of its structure, some of the radiation is being absorbed. The contrast of absorption creates the image.

Bone tissue is denser than soft tissue. Thus bones are visible on radiography pictures, that are highly contrasted. This method is particularly adequate for skeleton visualization and fracture detection. In the case of the wrist, it is suitable for visualizing the bones, their alignment and joints space. An example of an X-ray image of a wrist is visible in Fig. 1.12.

One downside is that the resulting picture is a 2D view of the internal structure of the object. The 3D information is lost in the process. To counter this effect, multiple views at different angles of the same object are generally taken. A second downside is the exposure of the patient to ionizing radiation, dangerous for health, though it is relatively minor in the case of the hand [HAC⁺15].

We can cite the MURA database [RIB⁺17], a large collection of radiographs of various upper-body parts, including almost 3700 images of wrists, both normal and abnormal. The database is intended for classification of normal vs abnormal studies using machine learning methods.

Computed Tomography

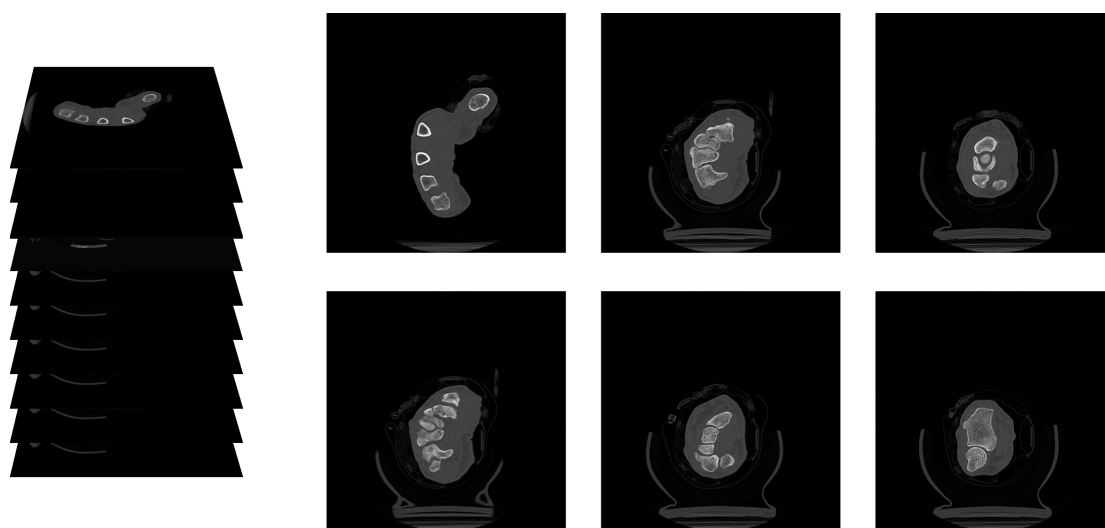


Figure 1.13: Example of CT scan imaging : a stack of 2D cross-sectional images. An example of 6 cross-sections from a unique wrist. Images from the CMC database.

Computed Tomography Scans are usually referred to as CT scans. Like previous projectional radiography, the creation of CT scans is based on X-ray radiation. However CT scan aims at depicting the volume of the scanned object, on the opposite of previous radiography that simply projects the volume of the object onto a 2D plan.

The acquisition system is composed of a ray generator and a ray detector. They rotate around the object, capturing multi-view projections taken at different angles around an axis. A computer-based calculation produces cross-sectional images or slices of the inside of the object from the numerous projections. It represents non-homogeneous materials ray absorption capacity at every point. Post-processing can also be used to enhance contrast, reduce noise, etc. Finally, improved results can be obtained with the use of contrast agents absorbed by the patient beforehand.

CT scans data were historically generated in the form of a stack of 2D slices, in the axial or transversal plane. An example of such data of a wrist are visible in Fig. 1.13. Nowadays the output data can take other forms, including volumetric representations (in 3D).

Wrist CT scans are especially adequate for fracture detection : it is used for complex fractures, for example around joints, where the area of interest can be examined from multiple plans. It can also be used to detect fractures occulted by projectional radiography, or to gauge fractures. Finally, it is helpful for identifying joint irregularities, and might be used in some cases of soft tissues injuries. Like radiography, a downside of the method is the exposure of the patient to ionizing radiation.

Other medical imaging modalities

Computed Tomography scans is the most appropriate data format to extract precise 3D information of bone shape. Using such material enables the creation of 3D statistical models, shape comparison between groups of people, and so on.

However alternative data formats are also used for various applications, either because less or different information is needed, or because they become suitable for use when combined with models learned on more precise data. We present briefly in this paragraph other imaging modalities that have been used for wrist pathology detection, guiding of wrist surgery and other utilizations.

Magnetic resonance imaging, most commonly referred to as MRI is an image acquisition method based on the capacity of some atoms to absorb and emit radio signals, when they are in an external magnetic field. This method is particularly adequate for soft tissue visualization, especially fat or water. However MRI can also be relevant for bone observation and is recommended for some fractures detection in the wrist for instance [MT07]. Like CT scans, MRI produces 3D information, in the form of a stack of 2D images. It is less adequate than CT scans because bones have lower contrast with the environment, but has the benefit of being safe for living beings. Works have been dedicated to carpal bones segmentation in MR images [SVG02, KSCP11, WCT⁺15, FJB⁺18], but as was pointed out by Pedoia et al. [PML16] no fast and accurate musculoskeletal MRI segmentation method is established yet.

Two other imaging modalities have been sources of interest to some carpal bones works. But for both, models previously built based on CT scans have been used. The first modality is *fluoroscopy*, which is similar to projectional radiography but records movies over time instead of a simple image. Chen et al. have been working on inference of carpal bones kinematics based on fluoroscopic sequences [CGHM11, CGHM12]. Anas et al. have worked on registration of a statistical model to *ultrasound images*, to provide real-time assistance during scaphoid surgery [ARJ⁺15, ASR⁺16]. Ultrasound allows real-time viewing, and is safe but produces really noisy images, where bones are extremely difficult to discern, which makes the use of ultrasound images very challenging.

1.3.2 Wrist movements capture : static vs dynamic

The capture of movement in medical imaging raises issues. Dynamic acquisition systems that allow 3D data capture are not common. Such devices have been built for specific body parts movements [CJS⁺08], but they remain limited to some applications.

We discuss the choice of static vs dynamic image acquisition for carpal kinematics analysis.

Many different ways of capturing and measuring joints motions exist, based on electrogoniometers, surface markers filmed by cameras, 3D motion capture, etc... When bone movements are to be analysed using radiographic imaging, two major approaches exist: either the dynamic motion is filmed, multiple frames per second are captured, or only a few static poses of the joint are photographed. Both methods present downsides. Fluoroscopy is the imaging modality that produces a film of the moving body, by generating many frames through projectional radiography. It exposes the patient to a continuous or pulsed ionizing radiation, that can cause burns and increases the risk of cancer. Moreover, the resulting frames are in two dimensions, volumetric information is lost. It can be compensated by using multiple fluoroscopes at various angles, but it increases even more the radiation level. On the other hand, capturing a few static poses allows to have volumetric CT scans, and less exposure to ionizing radiation. But the motion can only be deduced by interpolation between poses, which supposes that the joint has fluid motion.

The error introduced by interpolating between poses instead of studying dynamic movement has been studied in the case of the wrist. Carelsen et al. [CBS+05] assumed that differences between dynamic and animated movements could exist due to neuromuscular control or physical properties. Some abrupt changes in the carpal bones orientations and positions had also been observed during dynamic movement [MDBG97]. On the observation that 3D imaging methods could only capture static poses, they built a device for 3D dynamic imaging of the wrist: a 3D-rotational X-Ray system [CBS+05, CJS+08]. Using this machine, Foumani et al. studied the differences between statically and dynamically acquired carpal kinematics [FSJ+09]. Their study was performed on eight healthy subjects for flexion-extension and radio-ulnar deviation movements. They concluded that very small and mostly non-significant differences were observed between both acquisition methods. They argue that abrupt changes and variability observed by some studies are due to external measure factors, such as the coordinate system choice, and don't exist in real wrist motion. Their study confirms that static data can be used to study carpal kinematics for individuals without any pathology. Both databases that are used in this thesis capture movement by scanning wrists at a few poses.

1.3.3 NIH database

The database referred to as NIH database for the rest of the document, is the only currently public database of wrist CT scans. It is fully described in [MCTL07].

Both wrists of 30 individuals were scanned for the database. These individuals are composed of 15 women, aged between 21 and 28 and 15 men, aged between 22 and 34. None of these subjects had history of wrist pathology or wrist trauma.

Both sides were captured simultaneously using a GE helical CT scanner (GE Medical, Milwaukee, WI). For wrists scans in various postures, the image resolution of a slice is $0.9 \times 0.9 \text{mm}^2$, with 1.0 mm between neighboring slices. However, the neutral scans

from which are extracted the volumetric surfaces of the bones were reconstructed from a smaller field of view, generating images with higher resolutions, the pixel resolution ranges from $0.2 \times 0.2 \text{mm}^2$ to $0.3 \times 0.3 \text{mm}^2$.

In the scans, the cortical surfaces of the eight carpal bones are fully visible. A portion of the distal radius and ulna that ranges from 1 to 2cm is also visible, along with 1 to 2cm of the proximal surfaces of the five metacarpals. A wrist of the NIH database and the portion of bones captured is visible in Fig. 1.14.

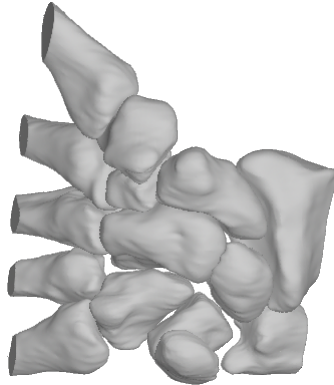


Figure 1.14: Example of one wrist from the NIH database. A short portion of the proximal metacarpals and distal radius and ulna are present in addition to the full eight carpal bones.

Two protocols were used for wrist poses captures. The first one, called incremental orthogonal protocol was used for 5 men and 5 women. Both movements of flexion-extension and radial-ulnar deviation are studied, by scanning eight targeted positions. The wrists were photographed in neutral position, 30° and 60° of flexion, 30° and 60° of extension, 20° and 40° of ulnar deviation and 20° of radial deviation. The second protocol, called combined motion protocol was used for 10 men and 10 women. It includes 9 movements, of flexion-extension and radial-ulnar deviation, but also of combined movements. In addition to the neutral position, the wrists were scanned at 40° of flexion, 40° of extension, 10° of radial deviation and 30° of ulnar deviation. The combined positions are composed of a 30° of ulnar deviation associated with both 40° of extension and flexion and 10° of radial deviation combined with both 40° of extension and 40° of flexion.

1.3.4 Brown U. - Stanford CMC database

Our work was mainly conducted on a database created by Crisco and his team in the Mechanical Engineering and Orthopedic department at Brown University and Stanford. It has been intended to study the carpo-metacarpal (CMC) joint between the trapezium and 1st metacarpal, in the base of the thumb. This joint is also sometimes referred to as trapeziometacarpal joint (TMC). Because of the original purpose of this database, it will be referred to in this document as the CMC database.

While the database originally included 46 subjects, two of them had such a short portion of radius visible that we haven't been able to use them for our method. We will

therefore introduce the 44 wrists that have been used. 44 individuals were scanned, one wrist per subject. None of them had any history of wrist injury or pathology. For 35 subjects, their right hand was scanned, while for 9 of them it was the left one. The group is composed of 24 women (age 41.2 ± 17.7 years) and 19 men (age 39.6 ± 19.2 years). Information about the last subject are missing.

Each individual was scanned in 11 targeted positions. The wrists were photographed in neutral position. Then the thumb was captured in four extreme positions: flexion and extension, adduction and abduction. Finally 3 functional tasks were scanned both without any force and while pushing. The functional tasks were pinch, jar grasp and jar twist. All poses are listed in Table 1.1. In the literature, illustrations for the same poses were proposed in [HMP⁺14, CHM⁺15]. We present them in Fig. 1.15 and Fig. 1.16 for a better comprehension of the poses.

	Pose	Load
1	Neutral	Not loaded
2	Thumb flexion	Not loaded
3	Thumb extension	Not loaded
4	Thumb abduction	Not loaded
5	Thumb adduction	Not loaded
6	Pinch	Not loaded
7	Pinch	Loaded
8	Jar grasp	Not loaded
9	Jar grasp	Loaded
10	Jar twist	Not loaded
11	Jar twist	Loaded

Table 1.1: The CMC database poses

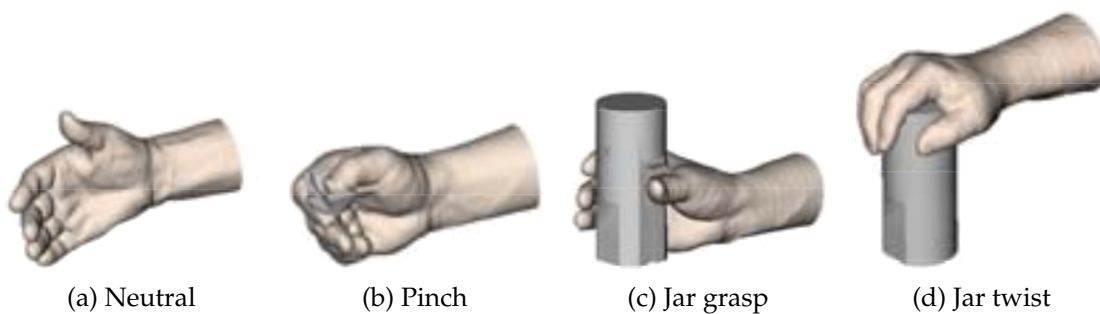
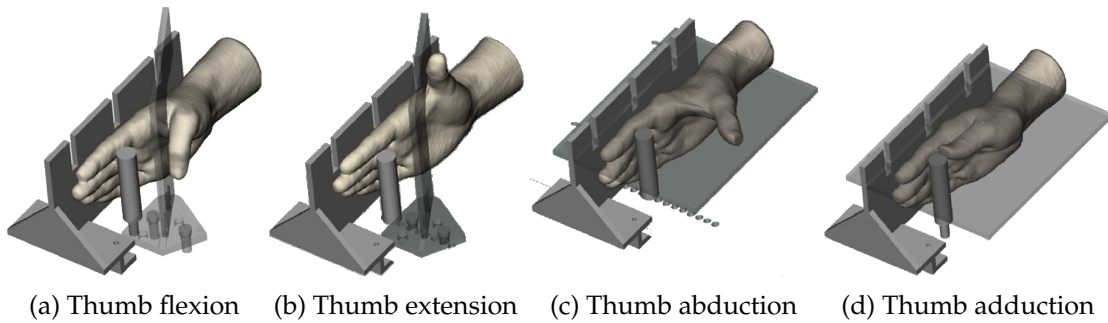


Figure 1.15: The functional poses of the CMC database. Images from [HMP⁺14].

The neutral poses were scanned with a resolution of 512×512 pixels, with 0.33 mm accuracy in the image plane. The space between slices ranges from 0.6 to 0.625mm.

In the scans the cortical surfaces of the eight carpal bones and the five metacarpals are fully visible. Only a portion of the distal radius and ulna were captured, with varying lengths, but it is in average a few centimeters long. An example of a wrist of the



(a) Thumb flexion (b) Thumb extension (c) Thumb abduction (d) Thumb adduction

Figure 1.16: The extreme thumb poses in the CMC database. Images from [CHM⁺15].

CMC database can be seen in Fig. 1.17. Compared to the NIH example wrist in Fig. 1.14, it is clear that the wrists of the CMC database are more complete than in the NIH one.

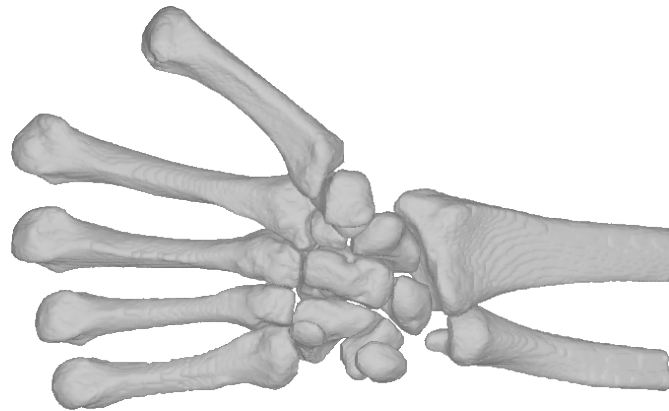


Figure 1.17: Example of one wrist from the CMC database. Varying portions of the proximal metacarpals and distal radius are visible, a few centimeters long in average. The five metacarpals and the eight carpal bones are captured in full.

In this section, we have introduced various modalities for capture of medical data. We have more specifically detailed the methods and characteristics used for the creation of the two databases used in this thesis, the NIH and the CMC databases. These specifications are important for future work, especially the precision of the acquired data. We will take the voxel resolution as a lower bound for the accuracy. Therefore the specifications must be kept in mind when considering the results obtained later.

While the initial captured data are stacks of 2D images, we are working with 3D polygon meshes. We present in the next section what are 3D meshes, how they were created from the CT scans. Then we introduce properties between 3D meshes and how to verify them. We end with a detailed state-of-the-art of works about carpal bone shapes studies.

1.4 Similarity and correspondence of 3D meshes

1.4.1 3D meshes geometry

Many representations of a 3D shape exist. It can be described as a filled volume, with voxels for instance, or else it can be delimited by its 2D surface. Different characterizations of the 2D surface exist: polygonal surfaces, spline surfaces, subdivision surfaces... The surface can be described in \mathbb{R}^3 as an embedded manifold.

We are working with polygonal meshes: the surface is defined by the 3D coordinates of points called vertices. Pairs of vertices are connected by edges. A close set of edges defines a face that can be any polygon, though we are working with triangular meshes only. See Fig. 1.18 for an illustration of the mesh components.

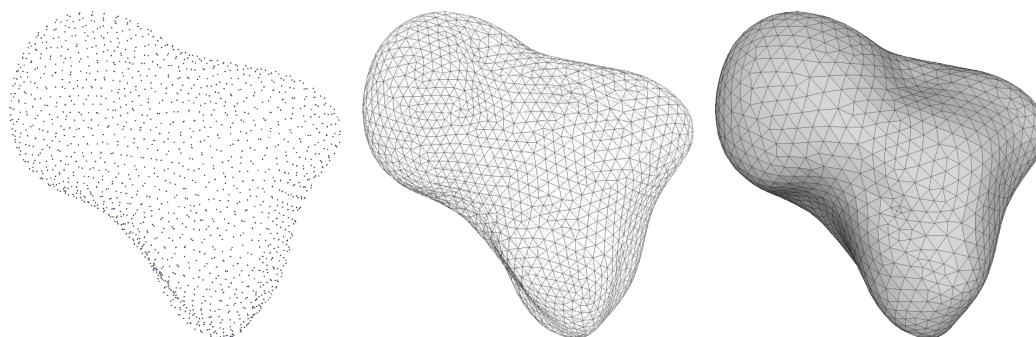


Figure 1.18: A 3D mesh is composed of a set of vertices (left), linked by edges (middle) constituting polygonal faces (right).

1.4.2 From CT scans to 3D meshes

The CT scans are composed of regularly spaced 2D grayscale images. In this section, we present how 3D meshes composed of vertices, edges and faces were created from these piles of planar images. The bones, due to their high density, are particularly visible in the X-ray images, especially their external layer, the cortical surface. As illustrated in Fig. 1.19, the construction of the polygonal meshes starts with outlining them in all images. Meshes are constructed from the piles of outlines, using various methods, introduced in the following section.

The first step of 3D meshes generation consists in bones segmentation. In every image slice of the scan, the contour of the cortical surface of every bones is delineated. For the CMC database, the outlines were manually outlined by medical students. Human experts are expected to be very precise, and should mostly avoid errors. However, such a procedure takes a very long time, considering the number of subjects, poses and slices in a CT scan. On the opposite, the NIH database was automatically segmented using a combination of thresholding and edge detection.

Two different methods were used for mesh construction from contour piles for the NIH and the CMC databases. Concerning the NIH database, Moore et al. considered the outlines as sets of 3D points, gathered in point clouds, one per bone. From the point cloud they generated the surface by tiling them with triangles, manually edited,

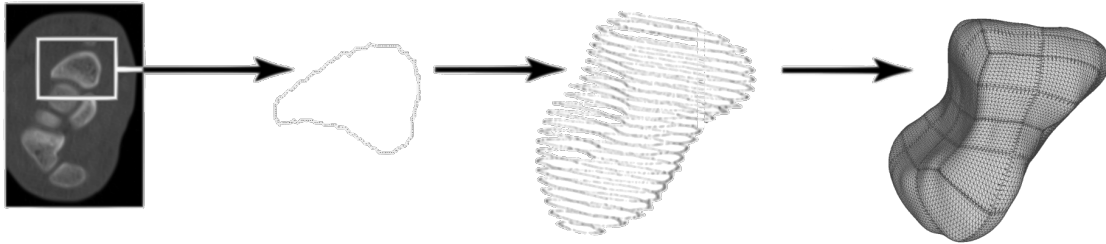


Figure 1.19: The different steps from a CT scan to a 3D mesh: in every 2D image, the bones contours are outlined. The triangular mesh is constructed from the stack of contours (from [MCTL07]). The final mesh is taken from the NIH database, which patchwork-like appearance is due to their mesh construction method.

smoothed and fitted the generated mesh with a mosaic of individual NURBS patches, using Geomagic software. The final mesh in Fig. 1.19 is a scaphoid from the NIH database, the patchwork-like appearance is due to their mesh construction method.

The CMC database meshes were generated in Brown university by Crisco and his team. The meshes were created from the manually outlined contours of the bones with the marching cube algorithm [LC87] using the Osirix software. Marching cube is a simple method which constructs the triangular 2D surface of a 3D volumetric object defined by its voxels. The algorithm considers iteratively 8 neighboring voxels, represented by the 8 vertices of a cube. Depending on the number and position of voxels belonging to the object, the algorithm resolves the presence of surface triangles through the cube, and their positions. This decision step is determined by an index of 256 different cases, reduced to 15 when considering symetries. For example, if all neighboring voxels are part of the object, no surface triangle should pass in the middle. On the opposite if one voxel is outside the object, while all seven others are inside, the surface will cut the cube. After contouring the bones in the CMC database CT scans, the volumetric objects were constructed with voxels the size of the images pixels on two directions, and heights equal to the spacing between two stacked radiographs. From these volumetric bones the surfaces meshes were constructed. The marching cube algorithm is responsible to the step-like appearance of the meshes, visible in Fig. 1.20.

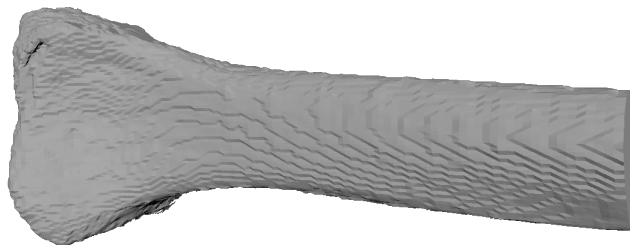


Figure 1.20: A radius mesh from the CMC database. The marching cube algorithm is the reason of the step-like appearance of the surface.

Only neutral position was segmented, the generated meshes serve as shape descriptors of the database bones. It is considered that the bones are solids that are not deformed

during motion. Shape creation from other poses is regarded as redundant information. Therefore, for both databases, poses are described by their rigid transformations only: translation and rotation with respect to the neutral wrist position.

1.4.3 Measures of similarity between meshes

Measurement of similarity between meshes refers to the evaluation of likeness between the volumes, which is equivalent to measuring similarity between their outer surfaces. Such a measure can be needed in many cases. For instance, representation of curved surfaces is a trade-off between precision and complexity. While a smaller number of elements speeds computation up, over-simplification should be avoided. Complexity depends on the number of vertices and faces, precision is measured by the similarity between surfaces. Another example for which similarity measurement is required is the case of meshes resampling. While the surface can have a satisfying compromise between precision and complexity, another mesh framework would have more interesting properties. After resampling, the comparison between the described surfaces is computed with similarity measure.

Distance between surfaces characterized by meshes is not a trivial measure. Different methods have been proposed in the literature to evaluate it. Due to mesh composition, mesh-to-mesh distances can be separated into 2 categories: *point-to-point* and *point-to-face* distances. Point-to-point distances are particularly interesting when correspondence between meshes is defined. (Please refer to Sec. 1.4.4 for further details about shape correspondence.) It can also be used if the vertices are densely and evenly distributed on the surface. Density ensures that the whole surface is well encoded, the even distribution that some regions are not too emphasized compared to others. In the point-to-point case, the distance at a given vertex is the distance to its closest vertex that belongs to the other mesh. It is measured for all vertices of the mesh. Point-to-point distance enables to speed the computation time up, but can easily be a cause of falsely high errors, due to irregular vertex distributions for instance. Point-to-face distance computes the distance from a vertex to the closest face belonging to the other mesh. It searches for the closest point on the other mesh, which isn't required to be a vertex, just to be on the mesh surface.

Surface similarity evaluation can assess *accuracy* and/or *completeness*. Accuracy represents the distance from the reconstructed mesh to its reference, while completeness evaluates the distance from the reference mesh to the reconstructed one. When both accuracy and completeness are measured, the distance is said *symmetrical*. Asymmetrical distances consider only one of the two factors. Such an asymmetrical evaluation can be useful when the data are incomplete, due to poor quality of data or occlusions in the image for instance. In these cases, if a complete model is being aligned to such incomplete data, a symmetrical distance metric can reach a minima by causing large distortions of the model. On the other hand, if only completeness is considered in this case, only the parts of the model that have a match on the data are factored in.

The nature of the distance measurement can also vary: should it give a sense of a *mean* distance across the surface, or rather a *standard deviation* or else a *maximum* distance on all surface. All these measures are commonly used: the maximum distance across

the surface is usually defined by the Hausdorff distance (1.3). The standard deviation is assessed by the Root Mean Square measure (1.2) which was used in [JLBC16]. Mean distances between the vertices and their closest vertex/face are also commonly employed [MSR⁺15]. Many variations of these measures exist, whether symmetrical or not, point-to-point or point-to-face, etc. We present one version of each.

A *symmetrical point-to-face mean mesh similarity distance* is defined as follow:

$$d_{\text{mean}}(M, N) = \frac{1}{|\mathcal{V}(M)| + |\mathcal{V}(N)|} \left(\sum_{v_1 \in \mathcal{V}(M)} \left(\inf_{p_2 \in N} \|v_1 - p_2\| \right) + \sum_{v_2 \in \mathcal{V}(N)} \left(\inf_{p_1 \in M} \|v_2 - p_1\| \right) \right) \quad (1.1)$$

M and N are the two meshes whose distance is being computed. $\mathcal{V}(M)$ (resp. $\mathcal{V}(N)$) is the set of vertices of mesh M (resp. N), and $|\mathcal{V}(M)|$ (resp. $|\mathcal{V}(N)|$) is the number of vertices of the mesh. $p \in M$ (resp. $p \in N$) can be any point that belong to a face of M (resp. N).

(1.1) measures the mean Euclidean distance between a vertex and its closest point on the other surface, for every vertices of both surfaces. If the vertices are uniformly distributed, no bias is introduced by the points distribution.

An *asymmetrical point-to-point Root Mean Square measure* between two meshes M and N is defined as follow, using the same notations as previous equation :

$$d_{\text{RMS}}(M, N) = \sqrt{\frac{1}{|\mathcal{V}(M)|} \sum_{v_1 \in \mathcal{V}(M)} \left(\inf_{v_2 \in \mathcal{V}(N)} \|v_1 - v_2\| \right)^2} \quad (1.2)$$

The Root Mean Square measure sums the squared distances between corresponding vertices, it amplifies the importance given to large gaps between two surfaces. In equation (1.2), the distance is asymmetrical, only the vertices of mesh $\mathcal{V}(M)$ are guaranteed to be all taken in account.

A *symmetrical point-to-face Hausdorff distance* represents the largest euclidean distance between a vertex and its closest point on the other mesh. The notations used are the same as the two previous distance equations.

$$d_{\text{Hausdorff}}(M, N) = \max \left(\sup_{v_1 \in \mathcal{V}(M)} \inf_{p_2 \in N} \|v_1 - p_2\|, \sup_{v_2 \in \mathcal{V}(N)} \inf_{p_1 \in M} \|v_2 - p_1\| \right) \quad (1.3)$$

Instead of considering the surfaces themselves, the volumes delineated by the meshes can also be used to estimate correspondence [HWM06, MDW08, RDD⁺14]. Several measures quantify the dissimilarity between two volumes, such as the Jaccard distance (also known as the Tanimoto distance) and the Dice coefficient (also known as the Sørensen index). They both take their values in $[0, 1]$. Let M and N be two volumes, the *Jaccard distance* is:

$$c_J(M, N) = 1 - \frac{|M \cap N|}{|M \cup N|} \quad (1.4)$$

The *Dice coefficient* between two volumes M and N is:

$$c_D(M, N) = 1 - \frac{2|M \cap N|}{|M| + |N|} \quad (1.5)$$

Depending on whether we are more interested in a similarity or dissimilarity measurement both coefficients exist in the two versions $\text{coef} = x$ and $\text{coef} = 1 - x$.

Both Jaccard and Dice coefficients are equivalent, and measure volumetric overlap. They are related according to the following equality:

$$c_J = \frac{c_D}{2 - c_D} \quad (1.6)$$

It may be noted that in computer graphics, the problem of mesh similarity exists too. However different constraints arise. While for medical data the surface precision is the only but very strong requirement, in computer graphics the results need to be visually satisfying. As illustrated in [Lav11], with identical mathematically computed errors between surfaces, meshes can look very different, and the human eye appreciates the results differently. Therefore measures taking visual appreciation in account have been developed, but are not of interest in our case.

1.4.4 Correspondence between meshes

The purpose of establishing correspondence between shapes is to define significant relationships between them. In particular, shape correspondence aims at identifying similar parts of the shapes, that have identical or comparable structures or functions, so as to be semantically meaningful. When correspondence is defined between a set of shapes, it permits comparisons between them.

Correspondence between a set of shapes S_1, \dots, S_n means that there exists a meaningful relation R between these shapes elements. Let (e_i, e_j) be elements such that $e_i \in S_i$, $e_j \in S_j$ and $i \neq j$, if $(e_i, e_j) \in R$ then these elements are in correspondence, they match each other. The relation R can be subject to various constraints, as described by Van Kaick et al. [vKZHCO11]:

- R can be a *one-to-one* relation, that is from one element of S_i towards one element of S_j , or a *one-to-many* relation, one element being allowed to be connected to multiple elements in the associated shape. Finally *many-to-many* relations can be defined.
- R can define a *dense* correspondence, that is characterized for all shape elements, while *sparse* correspondence is only defined for a subset of the elements. Indeed for some applications, such as the analysis of vertebrate movements, some representative points located at the limbs and the head are enough. An example of

sparse correspondence between a dinosaur body and skeleton is visible in the left of Fig. 1.21. In this case, the corresponding landmarks can be used to map both dinosaurs in the same pose. On the opposite, applications such as shape morphing require dense correspondence to guarantee global smoothness. An example of dense correspondence between four humans is illustrated in the right side of Fig. 1.21. The right arms being in correspondence for all humans, the shapes could be used to study the variation of the arms thickness between individuals for instance, or else analyze more precisely poses variations than with sparse correspondence.

- R can be defined for the *full extent* of the shapes, on the opposite of some methods that are able to compute correspondence for a *portion of the shapes* only.
- R can associate to each $(e_i, e_j) \in R$ a *confidence value* or not, the existence of a relation between two elements being considered enough information.



Figure 1.21: Sparse correspondence on the left (from [vKZHCO11]) compared to dense correspondence on the right (from [LRR+17]).

3D shapes described by polygon meshes are characterized by the locations of their vertices. Yet when one object has been scanned twice, it is usually defined by different meshes, with distinct number of points that are differently distributed over the surface. If we consider two meshes of a person's face, one when smiling, the other illustrating sadness, there is no natural way of studying the differences from the raw meshes. In this case sparse correspondence could define the position of the mouth corners, the nose tip and the eyes corners in both faces for instance. From the locations of these particular points, analysis could be conducted and prove that the corners of the mouth are closer to the eyes when the person smiles. Correspondence establish meaning between shapes by defining equivalences.

The shapes S_i can be multiple instances of a same object, but at various times or poses. Or they can be various occurrences of objects of the same class or of similar classes. The elements composing the shapes are the vertices in the case of 3D meshes. Dense correspondence will define equivalence for all vertices while sparse correspondence will only consider some of them. Points for which correspondence is defined are called landmarks, even when they are not in a significant place of the object. In the case of anatomical objects, corresponding vertices are expected to be in equivalent anatomical places. For instance a point at the tip of a finger will be expected to be in relation with another point at the tip of a finger, or a joint will be related to the same joint on the other

instance, etc... Various applications rely on correspondence, such as morphing, shape analysis, animations of shapes according to a leading one, and so on.

A first easy requirement to create dense one-to-one correspondence across multiple shapes is to describe all of them with the same number of vertices, while the j^{th} vertex of a shape is determined to be equivalent to all other j^{th} vertices of all other meshes. In this case, the coordinates of a 3D structure vertices can be described in a vector $v_{S_i} = [x_1, y_1, z_1, x_2, y_2, z_2, \dots, x_j, y_j, z_j, \dots]$. Equivalent vertices being defined in the same order for all meshes, vectors coordinates describe the same information across instances. If the forms were previously aligned, difference between vectors directly characterize differences between shapes. In this case we say that shapes are corresponding. This is what we aim to end up with for wrist meshes at the end of our method.

The precision of the correspondence established between elements is highly important. If the paired points are not anatomically equivalent, it inflates existing variability. A model computed using those false correspondences can produce invalid shape instances. Davies et al. illustrate this with a 2D model of hand outlines [DCT01]. For 17 hands they define two different sets of sparse landmarks, one composed of corresponding anatomical landmarks manually defined, while the points of the second set are computed based on an arc-length parameterization. Examples of corresponding landmarks of both sets are visible in Fig. 1.22. It can be observed that the second set of points in the right column are not anatomically corresponding. They compute shape models using both parametrizations, and prove that a model based on bad correspondence generates unreasonable shape instances (Fig. 1.22). They are visibly not anatomically plausible.

A huge difficulty when computing correspondence between shapes is that no generally accepted correspondence evaluation exists. It is thus difficult to assess results quality. Moreover comparison to ground-truth shapes is problematic, both because there is no unique ground-truth result for shape correspondence, and because when working with medical images, true correspondence between biological shapes are simply generally not known, making it impossible to compare results to ground-truth [SRN⁺03, HM09].

1.4.5 Correspondence: quality assessment

Correspondence between meshes is a strong property that enables many applications. It is however very difficult to evaluate the validity of the relations developed. It is in particular true for dense correspondence since all vertices are not on peculiar features, which makes it harder to define mathematical or visual validation. We introduce a few criteria that have been proposed in the literature to qualify at best correspondence quality.

A model describing the statistics of the points positions is often referred to as Point Distribution Model (PD), term introduced by Cootes et al [CTCG95]. Based on the observation that bad correspondence leads to a bad and less compact PDM (see Fig. 1.22), Davies et al. [DCT01] propose to evaluate correspondence quality based on the statistical model generated with the data. They follow the Occams razor principle

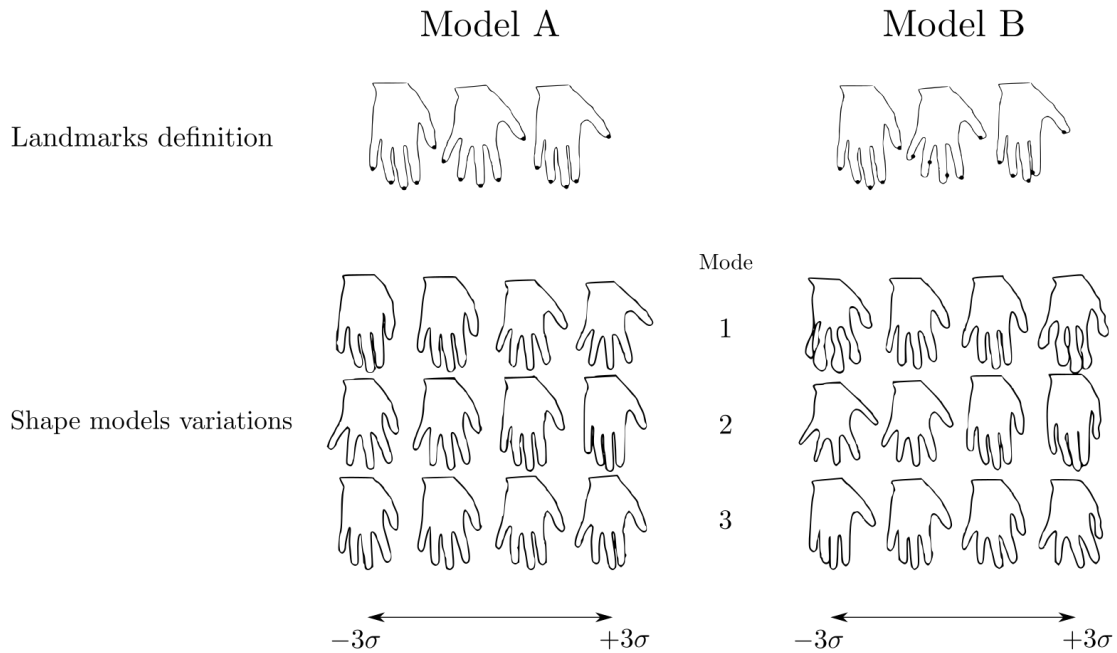


Figure 1.22: Two sets of landmarks defined on a database: one set anatomically consistent, while the other isn't. The 3 main modes of variations of shape models constructed using both sets illustrates the generation of invalid shapes when correspondence is bad.

stating that the simplest solution should be favored over more complicated ones. They list three factors that an ideal model should optimize.

The first one is *generalization*: any valid instance of the shape should be described by the PDM, not only the ones in the training set. Generalization can be measured using a leave-one-out method. A statistical model is generated based on all shapes of the training set but one, then is optimized to represent at best the element put aside. The mean distance between the model and the omitted training shape for a series of leave-one-out tests estimates the generalization factor.

The second factor is *specificity*. It represents the validity of the shapes the model can generate. It is measured by creating new elements according to random parameters generated from a normal distribution with zero mean and respective standard deviations described by the Principal Component Analysis. (For further details about PCA, please read Sec. 3.2.2.) The distances to the closest shape in the training set for each generated elements are averaged to estimate the specificity factor value. It can be noted that generalization and specificity are opposite factors, one can only be improved at the expense of the other. A balance between them needs to be reached.

The third and last factor is *compactness*. To each mode of the PCA is associated a variance, the modes are ordered from the highest variance to the smallest one. The variance of each mode can also be expressed as a percentage of the total variance of the model (the sum of all variances). The higher the first percentage variances, the more variance of the model is described with few parameters only. The less parameters are needed, the better the model is considered. This factor is based on the variances

associated to their experiment in Fig. 1.22 suggesting that a more valid model is also more compact. The factor is simply evaluated by the sum of the variances associated to the model modes.

However, these factors are not perfect for correspondence quality assessment. They are dependent on the landmarks distribution, when they are expected to quantify correspondence quality independently of any other parameter. Munsell et al. [MDW08] proved it by introducing three sets of accurately corresponding points. The three different point distributions characterize the same series of triangles. Some of these triangles are illustrated in Fig. 1.23. The distributions describe the same shapes, the resulting PDMs characterize the same shape-space. However, Munsell et al. show that the generalization, specificity and compactness factors have different values for these distributions. Ericsson and Karlsson [EK06] uncovered another issue with the specificity measure, which can not discriminate the membership to a class for some examples. C and D in their article have equal distances to their closest training shape, when C is an instance of the class and D not.

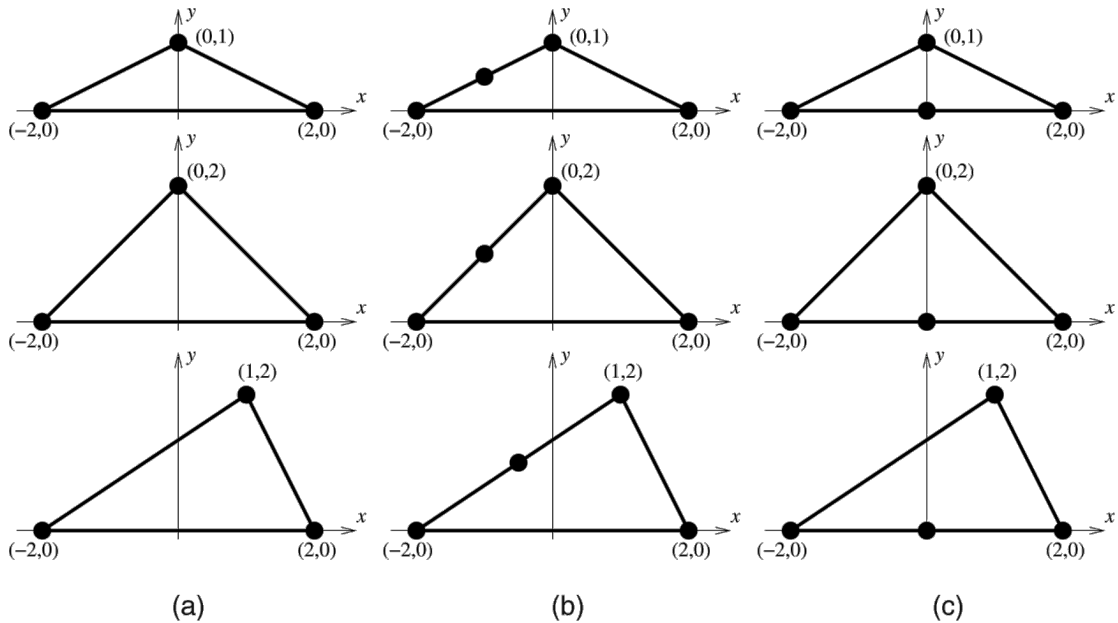


Figure 1.23: Three different landmark sets are defined for the same shapes in the three columns (from [MDW08]). In each column the correspondence is accurate. Yet the specificity factors are different (0.31 for the left and right columns, 0.39 for the middle one, for multiple modes).

Other correspondence evaluation criterion have been proposed. Instead of generating ground-truth corresponding shapes, Munsell et al. [MDW08] generate an arbitrary ground-truth shape space by defining a mean shape and a covariance matrix. Using this simulated PDM, they randomly generate shape contours. They test the correspondence algorithm with these generated shapes, and compare the shape space defined by the newly derived PDM with the generated shape space. This method enables to test a

method based on generated shapes, but can not be used to directly quantify relations quality between meshes.

For the moment few methods have been proposed to evaluate correspondence and none of them is perfect. The lack of good measure is one of the difficulty that makes correspondence computation a laborious task. In the following section, we introduce a few methods that have been proposed to compute correspondence relations between meshes.

1.4.6 Correspondence: computation

Correspondence mapping is needed for numerous applications of various fields such as medical imaging or graphics. Due to the complexity of both definition of correspondence and assessment of its quality, many works have been conducted about these issues in various domains. In this section, we will briefly introduce a few families of methods solving this problem.

A first approach consists in manually defining the landmarks. It was used by Cootes et al. [CTCG95], when they introduced the first statistical model. They manually characterized points of anatomical significance. If this method can seem to be appropriate for 2D outlines, it becomes an arduous task in three dimensions: it is harder to be precise, it requires often a lot more points, etc. Numerous other disadvantages are related to manual landmarking, such as the subjectivity of the results, which are annotator-dependent, the high time consumption, the necessity to be annotated by specialists for medical images, and so on. Some of these defects can however be improved by assistance of semi-automatic procedures, as was noted by Davies et al. [DTT08].

Manual landmarking raises too many difficulties, automated solutions have been looked for. One is based on strong similarity between shapes. The meshes are at first rigidly aligned, then equivalent vertices are defined, based on proximity, sometimes balanced with another criterion such as the angle of the vertices normals. [HMK⁺02, VdBA⁺04] are example of papers which used such a technique for correspondence definition. However, the assumption that equivalent points should be physically close is a poor criterion, as it may actually considerably vary over a training set, and lead to wrong correspondences. An example of a poor correspondence definition based on distance criterion can be seen in 1.24. Such a criterion creates possibility of surface folding.

Non-rigid alignment is an extension to rigid alignment. When the shapes have been rigidly matched, the vertices are moved freely from the reference shape towards the target surface. To keep a global consistency, regularization can be enforced through different methods such as penalization of large deformations. Neighboring vertices can also be forced to have similar transformations, to ensure a smooth resulting mesh.

When a reference mesh is deformed towards the database components, the choice of the reference shape is really important. It's been proven that it has a strong influence on the results. In Fig. 1.25, the influence of the reference chosen is illustrated through the application of image registration, since it has more visual effects. In a group of 19 MR images of the brain, two subjects were chosen as references [BHP⁺04]. They

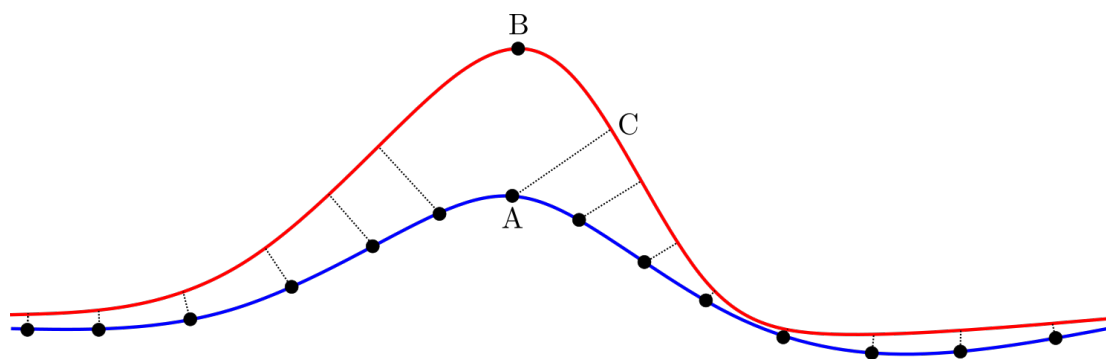


Figure 1.24: Correspondence of points based on proximity criterion may lead to false results. In these 2D curves, A and B, respectively at the top of their curves, should be in correspondence. However, A is closer to C and they are matched together.

were used separately to register all images of the population to them. The results of the two groups were averaged. It can be seen in the Fig. 1.25 that the results are very different, even though the same group of images were used. Several solutions were proposed to reduce this effect. One improvement consists in selecting as reference the subject which requires the least residual deformation to match all other subjects, in order to reduce the reference bias. Group-wise registration methods offer a solution where both the reference shape and its deformations towards the subjects are considered unknown. Two approaches perform such a registration: the backward and the forward models [DPTA09]. The first one considers the reference shape to be a noisy observation of the training shapes while the second assumes that the training shapes are noisy observations of the template, as illustrated in Fig. 1.26. The forward model is less computationally expensive, and is solved by iterations over two steps: construction of the template and registration of the template towards the training shapes [RRA12].

Non-rigid deformation of meshes for dense correspondence purposes may also be computed according to volumetric data. Indeed most medical data are originally segmented volumes extracted from imaging modalities such as CT scans or MRI. The reference mesh is non-rigidly deformed according to the volumetric data, which has in most cases been previously segmented, though the deformation step might be used both for correspondence mapping and segmentation. Example of works based on this principle are [KPL⁺03, SHD01, ZT05]. In some cases, existing meshes are even converted into binary volumetric images for correspondence mapping [SD04].

Some methods use a mapping of the mesh surface onto another surface, among which SPHARM is commonly used. SPHARM stands for Spherical Harmonics, which is the name of the set of basis functions used for the spherical parameterization. The latter is computed by optimizing the mapping of the mesh onto the sphere and minimizing angular distortion. The parameterization was first introduced by Brechbühler [BGK95], Gerig et al. [GSJ⁺01] proposed shape analysis using the SPHARM parameterization. Correspondence is defined to be between surface points that map to the same position on the sphere, after aligning all shapes by their first order ellipsoid. A limitation of SPHARM is its restrictive capacity to only represent objects with spherical topology.

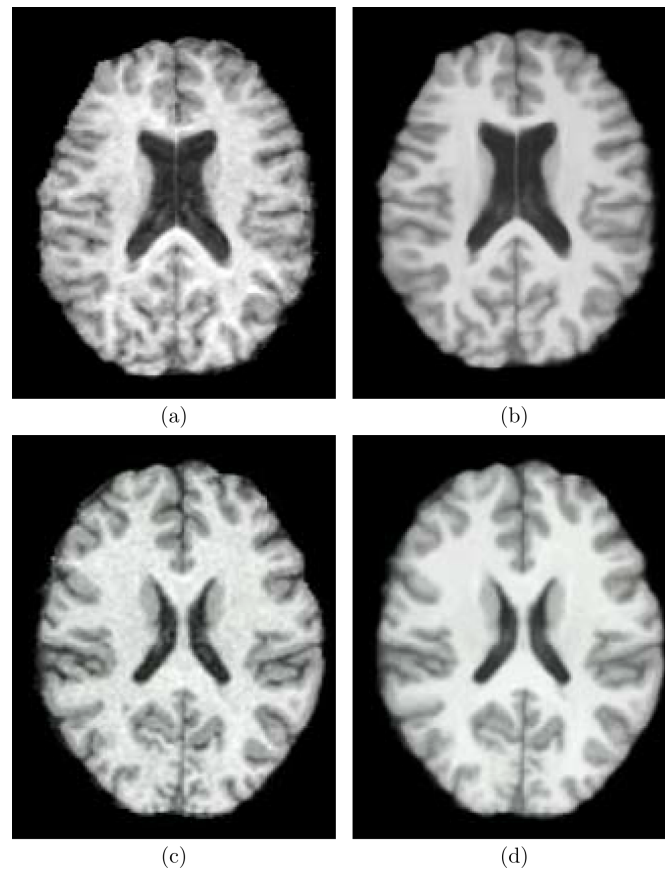


Figure 1.25: Illustration of the influence of the reference image on the registration results. (a) and (c) are two reference images used to register a group of 19 brain MRI. (b) and (d) are the respective results of averaging over the group of registered images (from [BHP⁺04])

While these methods guarantee a diffeomorphism between all shapes, the obtained correspondences are mostly arbitrary and the quality of the resulting SSM will strongly depend on the input shapes [HM09].

Some authors consider the correspondence problem as an optimization one. One such state-of-the-art method is called Minimum Description Length (MDL) [DCT01]. The minimum description length principle has an information theoretic foundation. It says that the best model is the one that describes the entire training set as efficiently as possible. By casting an objective function based on this principle, they compute the optimal parameterization of each shape of the training set. The extension to 3D shapes was introduced in [DTC⁺02].

Some other methods have been proposed to compute correspondence between meshes, such as volume-to-volume registration or physical properties-based methods for instance. Further investigation on these methods can be read in [DTT08, HM09].

Only few comparative works have been conducted over the correspondence methods. Styner et al. [SRN⁺03] compared a semi-automatic method with a parametric

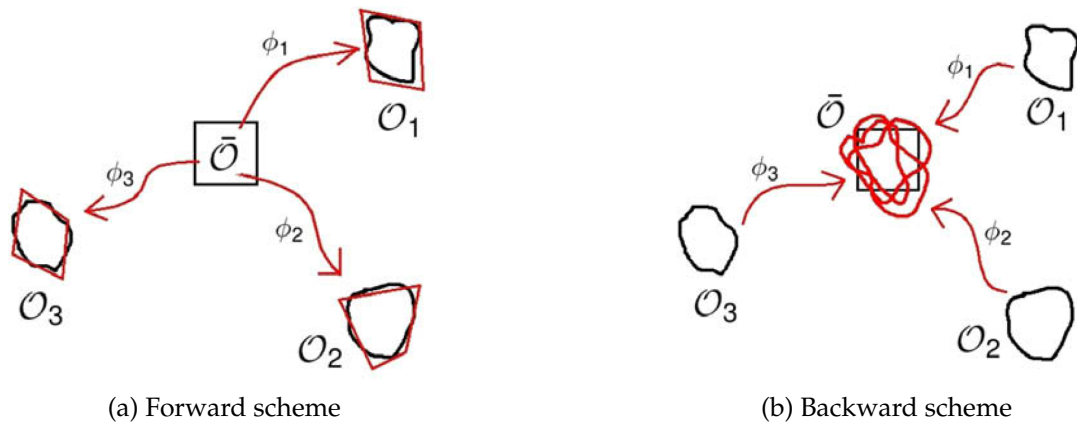


Figure 1.26: Two different approaches exist for the group-wise registration. In the forward scheme, the training shapes \mathcal{O}_i are seen as noisy observations of the unknown template $\bar{\mathcal{O}}$. In the backward model the template is a noisy observation of training shapes (from [DPTA09]).

surface description (SPHARM), an optimization method based on the determinant of the covariance matrix and finally the MDL method. His conclusions were that the two optimizations methods (MDL and determinant of the covariance matrix) were the best according to the three factors generalization, specificity and compactness.

1.5 Dense correspondence for wrist bones

In the previous section were introduced the dense correspondence property for 3D meshes and the main existing methods to create correspondence in sets of shapes. We are now interested in the small body of research addressing the dense correspondence problem for wrist bones. Wrist bones can pose particular problems due to their complex shapes and their small size compared to the acquisition data precision. Moreover methods for single shapes based on intrinsic representation of meshes are excluded, a wrist being composed of a set of bones which are often considered as a whole. We are interested in the multiple solutions that were proposed in the literature to solve the correspondence problem for carpal bones. We pay particular attention to the validation procedures proposed.

1.5.1 Existing technique

In [vdGFS⁺10], van de Giessen et al. introduce one of the first statistical shape model of carpal bones. They focus on two carpal bones, the scaphoid and the lunate. To build their model based on dense correspondence, they use the same method as in one of their earlier article [vdGSS⁺09]. The meshes are at first rigidly aligned, using unbiased Iterative Closest Point. The Iterative Closest Point algorithm (ICP) is a commonly used method. It was first introduced in [CM92] and [BM92]. The procedure computes the optimal rigid transformations between two point clouds. It starts by associating to each point of the source point cloud a point of the reference point cloud based on a minimal distance criteria. The optimal translation and rotation are then computed, such that they minimize the root mean square distances between the pairs of points. The optimal transformations are applied to the source point cloud and the algorithm reiterates by computing new pairs of points, and so on. Correspondence is then established by identification of pairs of points on the surfaces. Given a point, its match on the other mesh is the point that minimizes the distance between both their coordinates and their surface normals. The bones are resampled with 15000 vertices each. The statistical models are used to study the shape variations of both bones. In another following article [vdGFV⁺11], correspondence is computed using the previous statistical models, which are being registered to the new wrist bone surfaces, according to the models deformation vectors. The newly corresponding bones are being used to study the relative movement of adjacent bones in a joint. Study of normal behavior of a joint can be used for pathological wrist detection or else reconstruction of a physiological wrist for surgery.

Chen and his team who apply a Minimum Description Length algorithm on their papers [CGHM11, CGHM12] based on Davies work [DTCT09]. Using corresponding meshes for shape characterization and bones rigid transformations for pose description, they build a statistical model. They use it to infer both carpal bones shapes and poses from single-view fluoroscopic sequences. In [CGHM13], they use a statistical model to automatically segment 3D volumes (CT or MRI). The segmented bones are then directly in correspondence. As for van de Giessen et al. works, no measurement of correspondence quality is given.

Chaudhari et al. compare carpal bone shapes in [CLW⁺14] by modeling the surfaces as vibrating membranes based on spectral theory, introduced in [Rus07]. They use intrinsic representation of the meshes, which they can do due to their interest to each bone individually. The coordinates of the shapes in the new space are defined by the Laplace-Beltrami operator eigenspectrum. This spectral descriptor is called Global Point Signature. The space of representation has a Euclidean metric, comparison of shapes is measured in this space. In the GPS representation, each vertex of the original mesh is embedded into an infinite dimensional space. However, for practical reason, the shape signature is truncated, but no measure of the error made with the truncation is given.

Joshi et al. propose a non-rigid registration algorithm for carpal bones in [JLBC16] based on atlas warping. Their method starts with the selection of an atlas individual, the person whose wrist is the most similar to all others. It is defined as the one minimizing the sum of the pair-wise distances between all its bones with all bones of all others subjects, after rigid registration. They use a Root Mean Square distance metric:

$$d_{\text{Joshi}}(M, N) = \sqrt{\sum_{v_1 \in \mathcal{V}(M)} \left(\inf_{p_2 \in N} \left\| \frac{v_1}{A(M)} - \frac{p_2}{A(N)} \right\|^2 \right)^2} + \sqrt{\sum_{v_2 \in \mathcal{V}(N)} \left(\inf_{p_1 \in M} \left\| \frac{v_2}{A(N)} - \frac{p_1}{A(M)} \right\|^2 \right)^2} \quad (1.7)$$

M and N are the two surface meshes compared. $\mathcal{V}(M)$ (resp. $\mathcal{V}(N)$) is the set of vertices of M (resp. N) while $p \in M$ (N) designates any point p who is part of M 's (N 's) surface. Finally $A(M)$ (resp. $A(N)$) is the surface area of the mesh. It is used to normalize the bones.

When the atlas subject has been chosen, its wrist is deformed to warp those of the database, each bone being considered separately. This non-rigid registration is composed of two steps: first the database bones are rigidly aligned towards the atlas, using the Iterative Closest Point (ICP) algorithm (please refer to Sec. 2.2.3.a for further details about the ICP algorithm). Then the atlas surface is non-rigidly deformed based on the minimization of a cost function using gradient descent, as first introduced in [JCL⁺10]. The cost function factors both the distance between the paired meshes and the smoothness of the deformation field in. The deformation of a reference mesh towards the bones of the database gives a correspondence between shapes. They use correspondence to analyze bone shape variations both between male and female and between left and right wrists. They also prove that they can use their method to detect and track erosive changes in the carpal bones.

Finally, Anas, Rasoulian et al. propose several works about wrist shape and pose modeling and used it for diverse applications such as CT scans segmentation and surgery assistance via model registration to ultrasound images [ARJ⁺14, ARJ⁺15, ARS⁺16, ASR⁺16]. Their method to compute correspondence between shapes was introduced in [RRA12] and is based on soft correspondence between point sets based

on a group-wise Gaussian Mixture Model registration technique. Correspondence is computed using a forward group-wise registration model, decomposed in two steps: non-rigid registration of the template towards the shapes and update of the template as the mean shape using Quasi-Newton method. Correspondences are seen as probabilities instead of one-to-one relations. The template is considered to be a probability distribution: its vertices are assumed to be centroids of a Gaussian mixture model. The training shapes are observations generated by the distribution, non-rigid transformation becomes a probability density problem. It is solved using an expectation-maximization algorithm.

1.5.2 The problem of validation

We are interested in the quality of the methods previously presented. But none of these works focuses on the validity of the mapping method. And whether based on private databases as for [vdGFS⁺10, CGHM12] or based on the public NIH database like in [ARJ⁺14, JLBC16], none of the results are public, which makes it harder to compare their results. In most cases, correspondence was used to build statistical models. Yet it has been proven that bad correspondence introduces false variations in the models (Fig. 1.22).

In [JLBC16], Joshi et al. do not evaluate their correspondence method, but they measure the distance between the database meshes after rigid alignment, and after non-rigid registration to prove that their deformed atlases represent well the database bones. The distance metric they use (1.7) is a l^2 based pseudo-distance metric that sums distances between closest points. However the absence of division by the number of points makes this distance dependent on the number of vertices of the mesh. The exact number of vertices per mesh in their model is not given in their work, there are said to be "approximately 5000 nodes". It makes comparison with their meshes distances impossible.

Anas et al [ARJ⁺14, ARS⁺16] based their correspondence method on a previous paper [RRA12]. In the latter, they detail the correspondence method and apply it to vertebrae and hippocampi shapes. They assess the correspondence quality by measuring 3 factors: compactness, generalization and specificity. They compare their method to 4 others: a point sets affine registration from Hufnagel et al. [HPE⁺08], a backward model by Chui and Rangarajan [CRZL04], a SPHARM-PDM method by Styner et al. [SOX⁺06] and an intensity based method by Balci et al. [BGSWI07]. They prove on their two data sets that their method performs overall better than the other algorithms. They use the same correspondence method for carpal bones, but do not calculate the 3 factors for this new data set. In none of their articles they compare the database shapes with the ones in correspondence.

1.6 Conclusion

Four main themes have been approached: an anatomical and biomechanical introduction of the wrist joint; a description of how the *in vivo* data were captured by scanning various wrists in a few poses; a summary of properties of 3D mesh approaches employed in the following work; a panorama of existing works about carpal bones modeling and applications. The remainder of the document rests on these definitions.

It must be noted that concerning mesh correspondence, although these relations are very useful in several domains, no common agreement on an optimal method has been reached. This is mostly due to the lack of exact measures to quantify correspondence quality. Many solutions were proposed, but few comparative works were conducted. Some papers address this problem for wrist bones, which have various complex shapes. But validations of these approaches are always partial. Therefore we attach importance to quantification of error.

In the next chapter, we propose a method to transform the raw CMC database and reparameterize the bones into corresponding meshes. A list of all existing methods with similar purposes were presented in Sec. 1.5. Quality of correspondence relations cannot be measured by direct means. We attach importance to prove that at least the generated corresponding meshes characterize the same 3D bones than the original ones. Studies of bone shapes resting on the reparameterized data wouldn't make any sense if the volumes were distorted compared to the actual people's bones.

CHAP. 2

WRIST MODELING WITH DENSE CORRESPONDENCE

Contents

2.1	Introduction	47
2.2	Method presentation	49
2.2.1	Method overview	49
2.2.2	Preprocessing	49
2.2.2.a	Post-segmentation processing (1)	49
2.2.2.b	Resampling (2)	52
2.2.2.c	Initial alignment of the wrists (3)	53
2.2.3	Template set creation (4)	55
2.2.3.a	Template selection	55
2.2.3.b	Template creation	56
2.2.4	Dense correspondence mapping	56
2.2.4.a	Affine registration (5)	57
2.2.4.b	Laplacian Surface Edition	57
2.2.4.c	Non-rigid registration: Laplacian deformation (6)	58
2.2.4.d	Non-rigid registration: projection along the normals (7)	59
2.2.5	Results	60
2.3	Numerical Validation	62
2.3.1	Preprocessing	62
2.3.1.a	Post-segmentation processing (1)	62
2.3.1.b	Resampling (2)	63
2.3.1.c	Initial alignment of the wrists (3)	64
2.3.2	Template set creation (4)	65

2.3.3	Dense correspondence mapping	67
2.3.3.a	Non-rigid registration: Laplacian deformation (6) . .	67
2.3.3.b	Non-rigid registration: projection along the normals (7)	70
2.4	Conclusion	72

2.1 Introduction

In this chapter, we present a dense correspondence mapping method, which is applied to 8 carpal bones, 5 metacarpals and the radius of around forty wrists of the CMC database. The ulna is left out, the pronation-supination movement is not a focus of the study, and the radius alone is used as reference. The carpal bones raise particular difficulties for correspondence mapping, as they have various complex shapes, which need to be precisely captured. Whether for bone shape analysis, study of shape influence over each other or detection of bone erosion, precision in bones descriptions and in inter-correspondence is of high importance and particular attention is paid to the results quantitative evaluation. We also endeavor to propose a method easily implementable and reproducible.

We present a correspondence method based on the deformation of a template using a mesh deformation method: Laplacian Surface Edition [SCOL⁺04]. The chosen templates are initially bones from the database. To reduce particular details effects these chosen meshes are smoothed and downsampled to speed up computations. The deformation of the template towards the target shapes is computed following a forward group-wise registration model. The template is registered to the database meshes, then it is updated by averaging every vertex positions. These steps are iterated, the update of the template allows to reduce its influence. Finally, we use a simple local projection along the normals of the vertices towards the target shape to refine the results.

From all the existing methods for carpal bones correspondence definition, the method proposed by Joshi et al. [JLBC16] is the closest to ours. Indeed, we also use templates selected from the database, that are deformed to match the target meshes. However important differences exist between both approaches. At first, we have chosen to select each template independently, while in [JLBC16] they all come from the same wrist. We justify the independence of the templates choice with the mapping of each bone which is computed separately anyway, the most important parameter is that the bone should not be too specific. Indeed it has been proven that the template chosen has an impact on the following results. We use an iterative deformation, with visual inspections at every steps for control if need be. It provides a more local control on the results than the minimization of a cost function in an analytical way like in [JLBC16]. Moreover if proved to be necessary, the deformation could be guided manually. We propose to use a forward group-wise registration model, that iteratively deforms the template towards the targets and then updates the target meshes. It's been proved that updating the template is important to limit the initial template influence. On the other hand, in [JLBC16], the templates are being deformed only once. Finally we have added a last step of projection along the normals to optimize surface similarity.

As illustrated in chapter 1, dense correspondence is a strong property for polygonal meshes, that is required for many applications. However, it is also a property that cannot be easily verified, as no objective metric exists to validate or evaluate it. In the absence of such an unbiased criteria, other tests must be used to prove that if the error can not be exactly measured, it lies nonetheless within a limited range.

We have chosen to use several metrics to compare similarity between meshes. Two point-to-face distances between surfaces are used, one that measures the mean distance between the vertices and their closest point on the other mesh (1.1), and the Hausdorff distance that measures the maximum distance between a vertex and its closest point on the opposite mesh (1.3). Both are symmetrical and evaluate both accuracy and completeness since we want to avoid both folds in the deformed template and missed details from the target shape. Two other volumetric metrics are used, the Dice coefficient and the Jaccard distance, that are based on the overlap between two volumes. Both are given, though they are related. These metrics values are intended for comparisons with future methods that would like to compare their results with our algorithm.

In this chapter, we pay particular attention to assess every step of the process. We guarantee an upper bound on errors and show that our meshes can be trusted to be used for any application wanted. We prove that the output mesh outline very similar 3D volumes than the initial database meshes, and a statistical shape model is used in the next chapter to measure the 3 factors: generalization, specificity and compactness.

2.2 Method presentation

2.2.1 Method overview

We propose a correspondence method based on the deformation of templates, one for each bone, towards the database meshes. The original shapes are chosen among the database, then are modified in order to present convenient features, such as a balanced vertex count, respecting an equilibrium between lightness of calculation and precision of the data. We also work with uniform meshes, with homogeneous distribution of vertices and faces of the same size. The deformation is a composition of a first smooth detail preserving deformation, followed by a second registration to capture the sharp structures of the contours. A flowchart of the different steps is presented in Fig. 2.2, the mesh notations used in the rest of the document are given in Fig. 2.1. The steps leading to the final results are numbered from (1) to (7) as introduced in Fig. 2.1.

We are interested in 14 bones of the wrist joint: the 8 carpal bones, the 5 metacarpals and the radius. We chose to leave the ulna bone out. This bone is indeed important in the elbow articulation and plays a critical role in the pronation-supination movement of the forearm, but has a minor impact on the wrist articulation. It is however over present in the data due to its size: the number of vertices needed for a 3D mesh representation is more than the double of vertices required for one of the carpal bone. This overrepresentation affects the statistical models. For these reasons it was put aside, the radius alone is used as stable reference of the forearm.

2.2.2 Preprocessing

The initial input data we are working with are meshes of the CMC database, direct outputs of a marching cube algorithm. The meshes $M_{O,\{b,i\}}$ are raw, composed of many vertices irregularly spread along the surface, connected by irregular triangles forming the faces, as illustrated in Fig. 2.3. The irregularity of the vertices distribution can skew the distance measures between meshes. Some meshes also exhibit artifacts originating from the segmentation step. These artifacts are coarse inaccuracies that need to be removed before analyzing the bone shapes. Finally the wrists have various locations and need to be aligned. The only treatment they have undergone is that left wrists have been mirrored, so they all are right wrists. For all these reasons, the raw data could not be used as is, and required an early processing step.

2.2.2.a Post-segmentation processing (1)

The first treatment was to remove all artifacts of the data. There were different types of artifacts: one vertex that was obviously wrong compared to its neighbors, independent sets of points not attached to the bone surface that were floating inside the bones, different types of groups of vertices forming bulbs inside or outside the cortical surface. Some examples of defects can be seen in Fig. 2.4. All these coarse errors indubitably originated from the original segmentation and had to be removed. The erroneous vertices were manually selected and eliminated. The gaps created by the deletion of some faces were closed by adding triangles between the remaining

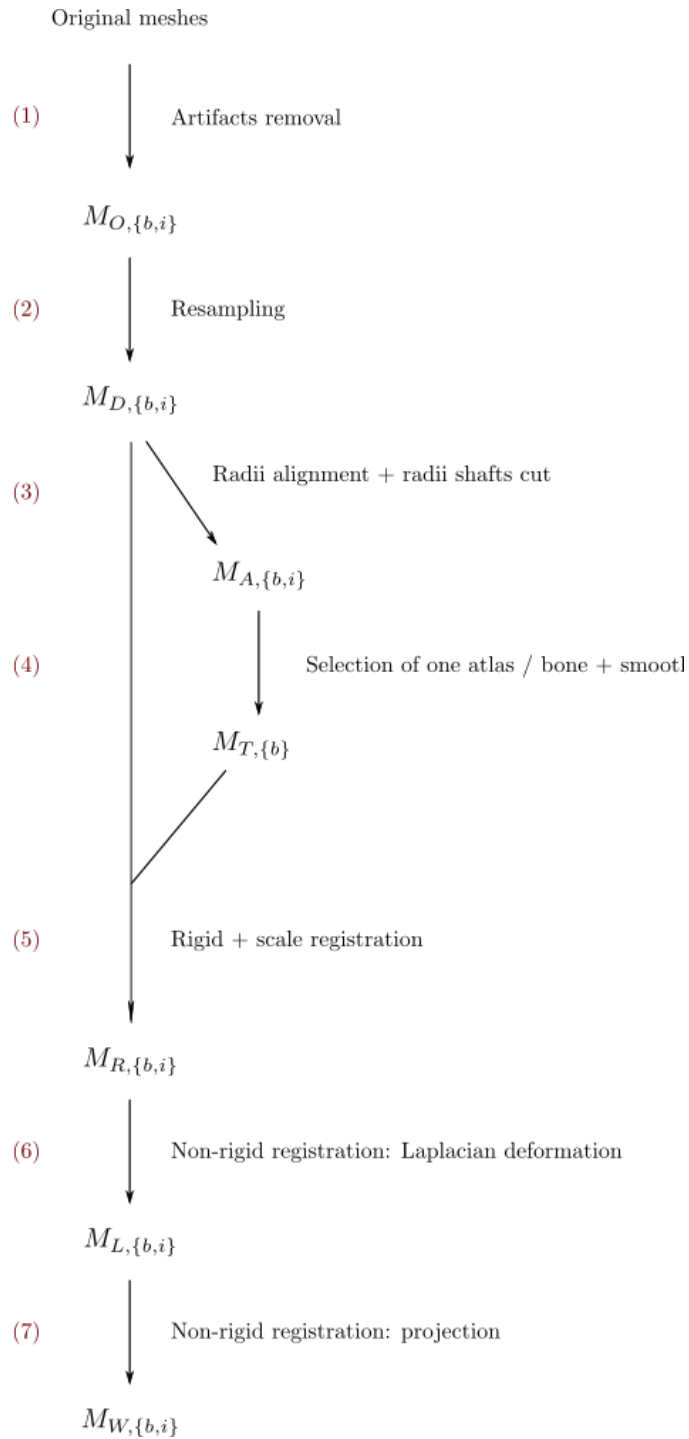


Figure 2.1: Notation of the meshes generated at each step of the method. b indicates the wrist bone, i indicates the subject of the database the mesh represents.

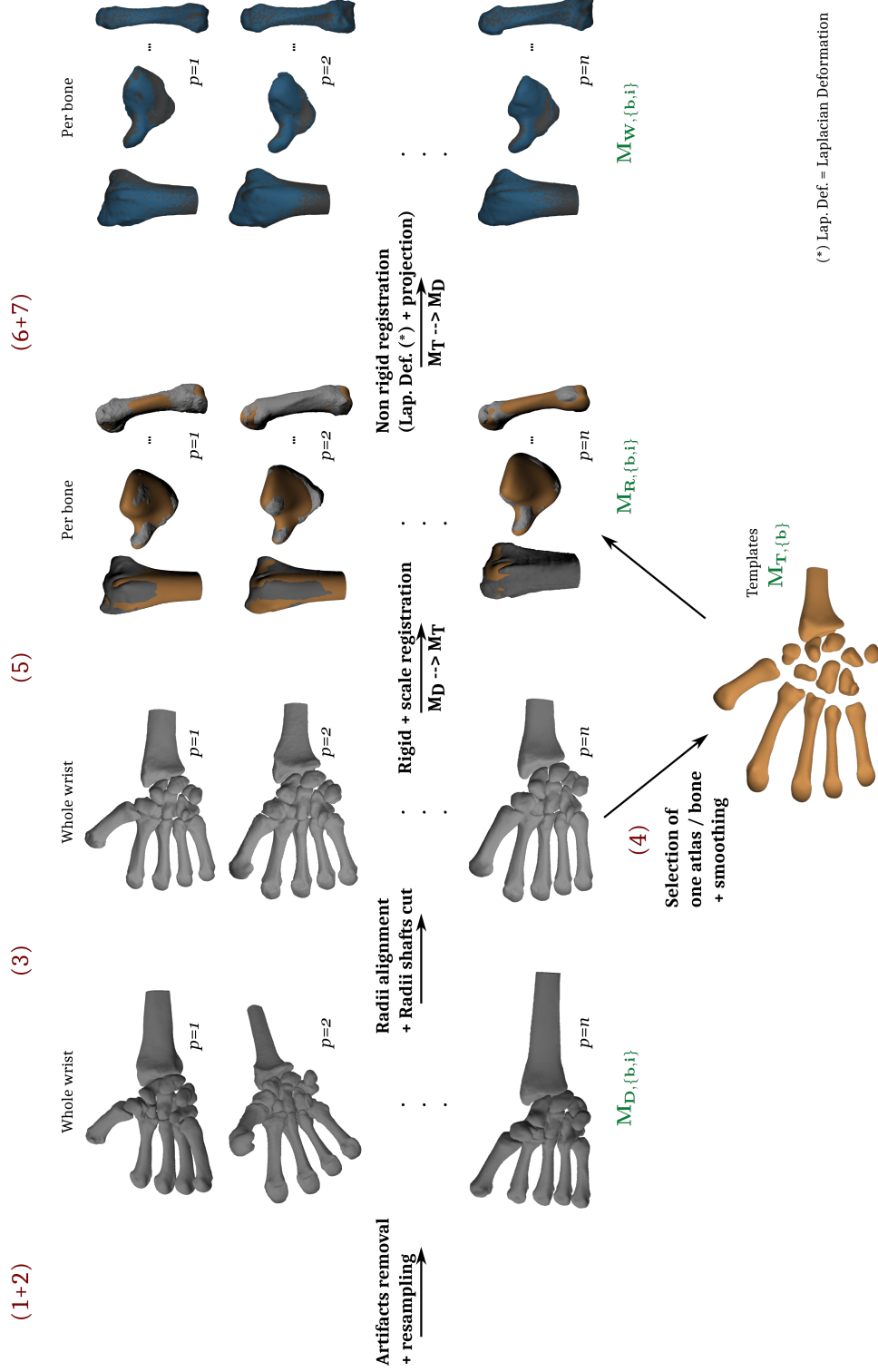


Figure 2.2: Flowchart of the different steps leading to dense correspondence between similarly shaped meshes.

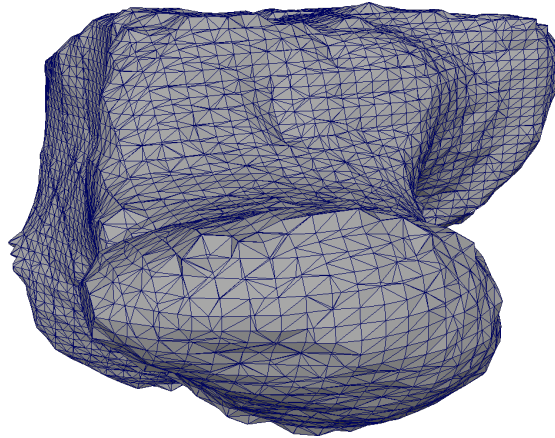


Figure 2.3: Example of an initial input 3D mesh.

neighboring vertices. The resulting meshes are referred to as $M_{O,\{b,i\}}$, b indicates the bone represented by the mesh, i specifies the subject.

2.2.2.b Resampling (2)

When the bones have been cleared of inopportune coarse inaccuracies, the second process consisted in changing the points distribution on the surface. The same number of vertices is kept for each mesh, but they are regularly spread along the surface. Indeed the irregular distribution can skew the distances, due to conglomerates of points. The resampling method is based on Centroidal Voronoi Tessalation, and guarantees an homogeneous output surface, with a stable edge length [ADVDI05].

The procedure uses Voronoi diagrams, which define a partitioning of a surface into regions (cells) based on a set of seeds of that surface. One region is associated to every seed and consists of all surface points closer to that seed than to any other. In the case of a mesh, the seeds are its vertices, the Voronoi diagram is computed for the mesh surface. To move the vertices into an homogeneous distribution, the Lloyd's algorithm is used. Based on the Voronoi diagram of the mesh, the centers of mass of the cells, also called centroids, are computed. Each vertex is moved to the position of its associated region's centroid. The new Voronoi diagram is computed, as well as the new centroids, etc. These steps are iterated and converge to a centroidal Voronoi tessellation, which is a Voronoi diagram such as its seeds are also the centroids of its cells. These seeds are the positions of the new vertices. The Lloyd's algorithm can change the topology of the mesh, and allows a partitioning into triangles nearly equilateral.

The resulting meshes are the ones used for the rest of the work as the target database meshes. The homogeneous distribution of the vertices guarantees a more representative outcome. They are referred to as $M_{D\{b,i\}}$, b is the bone index, i is the subject index.

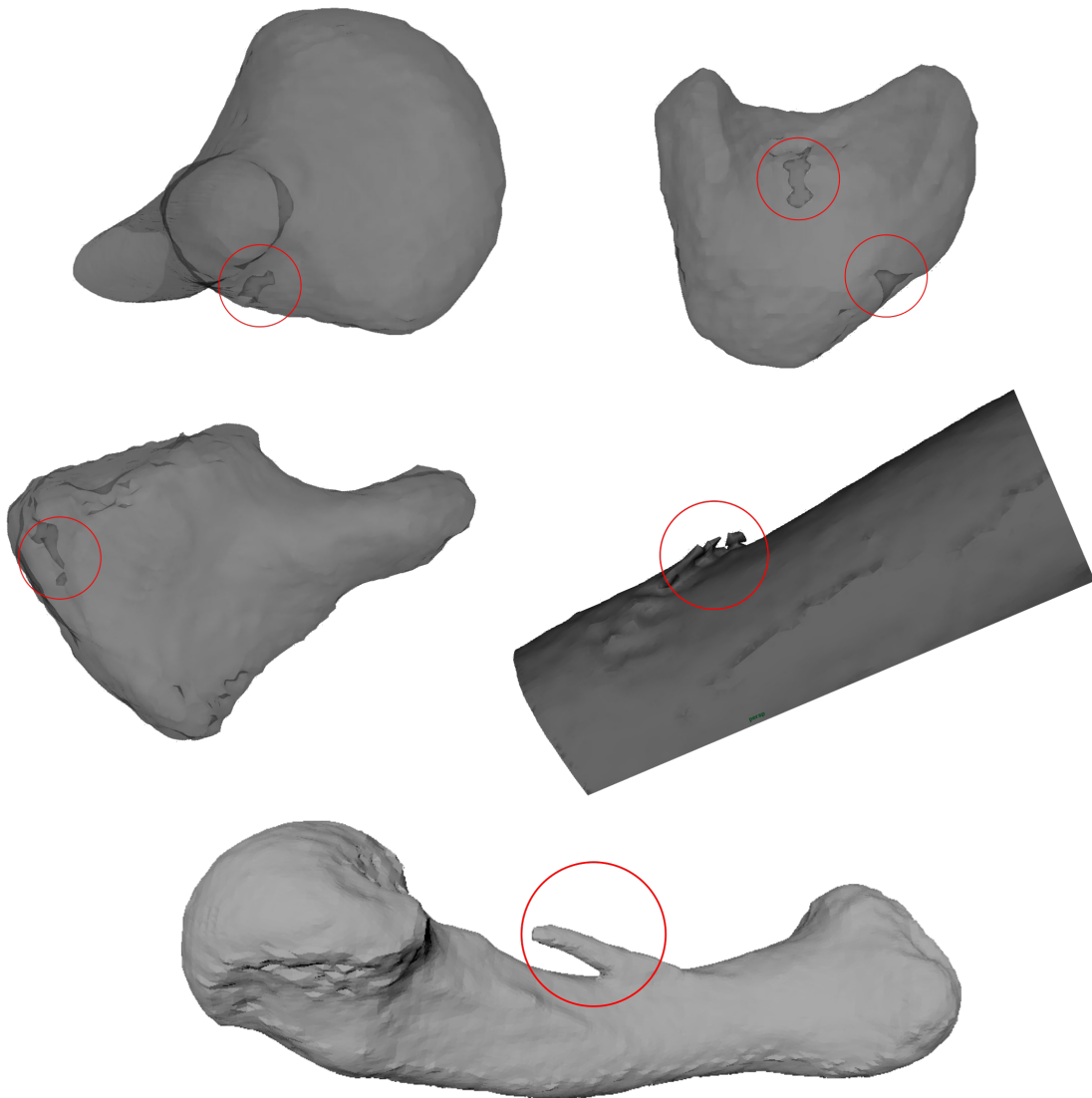


Figure 2.4: Example of anomalies present in the initial input 3D meshes.

2.2.2.c Initial alignment of the wrists (3)

Following the resampling step, the database bones $M_{D,\{b,i\}}$ are characterized by uniform 3D meshes. Distances can be computed without being influenced by an uneven distribution of vertices across the surface. They are however not aligned yet.

Alignment is in our case an absolute necessity. We have chosen to work with extrinsic characterization of the meshes, the vertices are described in \mathbb{R}^3 , using external origin point and system of coordinates. Comparison between meshes described in such a way requires a previous rigid alignment of the bones: identical shapes can have considerably different representations due to isometric transformations. It leads to falsely high distances between structures, unless these shifts have been previously canceled. Isometric transformations designate translations, rotations and reflections,

but only the two first ones are present between analogous bones in the database. We chose to get rid of scale differences too, by computing isotropic scaling. Size is the main parameter to bone shape differences between genders [JLBC16], we are more interested in shape disparities after normalization.

We use an Iterative Closest Point (ICP) algorithm for a affine alignment of corresponding structures. However, tests demonstrated that the method does not converge to an accurate lining up of the bones unless the shapes are already coarsely aligned. We therefore propose a first step to roughly adjust the meshes. We define for each subject a new system of coordinates attached to the radius, characterized by radius features. The bone meshes are described in the new system, which approximately places the wrists in the same positions and orientations. We define this new system of coordinates as (X_r, Y_r, Z_r) for every subject. In [CUC07], they define a radial coordinate system such that the X axis coincides with the radial long axis, the Y axis is directed through the radial styloid and perpendicular to the X axis. The Z axis is simply the cross product of X and Y . Our system of coordinates (X_r, Y_r, Z_r) was inspired from the one described in [CUC07].

At first, the radius minimum oriented bounding box is computed. It designates the smallest rectangular cuboid within which all vertices of the object lie. The polyhedron orientation coincides with main orthogonal directions of variance of the item points.

The X_r axis is defined as the line parallel to the longest edges of the bone's bounding box, going through both centers of the faces perpendicular to these edges. This axis is a good approximation of the radial long axis. It is directed from the radial diaphysis (the middle tubular part of the bone, see Fig. 1.2) towards the carpal extremity. We denote y the point at the extremity of the radial styloid process (see Fig. 1.2). It is the point whose perpendicular projection on the X_r axis has the biggest coordinate. Its perpendicular projection on X_r defines the center of the system. Y_r is directed from the system center towards y . Z_r is the cross-product of X_r and Y_r . The unit length in all three directions is 1mm. The carpal bones expressed in this new system are coarsely aligned across the population. An illustration of such a system is visible in Fig. 2.5.

When the meshes are described in this new bases, the radii are coarsely aligned, and so are the wrist bones, which have undergone the same transformations (rotation, translation). In this new basis the meshes are ready to be used, the affine ICP algorithm converges.

The portion of the radius diaphyses visible on the CT scans is very variable across the population. To overcome these fluctuations, a last treatment is applied to the database radii: the radius shafts are cut on the proximal side, following the first alignment. They are carved along the plane perpendicular to the X_r axis. The length kept along the X_r axis is a constant proportion of the height (along Y_r) of the bone. The proportion was chosen to be the biggest possible, that is available for every subject. The resulting aligned and cut meshes are referred to as $M_{A,\{b,i\}}$.

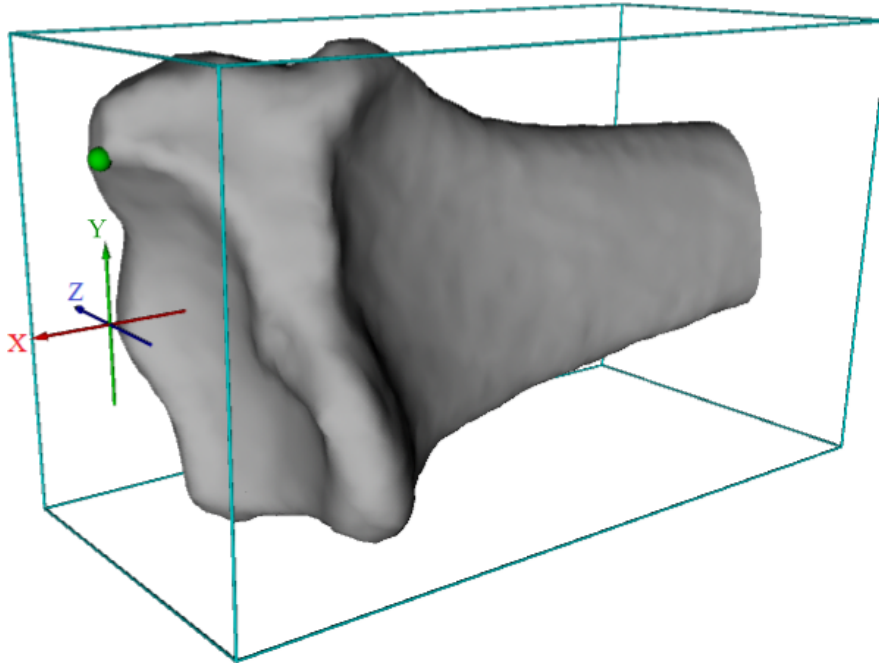


Figure 2.5: The radius-based coordinate system.

2.2.3 Template set creation (4)

We chose to compute correspondence between shapes by deforming a template towards the database meshes. Templates are chosen among the subjects' bones, to ensure close shape similarity between the original and target meshes. They are also prepared in order to present convenient properties, such as a good balance for vertex density.

2.2.3.a Template selection

The choice of the template is important, if its shape is too different from the ones it must adapt to, the results will be imprecise, miss details or else the deformations are so significant that it produces poor correspondence. Many iterations of registration and template updating might be a solution, but it would require a long time to get to a satisfying result. We start with templates already very close to the structures they are registered to. The best mean to have a close contour of the target shapes is to use database bones as templates. The registration of the bones is computed independently for each bone of a person, the template can also be selected independently. The selected meshes are then smoothed to remove sharp details specific to the individual bone. The templates should have desired mesh framework features, such as convenient edge density. Like in [JLBC16], we chose the templates among the database bones as the ones the closest to all other, they are the ones with the least specificity.

A reference mesh is selected for each one of the $B = 14$ bones among the database individuals I_{CMC} . The reference mesh of the b^{th} bone ($1 \leq b \leq B$) is chosen for being the one that is the most similar to the corresponding bones of the rest of the population.

The choices are independent, selected bones may come from different subjects. The similarity of the b^{th} bone of a person j to the rest of the population is measured as follow: its mesh is aligned to the equivalent bone of all other subjects $i, i \neq j$, one after the other, using ICP. Then the distance $d_{\text{mean}}(M_{D\{b,i\}}, M_{D\{b,j\}})$ between the rigidly aligned pair is computed using the mean distance (1.1). For each bone, its distances to all other equivalent bones are added up. The smallest sum across the subjects designates the reference mesh $M_{t\{b\}}$ for this bone.

$$M_{t\{b\}} = \min_{j \in I_{\text{CMC}}} \sum_{i \in I_{\text{CMC}}, i \neq j} d_{\text{mean}}(M_{D\{b,i\}}, M_{D\{b,j\}}) \quad (2.1)$$

We compute the rigid alignment with Iterative Closest Point (ICP) (1.5.1). To optimize the isotropic scaling simultaneously, we iterate between the optimization of the rigid transformations using ICP and the scaling.

2.2.3.b Template creation

To erase sharp details that are too specific to a given individual, the selected meshes are smoothed using five steps of Laplacian smoothing. A Laplacian smoothing consists in moving every vertex of the mesh towards the average location of its topological adjacent vertices. Applying this transformation five times shrinks slightly the shape, but mostly smooths sharp details.

We want to work with meshes that have a convenient edge density, which strikes a balance between detail precision and computing time. Therefore the smoothed meshes are resampled in order to get regular edge lengths of 1mm. The bones have various number of vertices, that are regularly distributed along the surface. It divides by 6 to 8 the number of vertices compared to the original meshes, highly speeding up computations. Tests have proven that no important loss of information is caused by this decreased number of points, compared to meshes with edges of 0.5 or 0.3mm, while the calculation time substantially decreases. In the end of the process, the corresponding bones will have the same number of vertices as the templates, and should also have a mean edge length of approximately 1mm, though by definition, points should not be exactly at the same distance from each other. The resulting templates that are used for the rest of the work are referred to as $M_{T\{b\}}$.

2.2.4 Dense correspondence mapping

The templates having been selected, they are non-rigidly registered to define dense correspondence across the database. The deformed meshes should fit perfectly the individual shapes, preserving all details. With such a registration, dense correspondence between the population is natural, and can be used for various applications such as shape comparisons or else statistical shape studies. The deformation is computed in two steps, presented in this section. At first they are smoothly deformed using Laplacian Surface Edition [SCOL⁺04]. These deformations are iteratively calculated, until an arbitrary precision is met and satisfactory visual results are obtained. This deformation

meets its limits on sharp details representation. Therefore a second registration step is performed, which is a projection along the normals towards the target shape.

2.2.4.a Affine registration (5)

The meshes encoding the database information are the original shapes that have been resampled once. They are referred to as $M_{D,\{b,i\}}$. The templates meshes, one for each bone, are referred to as $M_{T,\{b\}}$. We aim at representing the database bones with the same set of vertices for each individual. This is achieved by deforming the templates, to fit the bones of the sample wrists.

The very first step is to rigidly register the database bones $M_{D,\{b,i\}}$ towards the templates $M_{T,\{b\}}$, using affine ICP. This rigid registration converges thanks to the coarse alignment computed in Sec. 2.2.2.c. All remaining calculations are done with the aligned meshes $M_{R,\{b,i\}}$.

2.2.4.b Laplacian Surface Edition

The initial non-rigid deformation is computed using Sorkine et al. method called Laplacian Surface Edition presented in [SCOL⁺04]. Based on an intrinsic surface representation, they introduce an approach that can be employed for various mesh editing operations such as free-form deformation, transfer of geometric details between surfaces, and so on. We are interested in this first application. Sorkine et al. argue that for local surface modeling, the surface representation should capture the intrinsic geometry of the surface, rather than the absolute position of points in Euclidean space. Therefore, they use an intrinsic encoding of the vertices, based on differential coordinates. Each vertex is described by the difference between its position and the centroid of its topological neighbors, which is known as Laplacian coordinates. They are a linear function of the global mesh geometry, the conversion between the intrinsic and absolute representations is efficient.

Let $V = \{v_1, \dots, v_n\}$ be the geometric positions of the n vertices in \mathbb{R}^3 . Let N_i designates all topological neighbors of vertex v_i . Then, the Laplacian coordinate of v_i is:

$$L(v_i) = v_i - \frac{1}{|N_i|} \sum_{j \in N_i} v_j \quad (2.2)$$

Modeling operations consist in computing the new coordinates $\{v'_1, \dots, v'_n\}$ of the mesh vertices. It requires to fix the absolute positions of some vertices, such that $v'_i = u_i$ for $i \in \{m, \dots, n\}, m < n$. The constraints $\{u_i\}$ are satisfied in a least square sense. The new geometry V' is solved by minimizing the error function:

$$E(V') = \sum_{i=1}^n \|L(v_i) - L(v'_i)\|^2 + \sum_{i=m}^n \|v'_i - u_i\|^2 \quad (2.3)$$

Observing that Laplacian coordinates are only invariant to translation, the team modifies the latter error function, to make the coordinates additionally independent

to rotation and isotropic scaling. They compute a transformation T_i for each vertex i based on the new configuration of vertices V' . The error function becomes:

$$E(V') = \sum_{i=1}^n \|T_i(V')L(v_i) - L(v'_i)\|^2 + \sum_{i=m}^n \|v'_i - u_i\|^2 \quad (2.4)$$

T_i is a transformation matrix that is limited to represent translations, rotations and isotropic scaling. It is derived for each vertex v_i from the transformation of itself and its neighbors into v'_i and its neighbors.

$$T_i = \min_T \|Tv_i - v'_i\|^2 + \sum_{j \in N_i} \|Tv_j - v'_j\|^2 \quad (2.5)$$

T_i is a linear function in V' . For further details, please refer to [SCOL⁺04].

Mesh edition can be computed through the definition of handles. These handles are define for a set of vertices, which can be moved by the user. Their new positions give the constraints u_i from which the complete smooth deformation of the mesh is computed.

2.2.4.c Non-rigid registration: Laplacian deformation (6)

Following the rigid registration, the second process performed is a smooth deformation of $M_{T,\{b\}}$ towards $M_{R,\{b,i\}}$ for all bones and all individuals. We use the Laplacian Surface Edition method. The deformation uses handles defined for one vertex. They are moved towards target positions, dragging with it the nearby mesh surface in a smooth and detail preserving deformation.

The distance between a point p and a surface S is defined as the shortest Euclidean distance between p and any point of the surface (any point, not necessarily a vertex when the surface is depicted by a mesh).

$$d(p, S) = \inf_{p_S} \|p - p_S\|, \quad p_S \in S \quad (2.6)$$

The non-rigid registration loops over two steps : choosing a handle, then deforming the bone surface. For each vertex of $M_{R,\{b,i\}}$, its distance to $M_{T,\{b\}}$'s surface is computed. The vertex whose distance to the template is the greatest is named v_R . Its closest point on $M_{T,\{b\}}$'s surface is referred to as p_T . The handle is chosen to be p_T , and is moved to v_R 's location, deforming all neighboring region of the template.

The stopping condition is a threshold on the maximal distance between a vertex of $M_{T,\{b\}}$ and its closest point on $M_{R,\{b,i\}}$'s surface. A second condition was fixed on the number of iterations. The definition of the thresholds is discussed in the validation section (Sec. 2.3.3.a). The resulting meshes are referred to as $M_{i,\{b,i\}}$.

Tests have proven that the algorithm requires an initialization, to ensure the quality of the results. Otherwise, falsely close points that are not anatomically correspondent

may cause a bad convergence. The meshes having been previously rigidly registered, one vertex of the template is anchored to its own position, to avoid inopportune translation. Then, a few feature points are identified in both meshes, and aligned with each other. These points are automatically detected, and were defined based on trials. For instance, for the radius, the features chosen were 2 points at the proximal extremity of the radial tube, to ensure that the end of the visible diaphysis were in correspondence. The tip of the radial styloid process was selected to be another feature, as were two points on the distal radioulnar joint, see Fig. 2.6. The identification of such points was based on geometrical criterions, enabled by the coarse pre-alignment of the wrists. All these points are in turn used as handles for a first rough deformation. Then the vertex previously anchored to its own position is unanchored. There was indeed no reason that it was well aligned with the target mesh, and inopportune translations are not a risk anymore when a few other features have been defined.

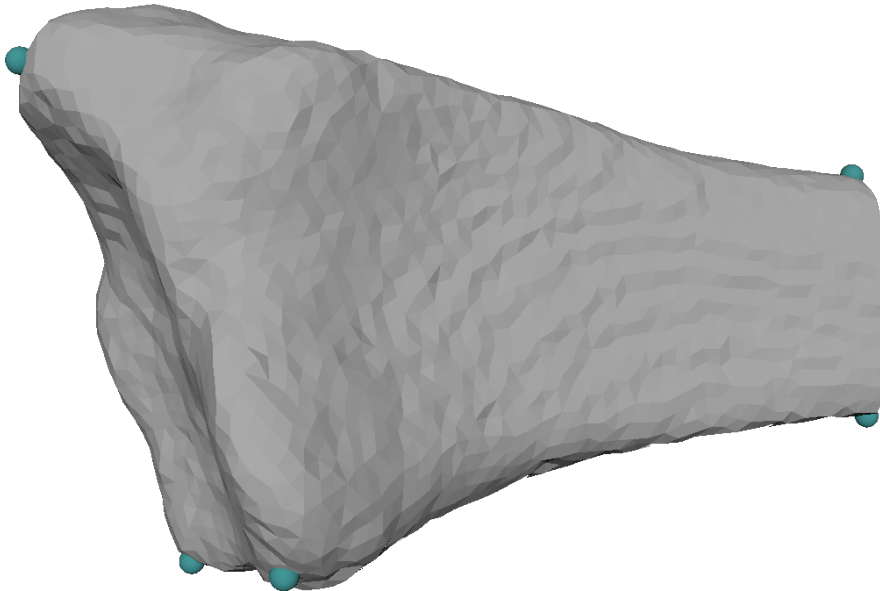


Figure 2.6: Example of the features points used to initialize the radius smooth deformation algorithm.

When all bones $M_{R,\{b,i\}}$ have been approximated by the deformed templates $M_{l,\{b,i\}}$, the templates $M_{T,\{b\}}$ are updated. The new templates vertices are defined as the geometrical mean of the deformed templates instances, the framework remains always the same. The registration of the templates to the database meshes and the update of the templates steps are repeated several times, generating at each repetition a new set of $M_{l,\{b,i\}}$. It is used to reduce the effect of the choice of the initial template meshes. The final meshes are called $M_{L,\{b,i\}}$. The number of iterations is discussed in the validation section Sec. 2.3.3.a.

2.2.4.d Non-rigid registration: projection along the normals (7)

The Laplacian-based deformation is smooth and meets its limits as for capturing the sharp details of the database. Therefore a second registration is used to completely

fit the deformed templates $M_{L,\{b,i\}}$ already similar to the target bones to the database target meshes $M_{R,\{b,i\}}$. The points of the $M_{L,\{b,i\}}$ meshes are simply projected along their normals to the hit point with the subjects bones $M_{R,\{b,i\}}$'s surface. This second registration step guarantees that every vertex is on the surface of the actual bone. The already great similarity between the shapes before this step ensures that the points are already close from their final position, keeping a coherent and regular distribution over the subjects, while best describing their particularities. To completely ensure that a point will not be sent to an absurd location around very sharp details, a maximal distance between the original and the final positions is defined. If the distance to the hit point is higher than this threshold, the point is moved to the mean position of its neighboring vertices.

Projection along normals could be considered as the only non-rigid registration step, and the Laplacian deformation would be skipped. Each point of the deformed template would be on the target's surface, point-to-face distances from the template to the target would be zero. However, depending on the initial shape differences and on the normal orientations, sharp details of the target surface can easily be missed. Additionally crossing normal directions could cause crossing edges, flipped faces, the mesh surface would delineate degenerated volumes. And since the distances are symmetrical, the errors can be very high. For all these reasons, both non-rigid registration step are necessary.

The resulting meshes are the final meshes used in later applications such as statistical models, and are referred to as $M_{W,\{b,i\}}$.

2.2.5 Results

In this section, we have started with a raw database of 3D polygonal meshes, results of manual segmentation and marching cube mesh generation. These meshes presented coarse irregularities that were removed. They also were resampled, in order to have a homogeneous distribution of vertices over its surface. The new resulting meshes are named $M_{D,\{b,i\}}$.

Comparison of 3D shapes requires some relations defined between these shapes. We use dense one-to-one correspondence between the meshes by describing all instances of a class of bones using the same landmarks. Each vertex is considered a landmark, even though it is not necessarily positioned in a significant place of the bones. The bone b of every subject is characterized by the same number of vertices, the j^{th} vertex is at the same location of the bone on all instances. Therefore the correspondence between bones ensues from such a description, all j^{th} vertices are in relation together.

In order to obtain such a characterization of the bones, we have chosen to work with template meshes that are being registered to fit the database bones. The registration is a two-steps process: first the templates are being iteratively non-rigidly deformed towards the target shapes. Secondly, when the templates are close to the targets, their vertices are projected towards the aimed surfaces.

The resulting meshes $M_{W,\{b,i\}}$ are believed to characterize the same shapes as the target ones $M_{R,\{b,i\}}$, while their vertices are used as landmarks for a class of bone and

fitted to represent the same place on each instance surface. The first property is verified in the next section. The second is harder to validate and will be considered in the next chapter. If the properties are verified, shapes diversity can be studied, by comparison of the vertices location, for example using a statistical shape model.

The process stages have aligned and scaled the bones regardless of their initial position in the wrist. However this information is preserved and the meshes can be brought back precisely to their initial location at the end of operations. It is essential for the handling of poses data.

2.3 Numerical Validation

As explained in Sec. 1.4.5, there exist no objective measure to quantify the quality of mesh correspondence. In the absence of a universally accepted metric, we propose to thoroughly validate each step that has led to the final corresponding shapes. We argue that if the error made at every procedures is proven to be bounded, the actual total error, even if cumulative, can only be limited.

The reparameterization of 3D meshes to obtain dense correspondence can be a source of two different types of inaccuracies: (i) the new shape is too divergent from the original one, the object outlined is not faithfully represented anymore; (ii) corresponding vertices are not anatomically equivalent. The first source of errors, similarity of shapes, is investigated in this section. The quality of the corresponding vertices is further explored in the next chapter 3, with respect to specific applications: PCA-based statistical model registration and anatomical landmark identification.

2.3.1 Preprocessing

The preprocessing of the database (Sec. 2.2.2) consists in three operations:

- (1) All artifacts created during the segmentation are manually removed;
- (2) The meshes are resampled in order to guarantee an homogeneous repartition of the vertices;
- (3) A initial alignment of the wrists is computed with the definition of a new system of coordinates based on radius features.

Some data manipulations are more prone to errors. We review each step separately.

2.3.1.a Post-segmentation processing (1)

Some artifacts in the original data were obviously incorrect (Fig. 2.4). Additionnally the metric error of the resampling step (2) took some abnormally high values. These aberrant distances between vertices proved to originate from irregularities in the original data and not from the resampling method. Such irregularities were vertices isolated from their neighbors, or small sets of vertices shaped into an independent mesh inside the bone for example.

The artifacts were removed manually using the software Maya. Manual edition is challenging, no error should be introduced in the data. There exist no groundtruth meshes with which the resulting cleaned up meshes could be compared. We have chosen to limit the task to the elimination of coarse errors. When a set of vertices were in an obviously anatomically incorrect location, these vertices were removed from the mesh. The removal of vertices create holes in the mesh. It was decided that no vertex would be created, but faces between vertices on the edge of the hole would be constructed in order to fill the hole. The resulting meshes $M_{O,\{b,i\}}$ are considered to be the ground-truth shapes of the wrist bones.

2.3.1.b Resampling (2)

The vertices of the meshes $M_{O,\{b,i\}}$ are irregularly spread along the surfaces, which skew distance measures. Therefore, the distribution of vertices was modified to guarantee an homogeneous distribution, based on Centroidal Voronoi Tessalation (Sec. 2.2.2.b).

The resampling was computed using the Graphite software [Lé]. The number of vertices of $M_{D,\{b,i\}}$ was chosen to remain the same as in $M_{O,\{b,i\}}$. The vertex locations and mesh topologies are modified by this process.

This step is the most prone to errors of the preprocessing steps, inaccuracies can be induced in the database meshes: a triangular mesh surface is composed of flat polygons connecting the vertices. Resampling modifies the vertices distribution along the surface, inevitably modifying the polygons and the surface itself. We need to make sure that the changes do not induce too much error. It is especially crucial since these new meshes are later on used as references of the database, they need to be of high quality. We measure both mean and maximum distances between the original and resampled meshes for all data instances. The results are reported in Table 2.1.

In addition to geometrical assessments between the surfaces, we compare the volumes defined by the meshes. We use two coefficients: the Jaccard distance and the Dice coefficient [MDW08, RDD⁺14]. The Jaccard distance measures the dissimilarity between two objects by considering the relation between their intersection and union volumes. Its equation was introduced in (1.4). The Dice coefficient considers the proportion of two times the intersection volume compared to the volume of both objects. It's formula is presented in (1.5). The two coefficients are related, they give an idea of the meshes superposition and similarity. Both are given to ease comparison for future works. The results are presented in Table X.1.

Surface distance between paired $M_{O,\{b,i\}}$ and $M_{D,\{b,i\}}$ meshes are presented in Table 2.1. Each bone is considered separately, the mean (1.1) and Hausdorff distances (1.3) are computed across the individuals I_{CMC} . The mean distance describes the average distance of a vertex to the paired surface. It can be seen that depending on the bones this mean distance for a vertex is in average 0.004 to 0.005 mm and it is at max 0.007 to 0.010 mm. The Hausdorff distance considers the vertex of any of the two surfaces for which the distance to the paired mesh is the greatest. This greatest value is in average in the range [0.088; 0.142] mm. The maximum Hausdorff distances are in the range [0.153; 0.269] mm. It means that the distance between a vertex and the associated surface for any subject and any bone is at max 0.269 mm.

The mean distances between the raw and resampled meshes are very small, a few micrometers only, even for the highest mean values. It shows that the resampling does not change much the global shape of the bones, the new meshes can be used in place of the raw ones without inducing error.

The maximal distance from a vertex to the paired mesh is 0.269 mm at max. The resolution of the acquisition system was $0.33 \times 0.33 \times 0.625$ mm. The resolution of the acquisition system gives a lower bound on the precision of the resulting data, they can never reach a better precision, no matter the treatments. Indeed any information between two slices for instance could be considered as noise, as no acquisition backs the

	Mean dist. (1.1) (mm)			Hausdorff dist. (1.3) (mm)		
	mean	max	std	mean	max	std
Radius	0.004	0.007	0.001	0.139	0.269	0.056
Scaphoid	0.005	0.007	0.001	0.088	0.153	0.021
Lunate	0.005	0.009	0.001	0.091	0.211	0.032
Triquetrum	0.005	0.008	0.001	0.097	0.158	0.025
Pisiform	0.005	0.008	0.001	0.096	0.170	0.027
Trapezoid	0.005	0.007	0.001	0.111	0.249	0.042
Trapezium	0.005	0.008	0.001	0.100	0.186	0.026
Capitate	0.005	0.008	0.001	0.126	0.215	0.035
Hamate	0.005	0.009	0.001	0.123	0.253	0.035
Metac. 1	0.005	0.009	0.001	0.108	0.198	0.037
Metac. 2	0.005	0.008	0.001	0.133	0.259	0.048
Metac. 3	0.005	0.010	0.001	0.142	0.241	0.041
Metac. 4	0.005	0.008	0.001	0.133	0.231	0.031
Metac. 5	0.005	0.008	0.001	0.118	0.266	0.040

Table 2.1: Distances between the initial meshes $M_{O,\{b,i\}}$ and the $M_{D,\{b,i\}}$ meshes, outputs of a first resampling to regularize the vertices and edges distribution on the surface. The results are in mm.

guesses made in between. The maximal distance is below the data acquisition resolution (cf Sec. 1.3.4). Therefore we can conclude that no information is lost in the resampling operation.

The Hausdorff distance is more challenging but in this case it also more interesting. Indeed the mean distance is very small and more or less the same for everyone. Abnormalities can for most meshes only be detected with the Hausdorff distance, as was done in the preprocessing step (1).

In Table X.1, both Dice coefficient and Jaccard distance are given, however since they are related, only the Jaccard distance (1.4) will be discussed. This metric measures the ratio of the two meshes intersection compared to their union. The Jaccard mean distance is in the range $[0.001; 0.003]$, its maximum value lies between $[0.002; 0.005]$. This means that in the very worst case the intersection volume is 995 thousandth as big as the union one. Both volumes are really closed to each other.

In conclusion to both volumetric and surface based metrics, it can be concluded that the resampled data $M_{D,\{b,i\}}$ can be used in place of the original meshes $M_{O,\{b,i\}}$ without loss of information.

2.3.1.c Initial alignment of the wrists (3)

The rough alignment of the wrist procedure does not modify the mesh outlines, it is only used for guaranteeing the ICP algorithm robust convergence. The cut of the

proximal end of the radii shafts (Sec. 2.2.2.c) is later used for template selection. It is a necessary procedure to limit the radius template to a length known for all wrists. Two subjects had such a small length of the diaphysis captured on the scans that they were removed from the database. If the radii meshes are modified, they are not the shapes used as reference of the physical bones. The cut has no influence on the later approximation of the distal end of the radii of the subjects, therefore no validation of this step is required.

2.3.2 Template set creation (4)

The templates are chosen among the database meshes. They are selected for being the most representative instance of a bone across the subjects (Sec. 2.2.3.a).

The measure of distance between pairs of meshes, necessary for shape comparison, requires that they are aligned. Rigid alignment was computed using an implementation of this algorithm in libicp (<http://www.cvlibs.net/software/libicp/>), from Geiger et al. [GLU12]. The scaling was considered to be isotropic. Rigid transformation and isoscaling optimizations were iterated until convergence.

In the resampling step (2) the meshes were resampled in order to have an homogeneous distribution of the vertices on the meshes. In this step of template creation, a second resampling of the meshes $M_{t\{b\}}$ is performed in order to reduce the number of vertices per mesh, but always with an homogeneous distribution. This downsampling is performed using Centroidal Voronoi Tessellation. The criterion retained to set the number of vertices for each bone was that the average edge length should be stable (which is ensured by the resampling step) and of 1 mm. Later tests with stable edges of 0.5 and 0.3 mm have proven that the use of smaller edges enables only very little more precision for a calculation time largely increased. The number of vertices varies for the template mesh of each bone: some bones are bigger than others, they should therefore be represented by more vertices, otherwise there would be variations in the precision of the data. In Table 2.2 are listed every bones and their associated vertices numbers after the downsampling step. By definition they are also the number of vertices of our final meshes.

Bone	sca	lun	trq	pis	tpd	tpm	cap	ham
Nb of vertices	1206	1185	802	708	968	862	1852	1321
	rad	mc1	mc2	mc3	mc4	mc5		
	4261	2760	3843	3471	2595	2322		

Table 2.2: The number of vertices for each template bone $M_{T,\{b\}}$

We verify the similarity between the templates $M_{T,\{b\}}$ and the database bones $M_{R,\{b,i\}}$ that have been affinely aligned to the templates. It is an initial comparison between shapes, intended for later comparisons with the non rigid registration results in order to evaluate the algorithm efficiency. It is therefore not an error but a distance. The templates were constructed starting from subject meshes that were smoothed and downsampled. The templates meshes are therefore expected to have globally the same

shape as the targets but individual details are not expected to be captured by the initial templates. In Table 2.3 are presented the surface measures, each bone is considered separately. Table X.2 presents the volumetric overlaps of the meshes by using both Dice coefficients and Jaccard distance.

The fact that we cut the radii introduces an artifact in the way we compute the distance. A special adjustment is needed when the radii meshes $M_{R,\{\text{RAD},i\}}$ are compared to the template $M_{T,\{\text{RAD}\}}$, a specific distance algorithm must be used. Indeed the database radii meshes $M_{R,\{\text{RAD},i\}}$ have various lengths of diaphysis, while $M_{T,\{\text{RAD}\}}$ was generated from a mesh whose proximal tip was shortened. To ignore the length difference between the bones, the cut plane P of the template is computed. A second plane P_m , parallel to P , but with an offset of one millimeter along the plane's normal in the direction of the radius head is defined. This additional millimeter shift is a safety margin due to some edge effects for a few wrists. Any point on the proximal side of P_m is ignored during the surface distance calculation. The radius template has an opened diaphysis representation. Therefore, the mesh does not delineate close volumes, though it is a necessary condition to calculate the Dice and Jaccard indexes. Both radii volumes of $M_{R,\{\text{RAD},i\}}$ and $M_{T,\{\text{RAD}\}}$ are considered to stop along P_m .

	Mean dist. (1.1) (mm)			Hausdorff dist. (1.3) (mm)		
	mean	max	std	mean	max	std
Radius	0.473	0.886	0.159	2.113	3.634	0.584
Scaphoid	0.357	0.575	0.082	1.649	3.179	0.408
Lunate	0.323	0.819	0.110	1.461	2.758	0.455
Triquetrum	0.333	0.650	0.089	1.467	2.550	0.377
Pisiform	0.282	0.504	0.069	1.168	1.911	0.253
Trapezoid	0.326	0.510	0.074	1.424	2.365	0.312
Trapezium	0.357	0.639	0.088	1.631	2.508	0.386
Capitate	0.376	0.726	0.083	2.081	3.535	0.515
Hamate	0.362	0.585	0.076	1.718	2.959	0.443
Metac. 1	0.378	1.059	0.140	1.726	3.534	0.469
Metac. 2	0.438	0.880	0.132	1.946	3.704	0.446
Metac. 3	0.412	0.748	0.125	1.796	2.744	0.394
Metac. 4	0.381	0.702	0.119	1.678	2.863	0.407
Metac. 5	0.373	0.720	0.107	1.609	2.607	0.361

Table 2.3: Distances between the database meshes $M_{R,\{b,i\}}$ and the templates $M_{T,\{b\}}$. The results are in mm.

The average mean distance from a vertex to the paired surface lies between 0.382 and 0.473 mm, while the maximal value of this mean distance is up to 1.059 mm. The resolution of the acquisition system was $0.33 \times 0.33 \times 0.625$ mm. It means that the average distance is in most cases higher than the initial data acquisition precision in two out of three directions. The average Hausdorff distance for its part is in range [1.168; 2.113] mm. For the carpal bones, it takes maximal values from 1.911 mm for the

pisiform to 3.535 mm for the capitate. This maximal Hausdorff distance goes up to 3.704 mm for the second metacarpal.

These values should be compared to the average carpal bones size presented in Fig. 1.3. For example, the pisiform can in average be delineated in a bounding box of $9.5 \times 11.5 \times 14.7$ mm, while the average capitate bounding box dimensions are $15.0 \times 19.5 \times 26.3$ mm. The distances between surface are indeed very high considering the shapes total sizes, as was expected.

The Jaccard distance, defined in (1.4), indicates dissimilarity between two volumes by measuring the overlaps between the intersection and the union of the two objects. The more the meshes are divergent, badly aligned or variously scaled, the higher the dissimilarity, but always included in range $[0; 1]$. The $M_{R,\{b,i\}}$ meshes have been rigidly registered and scaled to the $M_{T,\{b\}}$ ones, in such a way that only shape divergence remains when the Jaccard distance is computed and presented in Table X.2. The mean distances between the templates and the target meshes are between 0.115 and 0.158. It means that the volume of the intersection between the two meshes is in average only 8.5 to 9 tenth of the union volume. In the worst case, the coefficient reaches 0.324, the intersection volume is only two third of the union volume.

2.3.3 Dense correspondence mapping

Dense correspondence mapping consists in a reparameterization of the database 3D shapes into new meshes describing the same outlines, but with anatomical coherence between the vertices. It was accomplished by deforming templates, first with a smooth Laplacian deformation, then with a sharp projection along the normals. The resulting meshes are expected to match the original shapes, with no loss of details, while vertices are similarly distributed for all subjects.

In the following section, the accuracy of the new shapes compared to the database ones is measured. The meshes output of the Laplacian deformation $M_{L,\{b,i\}}$ are compared to the database ones $M_{R,\{b,i\}}$. We show that the shapes are already very similar to the target ones. It proves that the projection along the normals is simply a detail catching procedure, which does not influence much the overall shape. Then we measure the differences between the final outputs $M_{W,\{b,i\}}$ and the database shapes $M_{R,\{b,i\}}$. We prove that the database is reproduced precisely. The assessment of the anatomical coherence between vertices requires to build a statistical model or other applications, and will be explored in the next chapter 3.

2.3.3.a Non-rigid registration: Laplacian deformation (6)

The affine alignment of the database meshes $M_{D,\{b,i\}}$ towards the templates $M_{T,\{b\}}$ generates the $M_{R,\{b,i\}}$ meshes, whose only surface differences are due to anatomical variations. The templates are non-rigidly registered to the $M_{R,\{b,i\}}$ meshes using Laplacian deformations (Sec. 2.2.4.c).

The registration consists in iteratively moving a vertex of $M_{T,\{b\}}$ to a target position on $M_{R,\{b,i\}}$. The Laplacian deformation drags with the vertex its neighboring surface, in a detail preserving distortion. Vertices are selected and moved successively until a

stopping condition is met. Based on experiments, this condition was chosen to be an arbitrary threshold on the maximal distance between a vertex of $M_{T,\{b\}}$ and its closest point on $M_{R,\{b,i\}}$'s surface. This maximal distance was set to be 1 mm for the biggest bones (radius and metacarpals), and was smaller for the carpal bones, depending on the observed complexity for the template to register to a new instance. Due to the effect of multiple anchors in a neighborhood, the maximal distance does not strictly decrease between iterations, but fluctuates slightly. To counter this effect, the stopping condition was considered met when the maximal distance is below the threshold for 3 iterations in a row. For some bones, it has been observed that the distance converges too slowly, a second stopping condition was defined on the number of iterations. Tests have proven that after 150 iterations, even if the maximal distance was not reached, the two meshes were always satisfyingly close.

The generation of $M_{L,\{b,i\}}$ consists in a repetition of registrations of the templates to the $M_{R,\{b,i\}}$ meshes and updates of the templates. It helps reduce the influence of the initial choice of the template, as explained in the literature. It was indeed observed that even though the stopping conditions are unchanged between the iterations, the mean surface distance between the successive intermediary $M_{l,\{b,i\}}$ and the database meshes $M_{R,\{b,i\}}$ decreases. This is illustrated with the example of the scaphoid carpal bone: the average mean surface distance (1.1) between $M_{l,\{SCA,i\}}$ and $M_{R,\{SCA,i\}}$ for all individuals i of I_{CMC} is given for the 4 first iterations:

Iteration #1:	0.231 mm
Iteration #2:	0.210 mm
Iteration #3:	0.200 mm
Iteration #4:	0.195 mm

The average mean distance decreases over the iterations, though the fifth iteration and the next ones have been observed to improve only very little the global distance, while each iteration is time consuming. Therefore the number of repetition was fixed to 4.

In the same way than the similarity measures between the meshes $M_{T,\{b\}}$ and $M_{R,\{b,i\}}$, the $M_{L,\{RAD,i\}}$ meshes present a shorter proximal shaft than the $M_{R,\{RAD,i\}}$ ones. The same solution was employed than in Sec. 2.3.2: a cut plane P_m is defined and any vertex proximal to that plane is ignored for the surface distances. The volumes of both $M_{L,\{RAD,i\}}$ and $M_{R,\{RAD,i\}}$ are also delimited by the plan.

We present in Table 2.4 the mean and maximal surface distances between the non-rigidly registered templates $M_{L,\{b,i\}}$ and the database ones $M_{R,\{b,i\}}$. The meshes are a result of 4 template update then deformation to fit the target bones. In Table X.3 coefficients of volumes overlap are shown for the same shapes. The adjusted meshes are expected to fit the target meshes well, though they are anticipated to miss some sharp details, since the Laplacian edition is a smooth transformation.

The average distance between a vertex and the surface of the paired shape is included between 0.160 and 0.310 mm depending on the wrist bone. This average distance is smaller than the precision of the initial CT images, which was $0.33 \times 0.33 \times 0.625$ mm. It means that in average there is no error added. However, the maximum distances

	Mean dist. (1.1) (mm)			Hausdorff dist. (1.3) (mm)		
	mean	max	std	mean	max	std
Radius	0.310	0.540	0.077	1.312	2.184	0.322
Scaphoid	0.195	0.280	0.031	0.819	1.522	0.208
Lunate	0.160	0.268	0.029	0.697	1.991	0.229
Triquetrum	0.211	0.315	0.032	0.859	1.106	0.125
Pisiform	0.156	0.203	0.020	0.608	0.761	0.076
Trapezoid	0.190	0.363	0.040	0.782	1.805	0.227
Trapezium	0.280	0.446	0.053	1.170	1.568	0.187
Capitate	0.239	0.299	0.027	1.048	1.609	0.158
Hamate	0.243	0.327	0.035	1.089	1.880	0.226
Metac. 1	0.241	0.343	0.032	0.924	1.272	0.103
Metac. 2	0.244	0.303	0.021	0.933	1.215	0.104
Metac. 3	0.229	0.289	0.022	0.927	1.149	0.084
Metac. 4	0.240	0.301	0.029	0.911	1.089	0.094
Metac. 5	0.222	0.280	0.020	0.875	1.076	0.090

Table 2.4: Distances between the database meshes $M_{R,\{b,i\}}$ and templates non-rigidly registered using Laplacian deformations $M_{L,\{b,i\}}$. The results are in mm.

between a point and its closest face are in average in range $[0.608; 1.312]$ mm. The highest maximums are even as high as 0.761 to 2.184 mm.

The mean distance between surfaces is correct considering the original precision of the data. However the extreme distances are high, up to 2 mm. It means that as expected the global shapes of the bones are properly modeled. However sharp details are missed by this method. Yet, these details might be of importance and should be captured too. It may also be noted that the maximal Hausdorff distances and even some mean Hausdorff values are higher than the threshold fixed for the stopping condition. This is due both to the limit on the number of iterations, and to the fact that the threshold was fixed on the distance between a vertex of $M_{L,\{b,i\}}$ to the paired surface while the Hausdorff distance in Table 2.4 is symmetrical.

The Jaccard distance defined in (1.4) takes in average its values in range $[0.070; 0.0117]$, depending on the bone. It indicates that the intersection between the database mesh and the deformed template is in mean nine tenth of the union volume. The distance can however go as high as 0.178, that is the intersection represents only eight tenth of the volume.

The results can be compared with the ones obtained between the affine aligned database meshes $M_{R,\{b,i\}}$ to the original templates $M_{T,\{b\}}$ (Table 2.3, Table X.2). They are strictly better, whether considering means or maxes of all bones. The mean distance between a vertex and the paired surface drops below the original data precision for all bones in average, and even so for the highest mean distance for most of the bones.

2.3.3.b Non-rigid registration: projection along the normals (7)

According to the results after Laplacian deformation, the deformed templates are very closed to the target shapes. However, they miss some details, which is underlined by the high maximal distances. This was expected, considering that the deformation is a smooth transformation, while the bones may present sharp details. To refine the results a last non-rigid deformation is performed on the registered templates: a projection along the normals of the vertices towards the target mesh surface (Sec. 2.2.4.d). The shapes need to be very similar to ensure that two crossing normals will not cause some flipped faces for instance. It is the case, as verified in Table 2.4, Table X.3.

The surface distances comparing the final deformed meshes $M_{W,\{b,i\}}$ and the target meshes $M_{R,\{b,i\}}$ are presented in Table 2.5. The volumetric overlap coefficients are introduced in Table X.4. As for the comparison between database meshes and deformed templates, the tip of the radii shafts is ignored.

	Mean dist. (1.1) (mm)			Hausdorff dist. (1.3) (mm)		
	mean	max	std	mean	max	std
Radius	0.053	0.100	0.027	0.480	0.768	0.111
Scaphoid	0.040	0.059	0.007	0.391	0.592	0.073
Lunate	0.040	0.077	0.010	0.415	0.775	0.121
Triquetrum	0.052	0.073	0.009	0.483	0.783	0.124
Pisiform	0.045	0.066	0.008	0.375	0.739	0.100
Trapezoid	0.050	0.092	0.012	0.475	0.778	0.123
Trapezium	0.058	0.087	0.013	0.494	0.678	0.097
Capitate	0.043	0.057	0.006	0.532	0.787	0.118
Hamate	0.045	0.077	0.009	0.480	0.640	0.078
Metac. 1	0.037	0.056	0.008	0.474	0.782	0.093
Metac. 2	0.041	0.060	0.009	0.532	0.817	0.109
Metac. 3	0.041	0.062	0.008	0.565	0.799	0.097
Metac. 4	0.043	0.062	0.007	0.541	0.762	0.110
Metac. 5	0.041	0.060	0.009	0.445	0.687	0.099

Table 2.5: Distances between the database meshes $M_{R,\{b,i\}}$ and the templates $M_{W,\{b,i\}}$ non-rigidly registered using Laplacian deformations followed by a projection along the normals. The results are in mm.

In Table 2.5, both mean and Hausdorff average, max and standard deviation values are presented. Starting with the mean surface distance defined in (1.1), it can be observed that the average distance is included in range $[0.037; 0.058]$ mm. It is largely below the original acquisition precision, which was $0.33 \times 0.33 \times 0.625$. The maximal values of the mean distance have an upper limit of 0.100 mm, which is similarly way below the original precision. The Hausdorff distance for its part is in average included between 0.375 and 0.565 mm. These values are higher than the size of a pixel in the CT images, but are smaller than the space between two planar images. Finally the maximal distance between a point and its closest neighbor on the other surface is included in $[0.592; 0.817]$

mm. These values are higher than the precision of acquisition. However, they are the maximal values of the Hausdorff distance, which means that only one or a few points for one or a few subjects reaches these distances. The error made remains below the millimeter. These values should be compared with the average carpal bones sizes presented in 1.3.

In Table X.4, the volumetric overlap between the target and deformed meshes is presented. The two distances being related, we will only discuss the Jaccard distance, which volumetric implications are easier to apprehend. The mean values of the Jaccard distance, measuring dissimilarity between volumes is included in range [0.013; 0.025]. It means that the intersection volume of the two bones is in average approximately 98% of the union volume. The worst distances being between 0.019 and 0.040, the ration between the intersection and union volumes is at worst 96%.

Both surface and volumetric measures indicate that the projection along the normals step significantly improves the results. All distances, whether in average or in max are greatly reduced. In addition to being better, the results are good. They prove that the meshes are very similar. No shape information is lost when the deformed templates are being used instead of the original ones.

To further illustrate the similarity between meshes, various shapes, both from the database and registered ones are overlaid in two representations. It can be observed on these figures that the bones are very similar. In Fig. 2.7, the meshes are seen as wireframes: the edges are represented, but not the faces. The similarity between the bones is mostly visible around the bones edges. On the second illustration, in Fig. 2.8, all carpal bones, the radius and the metacarpals of two wrists are visible. The faces are colored, in green for the target mesh $M_{R,\{b,i\}}$, in pink for the registered templates $M_{W,\{b,i\}}$. The way both colors alternate on small surface illustrates how the surfaces are really close. It can also be observed that the final radii meshes in pink are shorter than their equivalent target meshes. Indeed, the radius diaphysis of the mesh used as radius template was shortened.

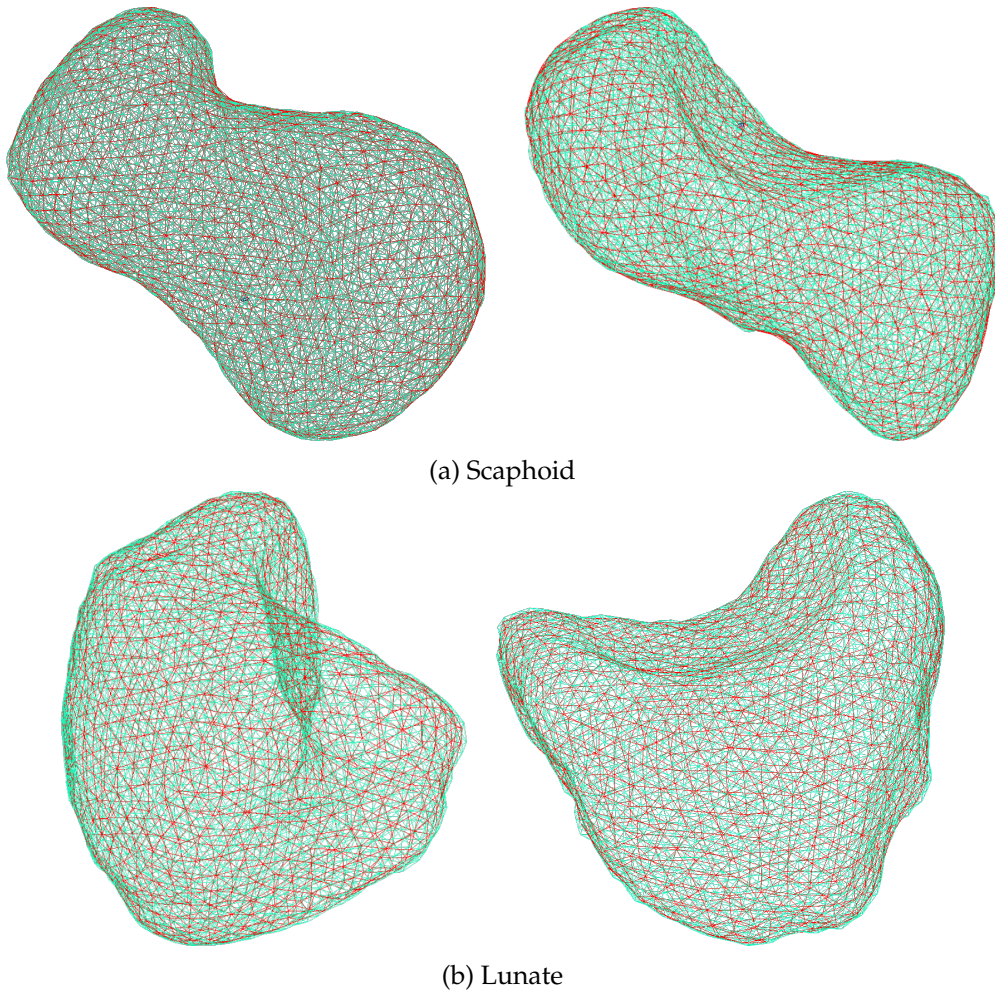
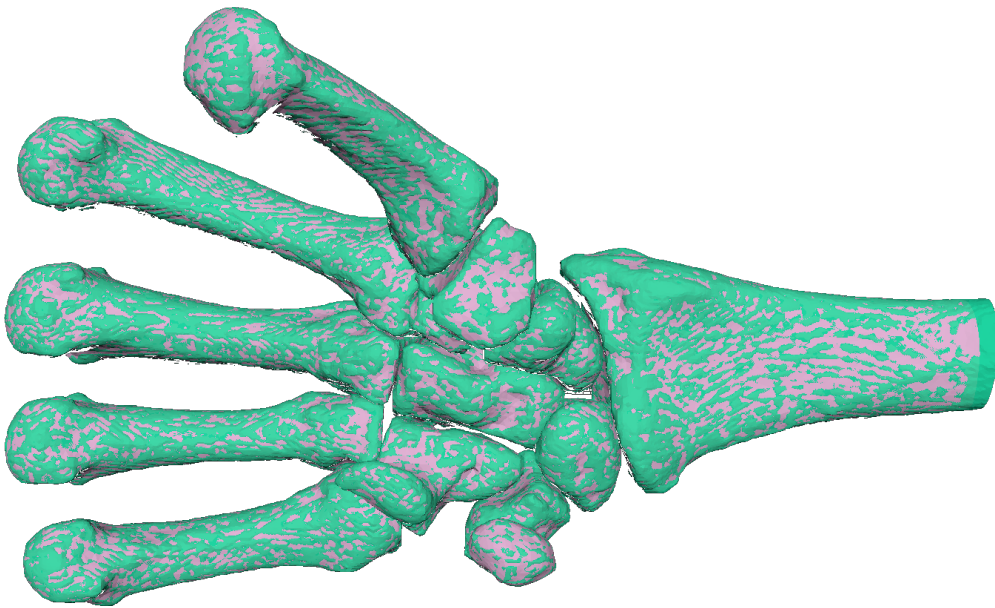


Figure 2.7: Two overlays of a database mesh $M_{R,\{b,i\}}$ in green and its registered template $M_{W,\{b,i\}}$ in red, in wireframe view. Both pairs were taken at two different angles.

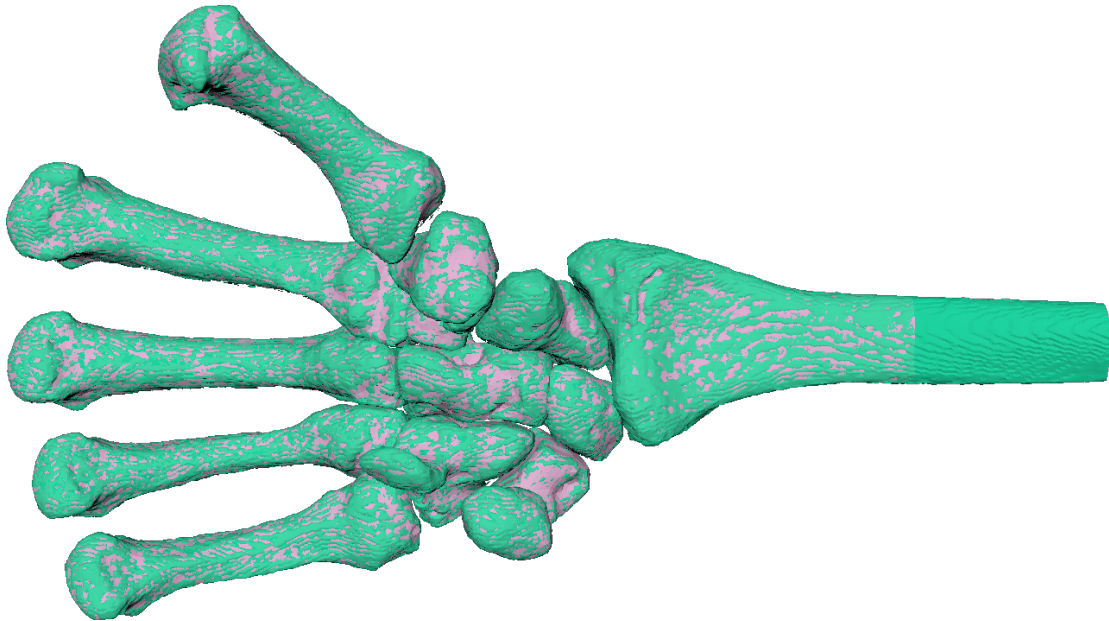
2.4 Conclusion

In this chapter, we have introduced a method to define correspondence between the small complex shapes that are the carpal bones. We paid particular attention to propose an algorithm that can be easily implemented, that is reproducible and we provide upper bounds of errors with different metrics. We endeavor to prove that our resulting meshes are reliable, they encode the exact same shapes as the original meshes.

Compared to the previous approach [JLBC16], we favor a method that give more freedom. It enables manual intervention should the need arise, as we have experienced with our dataset. We chose to work with templates non-rigidly registered to the database bones. These templates are iteratively updated, becoming the geometrical mean of all their deformed instances, before being registered again. These updates avoid too much dependence of the results on the original chosen templates. Finally, we have added a projection along the normals of the vertices to the target surface to refine the results.



(a) Person 1



(b) Person 2

Figure 2.8: Two database wrists and their registered meshes as colored surfaces. In green are the database target bones while the registered templates are colored pink.

Considering the quality measures of the meshes, we prove that both Laplacian deformation step and projection along the normals step are necessary and useful. The distances strictly improve after both processes, while the initial templates and the database bones are too different for a direct projection along the normals, vertices would be badly distributed along the target surface.

The final results prove that the difference between the initial shapes and the ones in correspondences are small. They are however existent. This is normal, since the templates have from 6 to 8 times less vertices than the original shapes. Nonetheless we obtained surfaces that provide an accurate representation of the bones, with mean errors largely below the accuracy of the CT images ($0.33 \times 0.33 \times 0.625$ mm). In addition, if really obvious coarse errors have been manually deleted during the preprocessing of the data, some defects remain present in the database bones, such as step-like appearance of the surfaces. We can therefore argue that on the opposite of being a negative point, the small remaining distance between the meshes smooths out such artifacts.

We have proven so far that the shapes encoded in both database and registered templates are similar. However, we argue that in addition to simplifying the meshes by describing them with fewer points, we also obtain meshes that are in dense correspondence. This has not been studied yet, and will be considered in the next chapter.

CHAP. 3

APPLICATIONS USING DENSE CORRESPONDENCE PROPERTIES

Contents

3.1	Introduction	78
3.2	Statistical Shape Model	79
3.2.1	State of the art	79
3.2.2	Principal Component Analysis	81
3.2.2.a	What is Principal Component Analysis?	81
3.2.2.b	Application and validation	84
3.2.3	Gaussian Processes	92
3.2.3.a	What are Gaussian Processes Morphable Models (GPMM)	93
3.2.3.b	Applications	98
3.2.4	Discussion	101
3.3	NIH reparameterization	103
3.3.1	Dense correspondence mapping of the NIH using the SSMs	103
3.3.2	Numerical Validation	105
3.3.3	Discussion	109
3.4	Anatomical Joint Coordinate Systems	111
3.4.1	State of the art	111
3.4.2	Coordinate System Computation	113
3.4.3	Comparison with Halilaj's results	114
3.4.4	Discussion	115
3.5	Conclusion	117

3.1 Introduction

In the previous chapter, a method to reparameterize shapes into meshes in correspondence was presented. The output meshes of a class of shapes are such that they are all described by the same number of vertices, and each vertex is on the same anatomical location for all instances of the class. The method was applied on a database of wrist bones, the output meshes are noted $M_{W,\{b,i\}}$, with b characterizing the class of bone the shape belongs to, i is the index of the person in the database.

In this chapter, we propose various applications of such a database, composed of bones in correspondence. The first application is the computation of statistical shape models. They consist in a statistical analysis of the location or deformation of the mesh vertices over the instances, and can only be computed when the shapes are in correspondence. Most of the time, the modeling is based on a Principal Component Analysis of the forms, or derivative methods. We compute such a model, both as a reference and because the correspondence quality factors proposed in [DCT01] rest on a Statistical Shape Model (SSM) computation. In a second time we compute a Gaussian Process based model. The latter is less common and has never been used on wrist bones, but offers advantages over SSMs, such as non-linearity and adaptation to posterior information. We carefully test the models in order to verify their reliability.

In a second phase, we use the SSMs to register a second wrist database. It offers two advantages: the model can be further tested on new data and the modeling of this other database with the SSMs is naturally in correspondence with the bones of the training database. We prove that the resulting shapes are close to the original ones: the average Hausdorff distance is below 0.3 mm. The method presented in Chap 2 is not used on this database because the final purpose of the work is to create tools for registration applications, and evaluation of the model on unknown data is more interesting. Furthermore the data of this second database are less complete than the one used in the previous chapter, the metacarpals are only partially visible, the radii distal end are shorter. Using complete models on these data bring information about the unavailable parts of the bones.

Finally, we propose a third application for the meshes in correspondence. We prove that the properties of these meshes allow the definition of consistent system of coordinates on example instances. The latter can be reproduced on all other occurrences of the database. Such systems are employed in biomechanics, the study of a joint movement is based on the rigid transformations of one system relatively to the other. We prove that the method is as reliable as another specific one proposed in the literature while being more global. The results additionally strengthen the confidence in the correspondence relations quality between the meshes, as the method is entirely based on the correspondence features.

3.2 Statistical Shape Model

In a first step, we propose to use the correspondence relation between the database meshes to construct statistical shape models. These latter are a common application for meshes in correspondence. They enable the analysis of shapes distribution by describing the main variations among a class. They can be used for various operations: for example the characterization of the main shape variations among a population allows a better understanding of the shapes studied. The statistical models are also often used as prior knowledge for image segmentation, which allows more stable and precise results. They can also be used to retrieve 3D information from 2D images using the additional knowledge of the model.

In all of these applications, the accuracy of the model is critical. We endeavor to create statistical models that should be convenient and reliable and measure their limits. They can afterwards be used for any aforementioned application, once their expected accuracy is established. We especially propose to work with Gaussian Process Morphable Models (GPMs), an extension of PCA-based SSMs, that have been little used by now. In particular, to the best of our knowledge, they have never been used for wrist bones encoding. The additional computation of PCA-based SSMs have two purposes: it enables comparison with GPMs and it is required for the computation of correspondence quality criteria.

The section starts with a brief state-of-the-art of existing statistical shape models. Then PCA-based SSMs are computed and analyzed, both models describing individual bones and a model characterizing the whole wrist at once. Then a more complex statistical model is used, based on Gaussian Processes, and the practicality of such a model for our data is discussed.

3.2.1 State of the art

One challenge in computer science is to make the machines able to recognize and delineate objects in pictures. Yet, objects can appear very different depending on the camera angle, or due to differences of shapes between instances. It is especially the case in medical imaging, every subject's organs are uniquely shaped, and they evolve over time, whether fast, such as beating hearts or more slowly. The need to adapt an initial object to the shape of the considered instance has risen.

Different solutions were proposed over time to segment variously shaped instances of the same class of objects. Model-based segmentation is a top-down approach consisting in matching a model containing information about the class expected shape with new images. It is one of the most successful existing methods, the prior information brought by the model provides stability against image artifacts and perturbations [HM09]. The flexibility of the model enables adaptation to the various instances of the class. We focus on this segmentation approach.

One of the first flexible model was introduced by Kass et al. [KWT88] and is called Active Contour Models or Snakes. It consists in describing the contour of an object as a continuous spline subjected to forces controlling compliance to image features and fulfillment of structural constraints such as smoothness. However, snakes lack

specificity as they don't incorporate knowledge about shape variations in the class and are not restrained in their distortions as long as the energies are minimized [DTT08].

Information about common variations need to be added in the model. One straightforward approach consists in considering multiple instances of the object class as training shapes and learning from the set statistical properties of the class [HM09]. It leads to Statistical Shape Models (SSMs), most of them being based on a Principal Component Analysis (PCA), which is further detailed in Sec. 3.2.2. The first SSM was introduced by Cootes et al. in [CHTH94] and was more detailed later in [CTCG95]. The statistical analysis of the training set is computed using PCA: they work with shapes described by landmarks, and analyze the points positions distribution over instances. This distribution is called Point Distribution Model (PDM). The model based on the PDM used for image segmentation is named Active Shape Model. Another popular SSM was introduced by Blanz and Vetter, called the Morphable Model. It is used for generation of new human faces and extraction of a 3D mask from a 2D picture, also based on PCA [BV⁺99].

PCA-based models are linear, which makes them mathematically easy and fast to compute. They can only represent linear combinations of the training shapes, which makes them robust towards artifacts and noise [LGJV17]. However this limitation to the linear span defined by the training set is both an advantage and a downside of the method. It prevents the apparition of impossible shapes, but it also prevents the model from generating accurate shapes too different from the training set. To overcome this problem, the training data should be as numerous and various as possible.

For PCA-based models, the training set should ideally be very large, however this is often not possible, in particular when working with medical images. Therefore, works have been conducted to reduce the impact of limited quantity of data for the model creation. Artificial training data can be used, as in [CT95]. Cootes et al propose to add artificial training data using finite element models (FEM). These latter give a set of linear deformations of one shape corresponding to its modes of vibration. They generate many new shapes using FEM on every instance of the training set, and use all original and generated shapes to train the SSM. However, the variations of the FEMs are arbitrary and may not be representatives of the real variations of the class of shapes. In order to extend the flexibility of the model, a spatial partition of the object can also be a solution, as proposed by Zhao et al in [ZAT05]. They partition shapes in tiles, and apply a PCA to each tile separately, before projecting the results in one hyperspace to ensure coherence between the fragments. Blanz and Vetter [BV⁺99] propose a similar partitioning of the total shape in sub-regions, which were morphed individually before being blended back together. Finally, another solution consists in decomposing the shapes in the frequency domain as proposed by Davatzikos et al [DTS03], and later improved by Nain et al. [NHBT07]. The hierarchical multi-scale formulation of SSMs is based on a wavelet transform of the points positions.

Wang and Staib chose to improve the SSM by working on the covariance matrix, rather than on the data [WS00]. They introduce the covariance matrix based on the PDM of the training data, but they also propose a covariance matrix describing smoothness constraint between neighboring points. Finally they combine both matrices to associate

the specificity brought by the model trained on the data with the variability of the smoothness constraint. Lüthi et al propose in a series of articles summarized in [LGJV17] a similar idea of SSM but extended. Their model is based on Gaussian Processes and is further detailed in Sec. 3.2.3. They call it Gaussian Process Morphable Model (GPMM). The GPMM can be viewed as an extension of the PCA-based SSM, in that it is more complete. Gaussian Processes were already used in the 90's for image registration, as referred in the overview by Grenander et al. [GM98]. Lüthi et al. argue that in their version using the Nyström approximation any combination of kernels can be used, which makes the method so powerful.

In this state of the art, we have focused on models for shapes characterized by landmarks distributed over the object, and already in dense correspondence. It is indeed the type of data we're working with (cf chapter 2). However, different shape characterizations, such as skeletons representations, surface encoding with Spherical Harmonics or Fourier surfaces lead to diverse models.

In the following sections, two statistical models have been implemented: a PCA-based Statistical Shape Model and a model based on Gaussian Processes. The theory behind the models, as well as the results achieved are presented and discussed.

3.2.2 Principal Component Analysis

The Principal Component Analysis, also called PCA, is a statistical procedure used to extract the principal modes of variations of data. It can also be used for dimensionality reduction of data, as will be further explained. It has been widely used for image segmentation, the PCA being used as prior information about the object class shape in the form of a Statistical Shape Model. It can have other applications, such as shape analysis by examination of the main modes of variations or investigation of the impact of some factors such as gender. Finally, as previously mentioned in Chapter 2, the SSM is a mean of measuring correspondence quality.

We chose to apply PCA on our data. It is aimed at controlling the quality of the correspondence results previously computed. It is also meant for comparison with the Gaussian Process Morphable Model later computed. First we detail the PCA procedure (further details can be found in Jolliffe's work, for instance in [Jol11]). Then we explain and examine our results.

The procedure requires multiple properties of the data: the data must follow a Gaussian distribution. In the case of coordinates of landmarks, the shapes must be previously similarly aligned, oriented and scaled, to avoid noise. We make the assumption that the bone shapes indeed follow a Gaussian distribution, which is a classical hypothesis. As explained in Chapter 2, all bones were previously aligned and scaled using ICP, this condition is met.

3.2.2.a What is Principal Component Analysis?

The Principal Component Analysis is a statistical procedure that evaluates the distribution of a set of data, and transforms them to a new space of uncorrelated components, which often leads to a dimensionality reduction.

Let us suppose we have n measurements of a vector \mathbf{x} of p random variables. These variables are potentially correlated. PCA transforms the data to a new space of uncorrelated variables. The axes of this new space are a set of orthogonal vectors, the origin of the coordinate system is the projection of the mean shape $\bar{\mathbf{x}}$ in the new space. PCA determines a set of orthogonal axes, which maximizes the variance along each axis. These axes are determined in such a way that they successively have maximum variance for the data, while being uncorrelated with previously computed axes. The number of distinct non-zero vectors is $q = \min(n - 1, p)$, which often leads to a reduction of dimensionality. An example of principal components can be seen in Fig. 3.1.

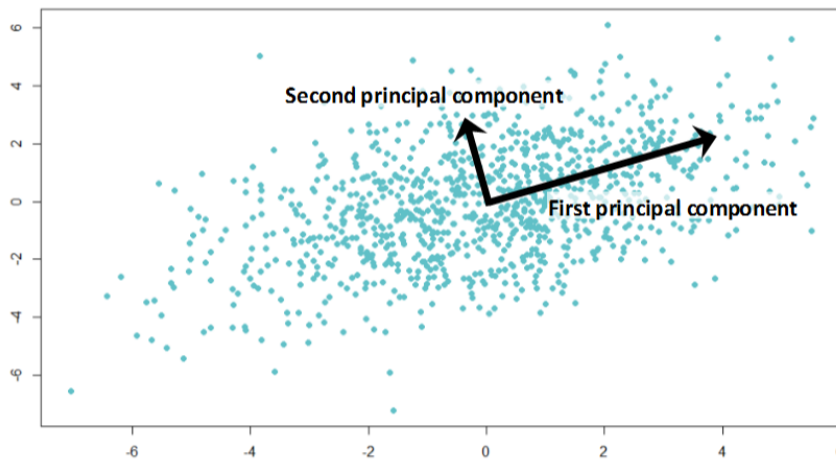


Figure 3.1: Example of a Principal Component Analysis. The first component is the axis on which there is the most variability when the data are projected onto it. The second axis is perpendicular to the first one. The center of the new system is the center of mass of the data.

It can be proven that the orthonormal directions that maximize the variance associated to each vector are given by the eigenvectors of the data covariance matrix, corresponding to the q largest eigenvalues [DTT08]. The eigenvalues give the variances associated to each eigenvector, the latter are ordered from the highest eigenvalue to the smallest one. To avoid the domination of a few high-variance variables over the others or in the case of different units, the variables are often standardized to have zero mean and unit variance [Jol11].

The PCA is computed as follows. At first the mean shape is calculated, as a simple average over the n measurements.

$$\bar{\mathbf{x}} = \frac{1}{n} \sum_{i=1}^n \mathbf{x}_i \quad (3.1)$$

Let \mathbf{X} be the matrix ($n \times p$) composed of all measurements of vector \mathbf{x} , and \mathbf{X}_c the standardized matrix such that:

$$\mathbf{X}_c(i, j) = \frac{\mathbf{X}(i, j) - \bar{\mathbf{x}}(j)}{\sigma(\mathbf{X}(:, j))} \quad (3.2)$$

$\sigma(\mathbf{X}(:, j))$ is the standard deviation of the j^{th} variable of all measurements of \mathbf{x} . The covariance matrix C is computed, using standardized values.

$$C = \frac{1}{n-1} \mathbf{X}_c^t \mathbf{X}_c \quad (3.3)$$

Then, the eigenvectors matrix V and their associated eigenvalues Λ are defined such as:

$$CV = \Lambda V \quad (3.4)$$

Only the q non-zero eigenvalues and their associated eigenvectors are considered. The matrix V maps the data from the original space towards the new space. A measurement of \mathbf{x} expressed in the new base, called x_n , is equal to:

$$x_n = (\mathbf{x} - \bar{\mathbf{x}})V\sqrt{\Lambda^{-1}} \quad (3.5)$$

New measurements of \mathbf{x} can be simulated by generating random vectors w of size q , with each value $w_i \sim \mathcal{N}(0, 1)$. Usually the values are forced to take their value in the interval $[-3; 3]$.¹ The vector of size q is the representation of the simulated measurement in the new space. In the original space, the simulated measurement is equal to:

$$\mathbf{x}_w = \bar{\mathbf{x}} + wV^t\sqrt{\Lambda} \quad (3.6)$$

It should be noted that the mapping are not exactly the inverse transformations of each other, even if all non-zero eigenvectors are retained, since the dimensionality of parameter space is less than the dimensionality of shape space [DTT08]. If a new observation of \mathbf{x} is projected into the new space, then transformed back into the original space, it will not be strictly identical to the initial observation. Indeed the first transformation is a projection into the subspace defined by the training set, then it is transformed back through a linear interpolation of the training set measurements, using the available modes.

¹Let X be a random variable, with a normal distribution of mean μ and standard deviation σ . Let x be a value taken by X . Then $P(x \in [\mu - 3\sigma; \mu + 3\sigma]) \geq 99.7\%$. Which means that almost all values that can be taken by X will be in the interval $[\mu - 3\sigma; \mu + 3\sigma]$ with a very small chance of error.

We make the assumption that the distribution of \mathbf{x} is a multidimensional normal distribution. The eigenvalues associated to the eigenvectors represent the variance of the modes. The square root of an eigenvalue gives the standard deviations of the mode sd . Then with a similar reasoning than in one dimension, with a very small error, we can define the range of all possible shapes as all those that can be described as a summation of the mean vector and the weighted eigenvectors, each weight w_i being such as $w_i \in [-3; +3]$

Most often the last eigenvectors are associated with small variance, information added by these vectors is poor. When there are not many data, it can even be strongly linked to one of the measurement, and falsely add variance to the model, which can worsen the results. Therefore, the last eigenvectors are often ignored, and only the ones corresponding to large eigenvalues are considered. The number of eigenvectors kept can be chosen according to multiple criteria: the cumulative variance should be higher than a defined proportion of the total shape variance, for instance 95% or 99%. Or else the number of eigenvectors kept should enable to reach a certain accuracy of data when using the model. In this case, the number q of considered eigenvectors is smaller than the number of non-zeros eigenvalues. The equations are still true, V and Λ are simply replaced by their truncated versions.

The registration of a SSM to a target shape consists in minimizing the distance between the target mesh x_{target} and the deformed model \mathbf{x}_w . The optimization is computed over the vector w , which describes the weight associated to each mode. We use the mean distance d_{mean} defined in (1.1) as the reference distance between meshes to be minimized.

A statistical model of 3D shapes is constructed by using the position of the meshes vertices. A mesh is described by p vertices in the 3D space. All coordinates are appended in a vector of size $3p$. The shapes are gathered in a matrix of size $(n \times 3p)$, with n the number of available shapes. This matrix of data \mathbf{X} is the one used for the PCA computation. The model describes the vertices location, a shape is recreated from the positions using the same edges and faces as in the training set. In the following section, such a model has been computed on our data, the results are presented.

3.2.2.b Application and validation

As a result of the processes applied in Chapter 2, our bones are described by 3D meshes that have been aligned, rotated and scaled in such a way that only shape differences are the cause of variations among the bones. The meshes are in dense correspondence and we make the assumption that the distribution of the bone shapes is a multidimensional normal distribution. All conditions necessary for PCA computation are met, we present a statistical model of our data.

Models computation

We chose to calculate two different types of PCA: one per bone and one for the whole wrist including the 14 bones. Both models are interesting as they bring various information. A model for one bone includes less information, and can therefore be more specific and will better capture the details of the bones. Registration results will be more precise. However, if the model of the whole wrist will be less detailed, it has the benefit of considering neighboring bones altogether. The carpal bones are small and really close to each other, the shape of one necessarily influences its neighbors, the complete model takes it into account. It enables the study of how bone shapes affect each other. This hasn't been studied yet, to the best of our knowledge.

The two main modes of variation of the whole wrist model are shown in Fig. 3.2. The most important variation of shape for the wrist bones is the length and thickness of the metacarpals. In the database they evolve between long and thin to shorter and thicker. It can be noted that quite logically the five of them evolve in the same way, they are all either long or short. The second most important mode of shape variation in the wrist is more subtle to observe on the illustration of Fig. 3.2. The radius styloid form evolves, being either further forward or backward. In the same time the extremities of the metacarpals change from being flatter and in the continuity of the bone to being more brought out. The lunate for its part present a concavity or not. The analysis of the modes of variation is interesting for a better understanding of the different types of wrists existing, and for later classification of new wrists for instance. Such analysis of the main modes of variations have been conducted for carpal bones, the bones were considered separately [vdGFS+10].

When a SSM is computed, one of the parametrization decision to make is the number of eigenvectors that should be used. When the number of data is small, the eigenvectors associated with small variance are sometimes too specific and should be associated rather with noise than with valuable information. To determine the number of eigenvectors that should be used, the models were used to approximate new shapes. The evolution of the registration accuracy compared to the number of modes used was analyzed. The new shapes outside the training set needed for such an application were obtained with a leave-one-out method: every subject of the database was by turn left out of the training shapes and the model was registered to it. Both individual models and the whole wrist one number of modes were investigated this way.

Registration of the models to the subjects

The maximum number of modes available for a model is the minimum value between the number of measurements minus one and the dimensionality of one measurement. In our case the number of subjects is the limiting factor, 43 of them were complete wrists, making 41 the maximum number of non-zero eigenvectors for the models when a subject is left out of the training set. Therefore the models were by turn registered to the target individual using 5, 10, 15, 20, 25, 30, 35, 37, 38, 39, 40, 41 modes. The evolution of the distance between the target mesh and the registered models were computed, using both mean distance (1.1) and Hausdorff distance (1.3) between meshes. The results of the individual models are shown in Fig. 3.3 for the mean distance, in Fig. 3.4 for the Hausdorff distance. The results of the complete model are similarly shown in Fig. 3.5 for the mean distance and in Fig. 3.6 for the Hausdorff distance. It must be noted that if all bones are considered at once in the model, the distances are nonetheless measured for every bone separately.

Considering the individual models, one per bone, it can be noted that the registration gets strictly better when the number of modes used gets higher. No maximal value has been reached where additional modes are unhelpful due to noisy information. This is true for all bones and both mean and maximal distances. The curves presented in Fig. 3.3 and Fig. 3.4 are strictly decreasing. We can note that the mean distance between the target mesh and the registered model is strictly smaller than 0.3 mm for all bones when enough eigenvectors are considered in the model. The mean error made between

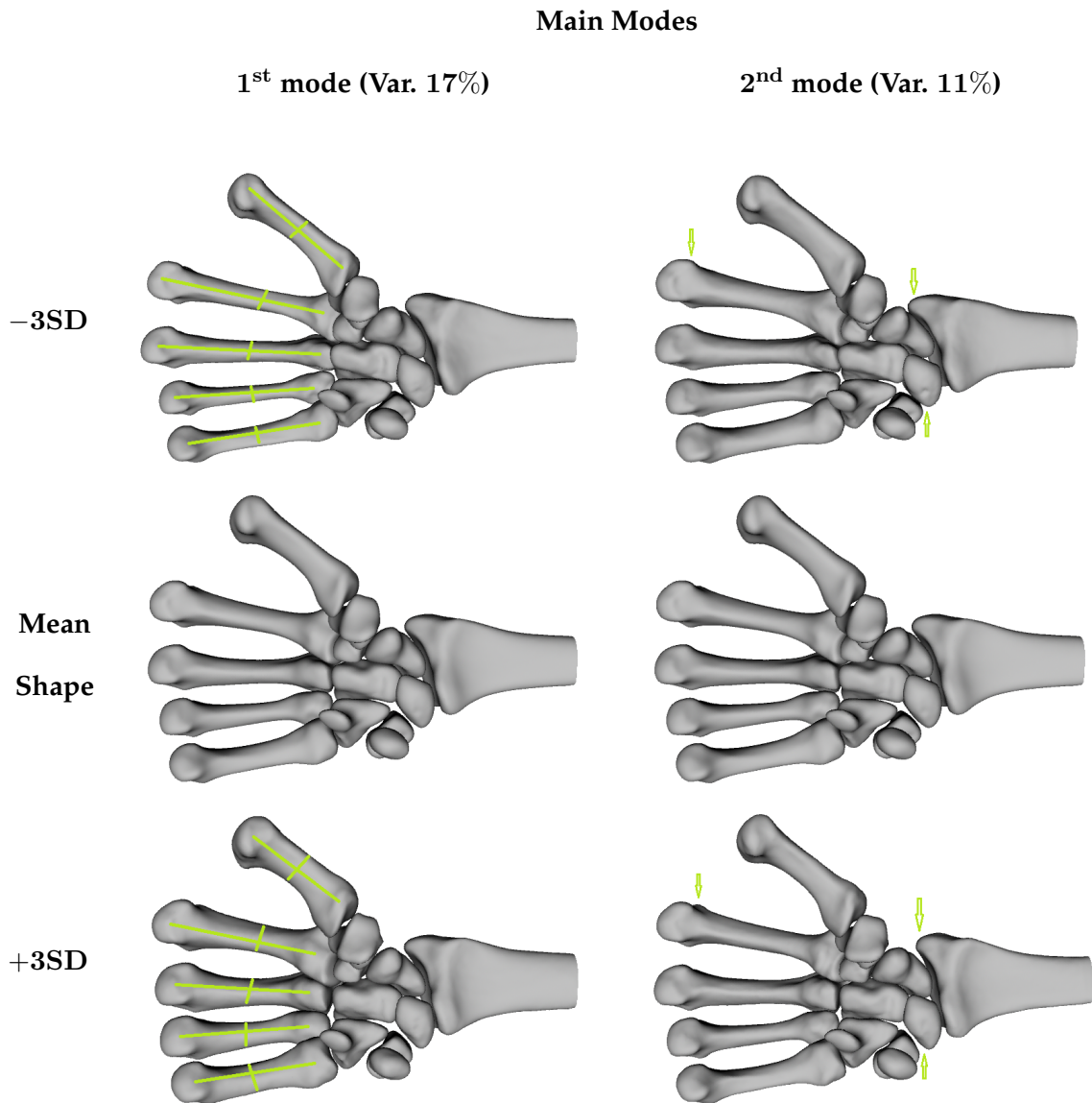


Figure 3.2: The two principal modes of variation of the SSM including the 14 wrist bones. In the middle is shown the mean shape of the wrist bones, while above and under are illustrated the effects of the two principal modes of variation, at extreme values. In the left column is shown the most important mode, in the right the second most important one. The two modes are associated with respective variances of 17% and 11% of the total model variance.

a vertex and its closest point on the paired surface is smaller than the accuracy of the initial data ($0.33 \times 0.33 \times 0.625$ mm). The Hausdorff distance between the target and the model lies between 0.7 mm and 1.6 mm. The smallest difference is for the pisiform, which is the smallest carpal bones, with both the less complex shape of all and the smallest number of points to represent it (see Table 2.2), enabling more details to be captured by the model. The highest difference is between the radius model and its target. This is due to the fact that it is the biggest bone, with the most vertices. Moreover the opened end of the radial styloid is an additional difficulty, that in spite of being taken into account in the distance measurement, has nonetheless a bad impact on the results.

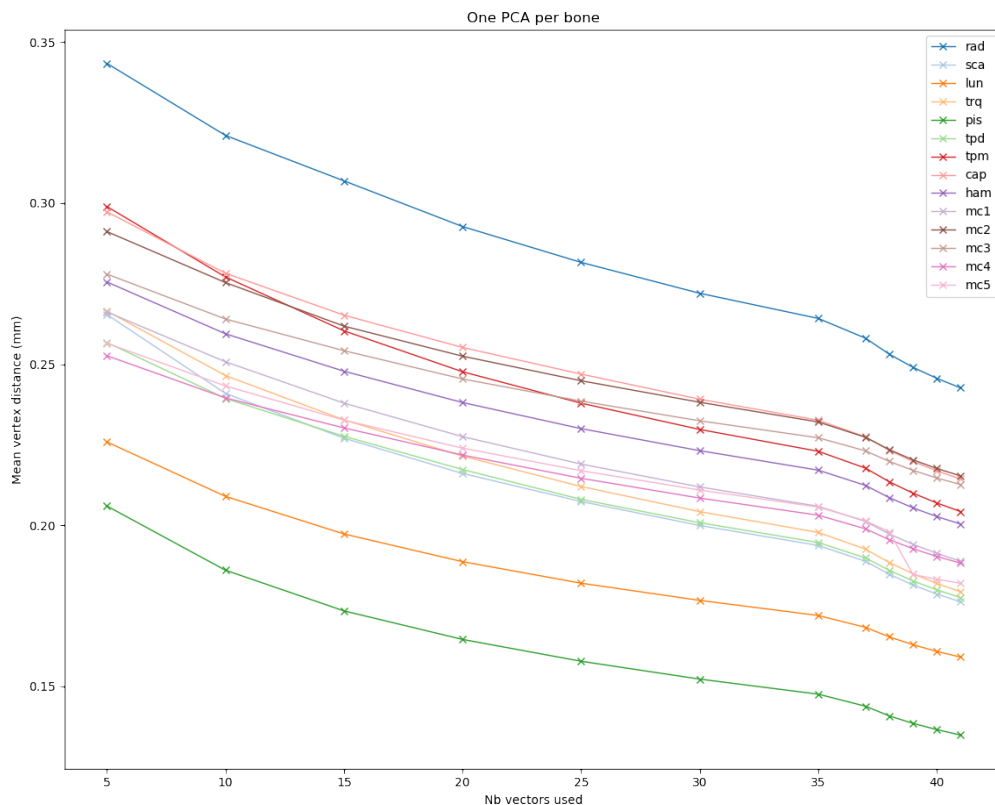


Figure 3.3: Influence of the number of principal modes used for the SSM registration. Each bone is captured by its individual model, every individual is by turn left out of the training set before being targeted by the models. The distance is computed between the registered model and the target meshes using a mean distance (1.1).

When considering the model of the whole wrist, the results are more complex. While the distances for most of the bones between the model and the target meshes decrease with the number of modes used, for some bones they increase instead. Finally for some of them, the distance starts by increasing with the number of modes, before decreasing. It can also be observed that the curves between the mean and the Hausdorff distance in Fig. 3.5 and Fig. 3.6 are not similar while they look a lot alike when individual models are considered.

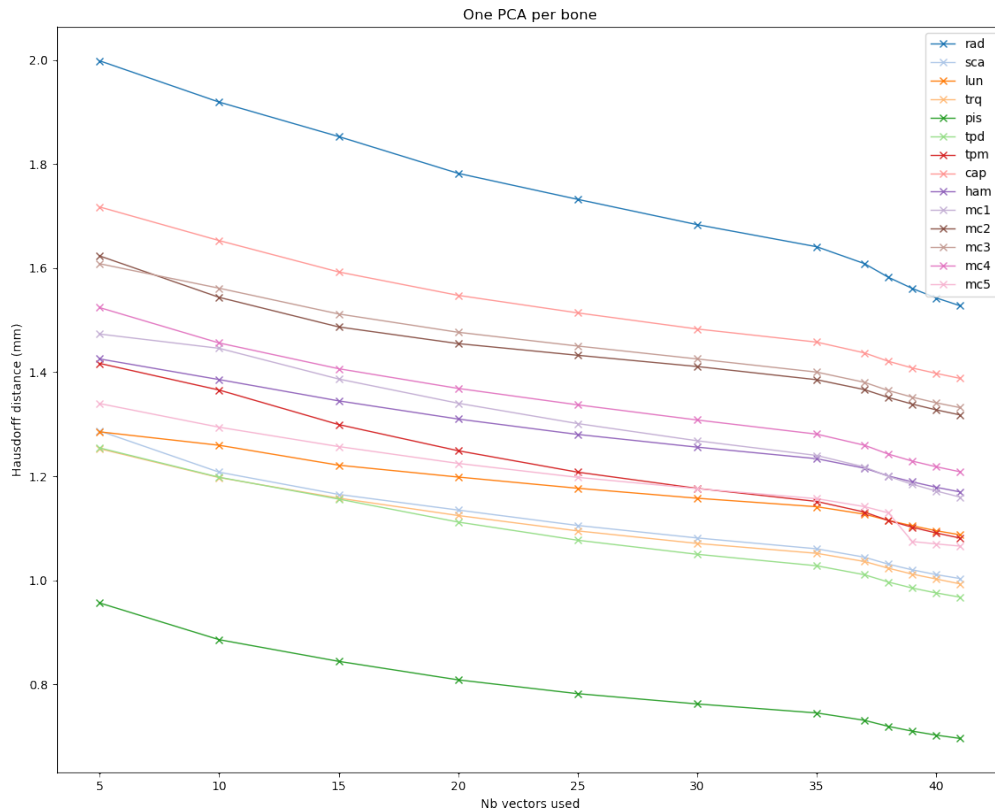


Figure 3.4: Influence of the number of principal modes used for the SSM registration. Each bone is captured by its individual model, every individual is by turn left out of the training set before being targeted by the models. The distance is computed between the registered model and the target meshes using the Hausdorff distance (1.3).

The bones with the most vertices, such as the radius and the metacarpals become strictly closer to the target shapes in mean distance when the number of modes increases. This is due to a stronger influence on the mean value compared to bones with less vertices. On the opposite, it can be noted that the pisiform, the bone with the less vertices has a distance strictly increasing with the number of modes used. For 8 bones out of 14, the mean distance between a vertex and its closest point on the paired surface is smaller than 0.32 mm, which is also smaller than the accuracy of the original data. However for the rest of them, the mean distance is higher than 0.33 mm. The Hausdorff distance is included in [1.1; 2.0] mm.

The mean distance when individual models are used is below the acquisition accuracy. However the maximal distances are still high, some details are present in one person only of the database. When the latter is taken off the training set and the models are registered to its bones, these details are not captured by the model, as testified by the high maximal distances. We can conclude that a larger training set would give better results, although these are already satisfying. Concerning the SSM modeling all wrist bones at once, the gap between the target bones and the model is too large. The number of data available are not enough for such a complex model, details are buried in the

general shapes of the bones. It must also be noted that various profiles of people have been scanned to compose the CMC database. Young and old people, males and females. However nothing guarantees that all types of wrists are present in the database, and these results rest upon the quality and diversity of the database.

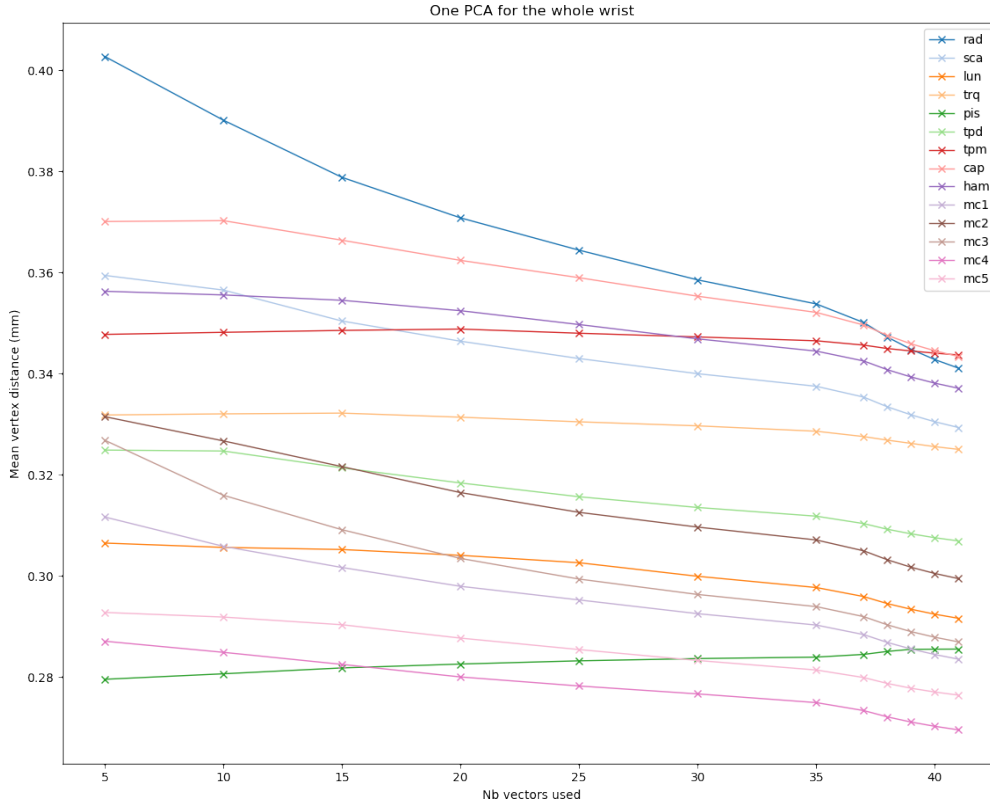


Figure 3.5: The influence of the number of principal modes used for the SSM registration. The whole wrist is captured by the model, every individual is by turn left out of the training set before being targeted by the model. The distance is computed between the registered model and the target meshes using a mean distance (1.1), the distance to each bone being separately measured, while all bones were deformed at once by a unique model.

Correspondence quality factors

In a second time, we use the individual SSMs of the bones to evaluate the correspondence quality factors between the meshes $M_{W\{b,i\}}$ previously generated. Indeed we have so far only been concerned by shapes similarity (Sec. 2.3), not correspondence between vertices.

The evaluation of the correspondence relations proposed by Davies et al. [DCT01] (Sec. 1.4.5) is based on the quality of the SSMs resulting from the corresponding meshes. We present the values for the 3 factors: compactness, specificity and generalization in Table 3.1. The factors definitions were presented in Sec. 1.4.5. For all factors, the lower the value is, the better. However, specificity and generalization of a model are opposite goals, one can only be improved at the expense of the other.

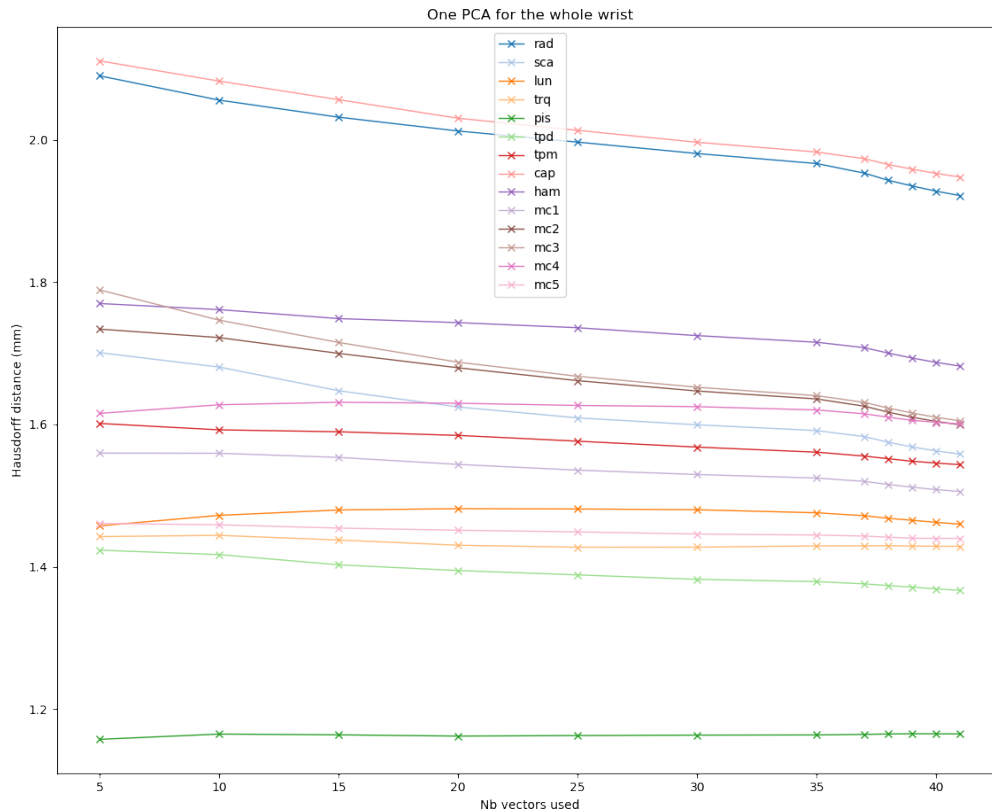


Figure 3.6: The influence of the number of principal modes used for the SSM registration. The whole wrist is captured by the model, every individual is by turn left out of the training set before being targeted by the model. The distance is computed between the registered model and the target meshes using the Hausdorff distance (1.3), the distance to each bone being separately measured, while all bones were deformed at once by a unique model.

We have computed these factors based on 39 principal modes for each individual model, one model describing one bone. The three factors are useful to compare various correspondence methods used on a same database. However, they can not be interpreted on their own. We give their values as reference, should anyone propose another set of corresponding meshes from the same database.

PCA-models are frequently used for the modeling of 3D shapes. They are easy to compute and to employ. Such SSMs are convenient for encoding prior information about classes of shapes. However, they are linear model, and if they are robust towards noise, they can only represent shapes that are in the linear span of their training set. We propose therefore in a second phase to work with statistical models based on Gaussian Processes, which can describe a larger span of shapes from the same training set by enforcing other properties of the shapes deformations, such as smoothness.

	Specificity (mm)		Generalization (mm)		Compactness
	Dist (1.1)	Dist (1.3)	Dist (1.1)	Dist (1.3)	
Radius	0.202	1.645	1.052	4.064	7126
Scaphoid	0.176	1.024	0.720	3.453	893
Lunate	0.145	1.117	0.701	2.873	579
Triquetrum	0.172	1.022	0.709	3.114	482
Pisiform	0.108	0.490	0.565	2.455	296
Trapezoid	0.140	0.857	0.612	2.574	648
Trapezium	0.213	0.952	0.639	3.329	542
Capitate	0.235	1.371	0.711	4.274	1261
Hamate	0.168	0.901	0.701	3.647	967
Metac. 1	0.182	1.079	1.033	3.917	2529
Metac. 2	0.228	1.337	1.023	3.814	4674
Metac. 3	0.225	1.525	0.985	5.406	4827
Metac. 4	0.175	1.113	0.889	3.367	2258
Metac. 5	0.077	0.745	0.861	3.143	2156

Table 3.1: Evaluation of correspondence quality based on the SSMs modeling one bone each and 39 principal modes with the three standard criteria: Generalization, Specificity and Compactness.

3.2.3 Gaussian Processes

Models based on a PCA are commonly used for shape analysis and prior information for image segmentation for instance. We propose to use models based on Gaussian Processes. It rests on two observations: PCA-based models are linear, and can only represent shapes in the span of their training set. Non-linear models could widen the range of shapes that can be represented, which is especially interesting when the quantity of data available is small. Moreover the use of PCA-based models is entirely automatic, users have no possibility of intervention, even when it is clear to a human eye that the model registration results are false. It is all the more regrettable that doctors accumulate a lot of knowledge about bone shapes or image segmentation that cannot be used by the model. Gaussian processes can be used to create parametric models that are non-linear. They can also integrate knowledge provided by a user in their prior information and adapt consequently the model. We will firstly detail the reasons that make Gaussian Processes more adapted for modeling. Then we will briefly introduce the mathematical background (for further details, the reader is referred to [LGJV17, Duv14, WS01]). Finally, we will present the two models that we have computed: a parametric one, entirely automatic and another one intended for user interaction.

Statistical models based on a Principal Component Analysis are linear parametric models. They are very specific, due to their limited capacity of representing shapes that are necessarily in a linear span of the training set. This specificity is an upside, it makes the model robust towards artifacts and noise. However, this specificity can also be a downside when the training set is small, it jeopardizes the generalization capacity of the model [LFGV17]. Yet appropriate databases can happen to be small, in particular for medical images. Furthermore, if the training data are composed of healthy subjects only, the model will be unable to characterize pathologic instances of the class. It may be enough for automatic detection of irregularities, but the model won't be able to adapt to the new instance. Finally these models are by nature designed to be embedded into fully automatic algorithms. The user has no control over the results.

Gaussian Process models characterize the possible deformations of a shape based on kernels. The kernels can describe prior information based on training data, but can also be analytically created to enforce properties such as smoothness or symmetry. Multiple kernels can be combined to blend their features. The use of such customized kernels enables the non-linearity of the model, and the span of the possible shapes represented by the model is widened compared to the PCA-based model. It allows to reduce the bias induced by a limited number of instances in the training set. A second property of such a model is that depending on the kernel used, if the latter is independent of any training set, the model can describe a continuous shape independently of the points distribution. The model is also able to integrate new posterior information, and to adapt to take it into account. It enables user interaction, a human can indicate the location of some points. It can especially be handy for pathologic cases that can not be grasped by the model based on its kernel only. Additional human information for vertices wrongly registered by the model would enable the characterization of any form. Theoretically, helped with external knowledge, any accuracy of registration could be reached. The

final results can be validated by the user, which enable the use of external knowledge brought by specialists.

Most existing statistical shape models of wrists are based on a Principal Components Analysis (PCA), or derivative methods. We propose to use a model for two applications: one fully-automatic registration of shapes, to compare with the PCA-based model, and another one fully dependent on external information: the expected corresponding final set-up is a continual interaction between the algorithm and the user, who gives any information he judges needed.

Our work has been mostly based on Lüthi et al articles [LJV13, LFGV17, LGJV17].

3.2.3.a What are Gaussian Processes Morphable Models (GPMM)

In this subsection is introduced the theory behind the GPMMs. These models were introduced by Lüthi et al. and are explained in details in a series of articles including [LFGV17, LGJV17]. In a first paragraph the mathematical concepts behind the models are introduced. Then in a second paragraph the models theory is described, along with various possibilities of covariance kernels and their effects for the model.

Gaussian Processes

A *stochastic Process* generalizes the concept of random variable. It is composed of a collection of random variables, which all take values from the same mathematical space. Often the random variables can be indexed by some mathematical set. A *Gaussian Process* is a stochastic process composed of random variables, possibly an infinity of them, such that any finite subset of these variables follows a multivariate normal distribution. The Gaussian process distribution is the joint distribution of all its random variables, and as such is a distribution over functions with a continuous domain, for example space. This property is very interesting in the case of the GPMMs as it allows to describe shape deformations as vector fields independently of the discretization. This is not the case with SSMs which are defined for a unique vertex distribution over the surface. A Gaussian process $\mathcal{GP}(\mu, k)$ is completely defined by its second-order statistics: its mean μ and its covariance k .

Let us consider the covariance function k of a Gaussian Process $u_t \in \mathcal{GP}(0, k)$ for $t \in \Omega$, Ω is a subset of \mathbb{R}^d . A linear operator \mathcal{T}_k is associated to k such that:

$$\begin{aligned} \mathcal{T}_k : L^2(\Omega) &\rightarrow L^2(\Omega) \\ f &\mapsto \mathcal{T}_k f = \int_{\Omega} k(s, \cdot) f(s) p(s) d(s) \end{aligned} \quad (3.7)$$

The eigenvalues and eigenfunctions pairs (λ_i, Φ_i) of the linear operator \mathcal{T}_k are found by solving the equation:

$$\int_{\Omega} k(s, t) \Phi_i(s) p(s) ds = \lambda_i \Phi_i(t) \quad (3.8)$$

$p(s)$ is a density function defined on Ω . The *Karhunen-Loève theorem* states that a Gaussian Process can be represented as an infinite linear combination of orthogonal functions $\{\Phi_i\}_{i=1}^{\infty}$, its covariance's eigenfunctions:

$$u \sim \sum_{i=1}^{+\infty} \alpha_i \sqrt{\lambda_i} \Phi_i, \quad \text{s.t. } \alpha_i \in \mathcal{N}(0, 1) \quad (3.9)$$

On the opposite of other expansions, the orthogonal basis functions depend on the process, determined by its covariance function. The coefficients in the Karhunen-Loève theorem are independent Gaussian random variables $\{\alpha_i\}_{i=1}^{\infty}$. Due to the latter property, the eigenvalues λ_i explain the variance associated to the i^{th} component. Therefore, if the sorted λ_i decrease sufficiently quickly, a low rank approximation of u can be used:

$$\tilde{u} \sim \sum_{i=1}^r \alpha_i \sqrt{\lambda_i} \Phi_i \quad (3.10)$$

This approximation enables to get a parametric low-dimensional model from the Gaussian Process. The associated error is given by:

$$\sum_{i=r+1}^{\infty} \lambda_i \quad (3.11)$$

The Karhunen-Loève theorem is closely related to the Principal Component Analysis, since the latter is also called Karhunen-Loève transform and is an empirical use of the Karhunen-Loève theorem.

The approximation (3.10) can only be used if the eigenvalues and eigenfunctions $(\lambda_i, \Phi_i)_{i=1}^r$ can be computed. Lüthi et al. propose to estimate the pairs using the Nyström method, which approximates the integral of (3.8). The integral over $p(x)$ is replaced by an empirical average over randomly sampled points $\{x_1, \dots, x_n\}$, sampled according to p . It leads to a matrix eigenproblem:

$$K^{(n)} U^{(n)} = U^{(n)} \Lambda^{(n)} \quad (3.12)$$

with $K^{(n)}$ the kernel matrix such that $K_{ij}^{(n)} = k(x_i, x_j)$, $i, j = 1, \dots, n$. The columns of $U^{(n)}$ are eigenvectors, $\Lambda^{(n)}$ is a diagonal matrix with the corresponding eigenvalues $\lambda_1 \geq \lambda_2 \geq \dots \lambda_n \geq 0$. The Nyström approximation of the i^{th} eigenfunction is:

$$\Phi_i(y) \approx \frac{\sqrt{n}}{\lambda_i^{(n)}} k_y \cdot u_i^{(n)} \quad (3.13)$$

with $k_y = (k(x_1, y), \dots, k(x_n, y))$ and $u_i^{(n)}$ the i^{th} column of $U^{(n)}$. The eigenvalues $\lambda_i^{(n)}$ approximate the λ_i s.

Gaussian Process Morphable Model

Gaussian Process Morphable Models are a generalization of more classical SSMs such as the PCA-based ones. The deformations undergone by a shape are modeled as a Gaussian Process, which is fully characterized by its mean and covariance functions. Due to the Karhunen-Loève expansion of Gaussian processes and its resulting low-rank approximation, a parametric low-dimensional model describing the deformations can be computed, using the Nyström method.

It must be noted that PCA-based models are usually employed for modeling shapes variations using a normal distribution $\mathbf{x} \sim \mathcal{N}(\bar{\mathbf{x}}, C)$, \mathbf{x} being a shape. However, instead of describing shapes, SSMs can model deformations undergone by the mean shape. Let Δ be the deformations modeled, then similarly to (3.6), $\Delta = wV^t\sqrt{\Lambda}$ and $\Delta \sim \mathcal{N}(0, C)$. The latter interpretation is the one used for GPMMs, the probabilistic model is defined directly on the deformations undergone by the mean shape. The generation of shapes from deformations simply consists in adding the mean shape to the deformations.

A Gaussian Process is characterized by its mean and covariance functions. The functions defining the model must be carefully chosen, as they impart its specific properties. Some such properties can enforce smoothness, periodicity, symmetry, and so on. We will only discuss two kernels that are of interest for shape deformation modeling, but many more possibilities exist, either for modeling or other applications.

The first property that we are interested in is *smoothness* of the deformations. A very simple assumption consists in using a zero mean function. It implies that the reference shape that is being deformed is a representative instance of its class of shapes, close to a mean shape. Many different kernels can be used to enforce smoothness, one of the most classical one being a Gaussian kernel:

$$k_g(x, y) = s \cdot I_{3 \times 3} \cdot \exp(-\|x - y\|^2 / \sigma^2) \quad (3.14)$$

$x, y \in \Omega \subset \mathbb{R}^3$, with $\Omega = S_R, S_R$ being the reference surface that is being deformed. $s \in \mathbb{R}$ characterizes the scale of the deformation and σ defines the range of influence of a point. Finally, the identity matrix $I_{3 \times 3}$ signifies that the 3 dimensions of the vector field are independent.

This model incorporates no prior knowledge about a shape, and can therefore be applied to any shape, no matter its point distribution or the absence of training shapes. However, when a set of valid shapes are available for training, it is ideal to learn valid deformations from them. We are therefore interested in a second time in *learning prior information from a training set*. If n valid shapes are in correspondence, deformation fields $\Delta_1, \dots, \Delta_n$ can be learned from the points locations, by subtracting the mean shape points positions. A Gaussian Process $\mathcal{GP}(\mu_p, k_p)$ modeling these deformations can be computed:

$$\mu_p(x) = \frac{1}{n} \sum_{i=1}^n \Delta_i(n) \quad (3.15)$$

$$k_p(x, y) = \frac{1}{n-1} \sum_{i=1}^n (\Delta_i(x) - \mu_p(x))(\Delta_i(y) - \mu_p(y))^T \quad (3.16)$$

On the opposite of the Gaussian kernel, the deformation field is only known for the point distribution of the corresponding shapes.

The only requirement for a matrix to be a valid Gaussian Process covariance function is that it should be symmetric and positive semi-definite. Algebraic rules define authorized operations between valid kernels to combine them into more complex ones. It enables the accumulation of various effects into complicated models. For example, a kernel resulting from a sum of Gaussian kernels with various s and σ values would allow multi-scale deformations, piling up global tendencies with finer and more local details. Other combinations can be used to make models more local or else to define partitions of the shape and apply various transformations depending on the section of the partition. More details about such combinations of transformations can be read in [LGJV17].

We are interested in making the most of the valid shapes available in the CMC database. However when the training set is limited, the span of shapes that can be represented by the model might not encompass the full shape space. In this case, the model is biased towards the training shapes. It is possible to reduce the bias by using a Gaussian kernel with parameter σ chosen large and s equal to the average error made by the prior model alone, as studied in [LJV13]. It is based on the assumption that deformations are smooth and errors are spatially correlated. Therefore, we combine the prior learned from the training set in $\mathcal{GP}(\mu_p, k_p)$ with a Gaussian kernel $\mathcal{GP}(0, k_g)$. The new model is based on a Gaussian Process $\mathcal{GP}(\mu_p, k_p + k_g)$

Another interesting property of a Gaussian Process based model is the ability to combine prior information and locations of some points given by a user to compute a new *posterior model*. Let Δ be the deformation modeled by a Gaussian Process, describing the prior information:

$$\Delta \sim \mathcal{N}(M, K) \quad (3.17)$$

If Δ is in the form of a vector, describing the deformation for a point distribution then M and K are respectively a vector and a matrix. The most probable prior shape deformation is the mean vector M .

The user provides the actual deformations $\delta_{\text{obs}} = \{\delta_1, \dots, \delta_q\}$ of points $\{p_1, \dots, p_q\}$. Δ can be decomposed into two vectors Δ_Y and Δ_Z such that Δ_Z describes deformations for points $\{p_1, \dots, p_q\}$, while Δ_Y characterizes deformations for all the other points. M and K are decomposed accordingly:

$$\Delta = \begin{pmatrix} \Delta_Y \\ \Delta_Z \end{pmatrix} \sim \mathcal{N} \left(\begin{pmatrix} M_Y \\ M_Z \end{pmatrix}, \begin{pmatrix} K_{Y,Y} & K_{Y,Z} \\ K_{Z,Y} & K_{Z,Z} \end{pmatrix} \right) \quad (3.18)$$

Except if K is an identity matrix, points are related to each other and the movement of one point influences its neighbors. Δ_Y is modeled by a new Gaussian Process taking the added posterior information δ_{obs} into account:

$$\Delta_Y | \delta_{obs} \sim \mathcal{N}(M', K') \quad (3.19)$$

such that:

$$\begin{aligned} M'(p) &= M(p) + K_{p,Z} K_{Z,Z}^{-1} (\delta_{obs} - \Delta_Z) \\ K'(p, p') &= K(p, p') - K_{p,Z} K_{Z,Z}^{-1} K_{Z,p'} \end{aligned} \quad (3.20)$$

The posterior model of the whole shape deformations is defined in eq. 3.21, and the most probable shapes are those characterized by the new mean.

$$\begin{pmatrix} \Delta_Y \\ \Delta_Z \end{pmatrix} \sim \mathcal{N} \left(\begin{pmatrix} M'_Y \\ \delta_{obs} \end{pmatrix}, \begin{pmatrix} K'_{Y,Y} & 0 \\ 0 & 0 \end{pmatrix} \right) \quad (3.21)$$

So far we have assumed that information given by the user are exact. It is however reasonable to suppose that it might be *noisy*. Indeed 3D shape visualization on a computer is tricky and so is the definition of exactly corresponding points. Then the observed deformations $\tilde{\delta}_{obs} = \{\tilde{\delta}_1, \dots, \tilde{\delta}_q\}$ are such that

$$\tilde{\delta}_i = \delta_i + N, \quad \text{s.t. } N \sim \mathcal{N}(0, \epsilon^2 I_{3 \times 3}) \quad (3.22)$$

δ_i is the exact deformation for point p_i , $\tilde{\delta}_i$ is the observed one. N represents the noise and ϵ is a parameter to scale it. The prior model becomes:

$$\Delta_n = \begin{pmatrix} \Delta_Y \\ \Delta_Z \end{pmatrix} \sim \mathcal{N} \left(\begin{pmatrix} M_Y \\ M_Z \end{pmatrix}, \begin{pmatrix} K_{Y,Y} & K_{Y,Z} \\ K_{Z,Y} & K_{Z,Z} + \epsilon^2 I_{3q \times 3q} \end{pmatrix} \right) \quad (3.23)$$

and:

$$\Delta_n | \tilde{\delta}_{obs} \sim \mathcal{N}(M'_n, K'_n) \quad (3.24)$$

such that for any points p, p' of the shape, whether among the observed ones or not:

$$\begin{aligned} M'_n(p) &= M(p) + K_{p,Z} (K_{Z,Z} + \epsilon^2 I_{3q \times 3q})^{-1} (\delta_{obs} - \Delta_Z) \\ K'_n(p, p') &= K(p, p') - K_{p,Z} (K_{Z,Z} + \epsilon^2 I_{3q \times 3q})^{-1} K_{Z,p'} \end{aligned} \quad (3.25)$$

The GPMM describes the deformations of a shape. The training set is constructed from the matrix of shapes \mathbf{X} defined in Sec. 3.2.2.a. The matrix is centered using $\mathbf{X}_c(i, j) = \mathbf{X}(i, j) - \bar{\mathbf{x}}(j)$ with $\bar{\mathbf{x}}$ calculated using (3.1). When a new deformation is simulated with the model, the equivalent shape is generated by summing the deformation and $\bar{\mathbf{x}}$. In the following section, such a model was computed with our data, we present the results.

3.2.3.b Applications

We test GPMMs for 3D shape registration towards the CMC database meshes $M_{R,\{b,i\}}$. The bones are considered separately, a model only describes one bone. The registrations are done in a leave-one-out manner: the target bone is systematically removed from the training set of the model. We use two distinct strategies to register the model to the target. First, we focus on the property of the Gaussian Processes to adapt to posterior information. It is aimed at using external knowledge brought by a human user. In a second part, we will focus on an fully automatic registration method, similar to a SSM registration, based on deformation described by vectors.

Registration based on external inputs

One of the arguments in favor of a Gaussian Process-based model is the exploitation of human knowledge, to fill in potential gaps of training data. Thus, we test a registration of models to new wrists completely based on external inputs. We have chosen to work with models based on a Gaussian Process $\mathcal{GP}(\mu_p, k_p + k_g)$ combining knowledge from training data with the assumption that deformations are smooth. [LJV13] found out that it is an efficient covariance kernel for model registration.

The algorithm leading to model registration based on user input is:

1. $t = 0$: For a given target mesh $M_{R,\{b,i\}}$, the corresponding model $G_{\{b,i\}}(\mu_t, k_t)$ is computed by using all $M_{W,\{b,i\}}$, $j \in \{1, \dots, n\}, j \neq i$ as training set.
2. $M_{G_{\{b,i\}}(\mu_t, k_t)}$ is aligned to $M_{R,\{b,i\}}$ using affine transformations.
3. The point $v_k \in G_{\{b,i\}}(\mu_t, k_t)$ with the biggest variance is computed based on k_t
4. **User input:** The desired location for one point of $M_{G_{\{b,i\}}(\mu_t, k_t)}$, whether v_k or another one. The deformation is calculated from the position
5. $t = t + 1$: μ_t and k_t are updated according to (3.25)
6. $d_{\text{mean}}(M_{G_{\{b,i\}}(\mu_t, k_t)}, M_{R,\{b,i\}})$ is computed using (1.1)
7. **User input:** "Ok" \rightarrow End of the algorithm; "Nok" \rightarrow Repeat 3. to 7.

$M_{G_{\{b,i\}}(\mu_t, k_t)}$ is the mesh describing the most probable shape according to the model of shape deformation. It is simply the sum of the mean mesh and the mean deformation μ_t at time t .

The registration continues until the similarity of the shapes given by $d_{\text{mean}}(M_{G_{\{b,i\}}(\mu_t, k_t)}, M_{R,\{b,i\}})$ is considered satisfying by the external user. The user can run the algorithm until he has manually given the positions of all points forming the model. In this extreme case any shape can be described, if technically possible for the number of vertices. Hence even shapes very different from the ones in the training set can be described, such as pathologic cases that can be caused by sickness or accidents.

To begin with, this registration method is tested with a simulated ideal user. The coordinates given by the user are supposed exact. In step 5. μ_t and k_t are updated using (3.20). To give exact positions, it is assumed that the optimal registration of the model $G_{\{b,i\}}$ towards the target mesh $M_{R,\{b,i\}}$ is equal to $M_{W,\{b,i\}}$. Additionally the

user systematically provides information about the vertex that has at the moment the greatest variance according to the model's kernel. Indeed it is the point for which there is the greatest uncertainty about its deformation, and potentially the most info to learn from: it is likely to influence a bigger area around it than another point with less variance.

The number of points needed from the user to reach some similarity levels are tested with an algorithm that simulates an ideal user. This algorithm always chooses the point with the biggest variance, to maximize the information of the input, and the location given is considered as accurate, while a human user might be imprecise, especially when visualizing 3D volumes on a 2D screen. Three distances between the target mesh and the one stemming from the model are tested: 0.3, 0.25 and 0.2mm. 0.3 mm is just below the original accuracy of the CT scans ($0.33 \times 0.33 \times 0.625$ mm). Most individual PCA-based models reach an accuracy in range [0.2; 0.25] mm when they are registered to a new mesh. The registration was tested for all persons and all bones of the CMC database at turn in a leave-one-out manner. The minimum number of points required correspond with the number of iterations needed to drop below the similarity levels. The average minimum number of points are presented in table Table 3.2.

Distance max. btw. the meshes	< 0.3mm	< 0.25mm	< 0.2mm
Radius	37	53	80
Scaphoid	13	16	23
Lunate	11	15	23
Triquetrum	12	18	30
Pisiform	7	10	17
Trapezoid	11	16	28
Trapezium	17	26	43
Capitate	23	34	58
Hamate	20	29	48
Metac. 1	22	32	52
Metac. 2	29	45	78
Metac. 3	27	37	65
Metac. 4	23	33	56
Metac. 5	22	33	55

Table 3.2: Average minimum number of vertices required to reach level of similarity between a target mesh $M_{R,\{b,i\}}$ and a GPMM registered $M_{G\{b,i\}}$ using only posterior information

While these numbers are not that high compared to the total number of vertices composing each bone (Table 2.2), for some bones they are high when the time needed by an actual human being is considered, especially when a good similarity of shapes is expected. Manipulating 3D meshes on a 2D computer screen to accurately locate the target position of a point, even when helped by tools such as magnets is highly time consuming. The total time needed would be considerable for several tens of points.

All the more so that Table 3.2 was computed in ideal conditions, a real user would probably need more points to reach the same similarity levels. With an actual human user, the algorithm would consider the information given as noisy. Moreover the user could decide to give locations of vertices that are more remarkable due to their location instead of filling in the ones with the most variance.

From this experiment, we conclude that a registration method completely based on human inputs is unrealistic. It requires too much time to be convenient in real conditions.

Automatic registration based on the Karhunen-Loève approximation

In a second time, GPMMs are being registered to a target mesh with an automatic optimization approach. The procedure is very similar to the PCA registration. It is aimed at comparing the results of the linear SSMs registration with ones, to compare the use of a linear model with

The registration is based on the low rank Karhunen-Loève approximation presented in (3.10). Any deformation can be approximated by a sum of vectors balanced by their associated eigenvalues and a vector α weighting the importance of each vector for the current deformation. These vectors are computed from the covariance function of the Gaussian Process using the Nyström method. The automatic registration of the model to the target mesh is similar to the SSM registration: the values of α are optimized to minimize the difference between the target shape and the deformed template. We use the same procedure as the one presented in [LGJV17]. The parametric form of the registration problem is the following:

$$\alpha^* = \underset{\alpha}{\operatorname{argmin}} \quad d_{\text{mean}} \left(\mathbf{x}_{\text{target}}, \bar{\mathbf{x}} + \mu + \sum_{i=1}^r \alpha_i \sqrt{\lambda_i} \Phi_i \right) + \eta \sum_{i=1}^r \alpha_i^2 \quad (3.26)$$

We did not have a chance to conduct an extensive review on GPMMs registration due to a lack of time. We have heavily based our experiment on the work of Lüthy et al. We have chosen to work with parametric models of 40 vectors, to have a comparable number of vectors than the SSMs, so comparisons make more sense. One model per bone was used. Our Gaussian Processes were a composition of the estimation of an empirical model based on a training set and a Gaussian kernel to model the deformations smoothness. This composition was found to be the most effective one for registration in [LJV13]. Only one set of parameters for the Gaussian kernel was tested: in (3.14), σ represents the smoothness and was chosen large to model global deformations: $\sigma = 10$. s defines the scale of the average error, and was chosen to be $s = 0.5$. A leave-one-out approach was used, for two subjects randomly selected. The average similarity between the optimized GPMMs and the target meshes are presented in Table 3.3. They are compared to the registration results of the SSMs for the two same individuals.

The results in Table 3.3 show that both models are under the 0.3 mm threshold, though the SSM ones perform better. However, the GPMMs have not been optimized at all, only one set of parameters were tested, and there's every chances that they are not the most appropriate ones. Additionally on the opposite of the SSMs, the number of

	GPMM		SSM	
	d_{mean} (mm)	$d_{\text{Hausdorff}}$ (mm)	d_{mean} (mm)	$d_{\text{Hausdorff}}$ (mm)
Radius	0.268	2.950	0.236	1.460
Scaphoid	0.219	1.280	0.137	0.805
Lunate	0.144	0.738	0.132	0.871
Triquetrum	0.189	0.895	0.151	0.843
Pisiform	0.181	0.883	0.130	0.732
Trapezoid	0.223	0.987	0.161	0.765
Trapezium	0.242	1.078	0.156	1.104
Capitate	0.224	1.449	0.204	1.231
Hamate	0.220	1.429	0.201	1.123
Metac. 1	0.198	1.204	0.178	1.022
Metac. 2	0.225	1.798	0.184	1.668
Metac. 3	0.183	1.142	0.168	0.964
Metac. 4	0.190	1.063	0.151	0.840
Metac. 5	0.182	0.925	0.055	0.413

Table 3.3: Distance between the target mesh and the registered GPMM based on a distance minimization of the parametric model using 40 modes. Comparison with the registration of the SSMs based on 39 modes.

modes used by the GPMMs could also be increased, it is not limited by the size of the training set on the opposite of the linear model. Therefore, it can be expected that with optimal models the results could be improved.

3.2.4 Discussion

In this section we have used the dense correspondence between bones of the CMC database previously computed to model the shapes variability. We have proposed two different models: one built with a PCA, another one based on Gaussian Processes.

The PCA-based models have proven to achieve good results for the registration of new shapes outside their training set, when a different model is used for each bone. The model describing the whole wrist at once couldn't replicate the shapes with a good enough level of details. The number of modes available, depending on the number of shapes in the training set was too poor to catch all the features.

In a second phase, Gaussian Processes were used to model the variability of the deformations undergone by the mean bone shapes. They were then registered in turn to the database meshes, using two methods: one stepwisely incorporating posterior information from a user and one based on a parametric approximation of the Gaussian processes. The first approach has proven to require too many given points to be used on real conditions with a human user though a good similarity could be reached when enough information is provided. The second approach has not been extensively tested,

but achieve similar results as the SSMs while the parameters have not been optimized. It is promising, and should be further studied.

The individual SSMs were quite effective to approximate new shapes. In the next section, they will be further tested by using them to register bones of a new database, in order to define correspondence between this second database and the CMC one.

3.3 NIH reparameterization

In Sec. 3.2 were computed Statistical Shape Models using PCA. The registration results of the SSMs were promising, particularly the individual models which could approximate the CMC database meshes with a mean distance below 0.3 mm. These models were used to register the only publicly available wrist database: the NIH database [MCTL07].

Correspondence for the NIH database was not computed by using the same method than the one used for the CMC database introduced in Chapter 2. Indeed, this database present additional difficulties: the radii and metacarpals are cut, and only small and variable portions of these bones are visible. It makes the alignment between the bones complicated, and while templates describe common information to all subjects, it significantly limits knowledge to be learned from these bones, only carpal bones are entirely known.

On the other hand, using the PCA-based SSMs computed with the CMC database to register the NIH database offers several interests. At first, as previously mentioned, a model quality is dependent on its training data diversity, and its assessment relies on the diversity of the test set. Therefore to have the possibility to test the model on more data from another database is an opportunity to further validate the model. Moreover if the results are good enough, the registered models can serve as a reparameterization of the NIH database. In this case the 60 wrists would be in dense correspondence with the CMC database, which would enable the use of both databases at once for the calculation of more complete models for instance. Or deeper shape analysis could be carried out due to the larger amount of data, since there are high chances that a larger span of wrists types are covered. Moreover, additional information can be learned from the models adjustments to the NIH bones: the CMC-based models encode complete metacarpals, and can be used as hints of what the whole bone shapes are like.

3.3.1 Dense correspondence mapping of the NIH using the SSMs

Similarly to the original meshes of the CMC database, the vertices of the raw meshes of the NIH database are irregularly spread along the bones surface (see Fig. 1.19). This uneven distribution can skew the distance measures between meshes. A first step consists in resampling the bones to describe the shapes with the same number of vertices, but with an homogeneous distribution and a stable edge length. As previously, this resampling is computed using the graphite software [Lé], based on a Centroidal Voronoi Tessellation. These resampled homogeneous meshes are later on used as reference shapes. On the opposite of the post-segmentation processing that was performed on the first database, we did not need to remove coarse errors of segmentation.

To be able to adapt the statistical models to the bones, the latter have to be aligned to the former. Our optimization algorithm includes refinement of the rigid and scale alignment to the model at every iterations. However shapes of short radii are too different to the associated model, which makes basic shape alignment impossible, preprocessing is required. Six feature points were manually selected on all radii and metacarpals of the NIH database and on the mean models. The bones were then

roughly aligned to the models by minimizing the distances between sets of feature points. Additional adjustments could be manually done if needed. For each bone, the plane along which it had been cut was computed, and any vertex within one millimeter of the plane or beyond it was listed. A customized model was created for each bone by removing all recorded vertices, so both shapes would be similar. Vertices within one millimeter of the cut plane were also removed from the database meshes, these points being absent from the associated model. Carpal bones were roughly aligned by using the transformation matrix of the radii, it is enough to guarantee the convergence of the alignment algorithm.

Afterward, the models are being registered to the database bones. The latter are individual SSMs of each bone, computed with a training set of 42 wrists from the CMC database (please refer to Sec. 3.2.2). According to the mean shape, the eigenvectors and their associated eigenvalues, the best parameters to approximate each NIH bone are calculated. It was decided that 39 vectors would be used for the models, which is almost all available vectors. Indeed throughout the leave-one-out tests of the SSMs, it was proven that the more vectors are used, the better the results.

The SSMs of the radius and metacarpals describe the entire bones, however a portion only of the bone can be registered to the targets. All vertices of the SSM previously listed as beyond the cut plane for the current subject are therefore ignored during the distance computation. Moreover the refinement of the bone alignment by the optimization algorithm uses the customized model associated to the target, deformed in the same way than the SSM. Two radii of the NIH database had such a small part of them captured that they were discarded from the calculations.

In order to use the NIH database for further studies, we want to perfectly capture the details of the bones. Yet, if the results of the SSMs are comparable with the ones obtained with the leave-one-out method on the CMC database, we expect to correctly approximate the global shapes of the bones, but details should be missed by the registration. Therefore, in addition to the model registration via optimization of the parameters, a second step of projection along the normals is added. The same process was used when the CMC database was reparameterized (please refer to Sec. 2.2.4.d). The shapes being already really close from each other, the points are not projected far, which prevents the meshes from having crossed faces or wrongly projected points. It allows to refine the registration by capturing the sharp details of the targets. All points listed as beyond the cut plane of the target mesh are removed from the final meshes, no corresponding target surface exists to project them onto.

Finally the resulting meshes are moved back to their target bones initial positions and orientations, to reconstruct the wrists. Two types of final wrists are available: the ones described by a deformation of the SSMs that include the whole metacarpals and a large portion of the radii, thanks to the extra information brought by the SSMs. The second type is composed of more precise meshes, that were projected onto the target surfaces, but only the portions of bones visible in the initial data are apprehended by the new meshes. Both types of wrists are in correspondence with the CMC database by construction. Only the similarity of shape between the database bones and the resulting meshes need to be validated, which is analyzed in the next section.

3.3.2 Numerical Validation

In the previous section was described the correspondence mapping of the NIH database with the CMC database. It was performed by optimizing individual SSMs previously created based on the second database to register the new one. In addition to the optimization of the SSMs, a second set of resulting meshes was created by additionally projecting the deformed SSMs towards the target bones. By construction all meshes of bone b for any subject are in correspondence with the ones of the CMC database, whether resulting from SSM deformation or further projection along the normals. To assess the quality of the correspondence mapping meshes, and to prove that they can be used instead of the original raw meshes, only the similarity of the encoded shapes needs to be evaluated.

NIH resampling

At the very first, the NIH database has been resampled, to be described by an homogeneous distribution of points over the surface. The treatment is the same than the one applied to the CMC database. Similarly, this step is very important, since the resulting meshes are used as reference for the rest of the work. If differences are introduced during this step, they will remain in the data. Therefore particular attention is paid to achieve proper outcomes.

In Table 3.4 the results of the resampling step are introduced. Dissimilarity between meshes is computed using two mesh-to-mesh distances: a mean distance from a vertex to its closest point on the paired surface (1.1) and a max distance, which corresponds to the maximal distance over all vertices of both meshes of a vertex to its closest point (1.3). The mean distance between a vertex and its closest point is in average between 0.002 and 0.004 mm and the maximal values are included in range [0.004; 0.007] mm. The Hausdorff distance is in average between 0.026 and 0.078 mm, while its maximal values are under 1.5mm, that is below the acquisition precision. Only one 1st metacarpal has a maximal value of 0.201mm, slightly above the 0.2 mm threshold. After verification, this higher value is due to small holes in the original mesh next to the cut plane that are mishandled by the algorithm. However since the holes are really close to the cut plane, they will not be taken into account in the following processes, and the distal side of the bone is not affected, so it was kept in the database

The results are in the same order of magnitude as the resampling results of the CMC database, perhaps even slightly better (please refer to Sec. 2.3.1 for the CMC database results). The precision of the initial data is between $0.2 \times 0.2 \times 1$ and $0.3 \times 0.3 \times 1$ mm. The distance between a vertex and the paired surface is in average largely below the precision of the raw data. Even in maxima, this distance is always below the initial precision, but for one bone. Given these distances, we can conclude that the resampled data perfectly characterize the original shapes of the NIH database.

Initial comparison to SSMs mean shapes

The initial similarity between SSMs mean shapes and the NIH bones shapes is measured, in order to be compared with later model registration results, to evaluate the model efficiency. In Table 3.5 are presented the distances between the individual

	Mean dist. (1.1) (mm)			Hausdorff dist. (1.3) (mm)		
	mean	max	std	mean	max	std
Radius	0.004	0.005	0.001	0.078	0.133	0.020
Scaphoid	0.003	0.004	0.000	0.043	0.068	0.009
Lunate	0.003	0.004	0.000	0.038	0.069	0.009
Triquetrum	0.002	0.005	0.000	0.037	0.073	0.010
Pisiform	0.002	0.004	0.001	0.026	0.069	0.009
Trapezoid	0.003	0.004	0.000	0.039	0.070	0.009
Trapezium	0.003	0.004	0.000	0.040	0.057	0.008
Capitate	0.004	0.005	0.001	0.051	0.084	0.010
Hamate	0.003	0.004	0.000	0.050	0.069	0.008
Metac. 1	0.003	0.006	0.001	0.060	0.201	0.029
Metac. 2	0.004	0.007	0.001	0.064	0.125	0.018
Metac. 3	0.004	0.007	0.001	0.060	0.101	0.017
Metac. 4	0.003	0.006	0.001	0.048	0.078	0.012
Metac. 5	0.003	0.006	0.001	0.052	0.104	0.018

Table 3.4: Distances between the original meshes and a first resampling to regularize the vertices and edges distribution on the surface of the NIH bones. Both mean and Hausdorff distances (1.1) and (1.3) are computed, the results are in mm.

SSMs mean shapes and the meshes of the NIH bones, when the bones have been rigidly aligned and scaled. These distances are for comparison with later results of the SSMs registration. It enables to measure the quality of the registration compared to the initial situation.

The average distance between a vertex and the paired surface is included in range [0.311; 0.747] mm, and the worst values go as high as 0.591 to 1.673 mm. In average the surfaces are far from each other, the global shapes are not captured by the mean shape. It proves the variability of shape among the same class of bones. The Hausdorff distances are in average between 1.218 and 2.779 mm, while the maximal values of the Hausdorff distance are for some bones higher than 5 mm, even up to 7.038 mm for a 1st metacarpal. Compared to the size of the bones, these distances are really high. These results are in the same order of magnitude as the difference between the CMC database meshes and the initial templates visible in 2.3. They are slightly worse for the metacarpals and the radii, due to the cut ends of the bones, although the distance functions have been modified to take these into account.

SSMs registration

When the bones are aligned and scaled to the individual SSMs, the latter are being deformed following their principal modes of variations. They are being registered to the database meshes by optimization of a mean distance function. The resulting registered SSMs are being compared to the database meshes. All vertices of the models that have been identified as having no equivalent target surface are ignored in the distance com-

	Mean dist. (1.1) (mm)			Hausdorff dist. (1.3) (mm)		
	mean	max	std	mean	max	std
Radius	0.747	1.673	0.275	2.779	7.038	1.003
Scaphoid	0.373	1.022	0.123	1.758	4.431	0.700
Lunate	0.411	1.142	0.184	1.557	2.943	0.482
Triquetrum	0.320	0.624	0.082	1.280	1.936	0.286
Pisiform	0.311	0.591	0.089	1.218	2.129	0.295
Trapezoid	0.345	0.884	0.120	1.416	2.421	0.416
Trapezium	0.362	0.875	0.127	1.508	4.221	0.553
Capitate	0.417	1.162	0.167	2.011	4.489	0.771
Hamate	0.382	1.202	0.171	1.656	4.846	0.665
Metac. 1	0.566	1.354	0.219	2.726	7.459	1.582
Metac. 2	0.556	1.372	0.180	2.070	4.064	0.642
Metac. 3	0.457	0.964	0.143	1.939	5.195	0.717
Metac. 4	0.448	1.153	0.158	1.806	5.448	0.939
Metac. 5	0.422	0.796	0.110	1.549	3.570	0.514

Table 3.5: Distances between the NIH database meshes and the SSMs mean shapes. Both mean and Hausdorff distances (1.1) and (1.3) are computed, the results are in mm.

putation. The average mean distances are included between 0.117 and 0.195 mm, while the highest mean distances are in range [0.165; 0.305] mm. The Hausdorff distances are included between 0.575 and 1.039 mm in average and between 0.879 and 2.599 mm for the maximal values.

When the registered SSMs are being compared to the mean shapes, we can observe that they are strictly closer to the target meshes, as expected. We can also note that in average the mean distance between a vertex and the paired surface is smaller than the initial precision of the data, though some of the highest mean distances are above the 0.2 mm threshold, which is the best original precision of some of the original data. We can however conclude that the global shape is well captured by the deformed models. However the Hausdorff distances for their part are quite high, details are definitely missed. These distances can be compared to the distances obtained between individual models registered using 39 principal modes to the CMC database bones, in Fig. 3.3 and Fig. 3.4. The results are slightly better for the NIH registration than they were with the leave-one-out method for the CMC database registration.

We can note that the SSMs of the metacarpals, created based on the CMC database, represent the whole bones, while they are being registered to the proximal end of the bones only. This has both upsides and downsides. The model is not exactly adapted to the data it must describe. Some of its modes could characterize shape variations in the distal end of the bone only, which could therefore give absurd values associated to these modes. Since the models are not perfectly fitting the data, it is one of the reason why the results are somewhat worse for these bones. The same apply to the radius, which portion of diaphysis available in the model is far longer than the ones in the NIH

	Mean dist. (1.1) (mm)			Hausdorff dist. (1.3) (mm)		
	mean	max	std	mean	max	std
Radius	0.195	0.304	0.037	1.039	2.526	0.283
Scaphoid	0.137	0.191	0.020	0.670	0.999	0.123
Lunate	0.123	0.191	0.019	0.638	1.013	0.129
Triquetrum	0.123	0.165	0.015	0.622	0.879	0.108
Pisiform	0.117	0.208	0.040	0.575	1.533	0.207
Trapezoid	0.144	0.305	0.039	0.744	1.320	0.195
Trapezium	0.152	0.197	0.019	0.766	1.328	0.155
Capitate	0.173	0.236	0.022	0.908	1.409	0.158
Hamate	0.167	0.250	0.027	0.910	1.583	0.198
Metac. 1	0.139	0.211	0.030	0.710	1.293	0.152
Metac. 2	0.175	0.227	0.024	0.996	2.599	0.292
Metac. 3	0.151	0.202	0.023	0.783	1.214	0.179
Metac. 4	0.133	0.182	0.017	0.690	1.222	0.142
Metac. 5	0.121	0.165	0.017	0.611	0.905	0.127

Table 3.6: Distances between the NIH database meshes and the registered SSMs. Both mean and Hausdorff distances (1.1) and (1.3) are computed, the results are in mm.

database radii. We could imagine to learn the models only for the length of the bone visible in the target mesh. The model would therefore be more adapted. However, in exchange of a model less customized to the target shapes, we gain information about the distal end of the bone that is not initially present in the database. The models bring additional knowledge.

Projection along the normals towards the target meshes

As previously analyzed, the deformed SSMs capture the global shapes of the bones, but miss details. If we want to enrich our data by mixing both NIH and CMC database, we need to fully trust the shapes characterized by the corresponding meshes. Therefore the shapes describing the NIH bones were refined by projecting the vertices towards the target surface, as previously done with the CMC data.

In Table 3.7, the distances between target bones and final meshes are presented. The mean distances between the shapes are smaller than 0.035 mm for all bones. This is largely below the initial precision of the data. The Hausdorff distances are included in range [0.174; 0.295] mm with highest values up to 0.565 mm. The highest distances between vertices and the paired surface are a little higher than the original precision of the data. However, these distances are small nonetheless, half a millimeter at worst, and involve a few vertices at max. The data can be trusted to be used instead of the initial meshes.

	Mean dist. (1.1) (mm)			Hausdorff dist. (1.3) (mm)		
	mean	max	std	mean	max	std
Radius	0.015	0.019	0.002	0.287	0.565	0.096
Scaphoid	0.020	0.025	0.002	0.221	0.458	0.067
Lunate	0.018	0.021	0.001	0.199	0.315	0.047
Triquetrum	0.023	0.028	0.002	0.230	0.347	0.047
Pisiform	0.019	0.024	0.002	0.185	0.359	0.050
Trapezoid	0.020	0.025	0.002	0.255	0.517	0.081
Trapezium	0.029	0.035	0.003	0.295	0.533	0.071
Capitate	0.019	0.023	0.002	0.222	0.362	0.048
Hamate	0.022	0.028	0.002	0.283	0.431	0.069
Metac. 1	0.013	0.019	0.002	0.174	0.423	0.071
Metac. 2	0.018	0.024	0.003	0.216	0.363	0.062
Metac. 3	0.020	0.030	0.004	0.257	0.417	0.067
Metac. 4	0.020	0.031	0.004	0.208	0.360	0.058
Metac. 5	0.018	0.029	0.003	0.177	0.340	0.049

Table 3.7: Distances between the NIH database meshes and the final resulting meshes. Both mean and Hausdorff distances (1.1) and (1.3) are computed, the results are in mm.

3.3.3 Discussion

In this section, by using the statistical shape models constructed based on the CMC database, we have been able to reparameterize a second database and map it to be in dense correspondence with the first one. We have proven that the shapes of the raw meshes and the final projected ones are very similar and can be used instead of each other. We have not tested the quality of the correspondence between the vertices. However, the meshes were constructed by deformation of statistical shape models following their principal modes. By construction, they are in dense correspondence. It should also be noted that during the registration of the SSMs of complete bones to the only proximal end of these bones, we added information about the distal end of the metacarpals that is absent from the initial data. However, during the projection along the normal step, only vertices having close neighbors were projected. The parts with no initial information (distal end of the metacarpals, proximal end of the radii) could obviously not be refined. This step loses the extra knowledge brought by the former process. In the case where this info would be needed, the meshes output by the SSMs registration have to be used.

Since the SSMs were able to register properly the target meshes, it proves that they are not too specific to the training set. An additional step of projection along the normals of the vertices towards the target surface was used to refine the results. The final shapes are very close to the target ones, the average Hausdorff distance is below 0.3 mm. We can use them instead of the original meshes. Additionally, by construction, the correspondence is guaranteed, the NIH database is now in correspondence with the CMC database. In future studies it will enable the use of all subjects from both

databases, which doubles the number of wrists considered. Issues had to be faced about the metacarpals and radii bones due to a variable length of bones visible in the NIH database, while longer portions were encoded in the SSMs.

The two first sections of this chapter are dedicated to the construction of statistical models, and their registration to 3D shapes. This is mostly aimed at testing the quality of the models before using them for registration to images. In the following section, a completely different domain of application is proposed: biomechanics and definition of system of coordinates for joint movement measurement.

3.4 Anatomical Joint Coordinate Systems

In this section, we are interested in a completely different application than the previous ones, though it is also aimed at validating the correspondence relations quality of the generated meshes $M_{R,\{b,i\}}$. We propose the computation of a joint coordinate system for the trapeziometacarpal (TMC) joint. Joint coordinate systems are a common tool for the analysis of joint kinematics. They are composed of two coordinate systems, one attached to each bone of the joint. The description of a motion is based on the rigid movement of the distal bone with respect to the proximal one. We are interested in the TMC joint, the articulation situated at the base of the thumb, connecting the trapezium and the 1st metacarpal, as shown in Fig. 1.4a. But we argue that once the method has been proven reliable for this joint, it can naturally be transferred to any other wrist articulation.

The computation of anatomical coordinate systems offers a dual benefit for our work: our method is completely based on the correspondence relations between the meshes $M_{W,\{b,i\}}$ previously computed. The quality of the results fully depends on the quality of the corresponding points locations. We prove that we get equivalent results to another analytical specialized approach, we therefore consider it an evidence that the corresponding meshes are to be trusted. Additionally, our method is general and naturally functional for any other joint. We illustrate that the database that has been put in correspondence can have many applications in various domains. While in the previous sections we were focused on shape models for 3D shape registration, we are now concerned with a biomechanical utilization.

3.4.1 State of the art

The unique versatility of the human hand is due to its opposable thumb, essential for dexterity as well as for effective handling [JL06]. These skills rely on the thumb's large range of motion [CLCL81], enabled mostly by the trapeziometacarpal joint. This articulation is also one of the joints the most affected by osteoarthritis [MvdWN⁺10], which can prove to be disabling in everyday life. For these reasons, it is important to study the thumb and the TMC joint. Several previous works have addressed the TMC joint kinematics ([HRG⁺14], [CHM⁺15], [KOT⁺18]). It is an intricate joint, composed of saddle-shaped articular surfaces, as shown in Fig. 1.4b. The two main mechanical axes for extension-flexion and abduction-adduction are nonorthogonal and nonintersecting ([HBM⁺92], [CHM⁺15]).

Studies of joint motion require the definition of geometrical reference systems in order to describe the bones kinematics. A strong condition to define such a system is the necessity of reproducibility. Multiple reference systems for the TMC have been proposed in the literature, as more appropriate systems allow to be more precise in the kinematics description. In particular, axes parallel to the direction of movement are ideal, though they are also required to be easily reproducible.

Cooney et al. [CLCL81] were among the first ones to propose a joint reference system for the TMC. The definition of the system is based on the location of anatomical landmarks identified during a cadaver study. It is composed of a fixed coordinate system

on the trapezium and a moving one on the 1st metacarpal. In [WC95], the International Society of Biomechanics (ISB) issued global recommendations on the definition of joint coordinate systems. In [WVdHV⁺05] the ISB proposed system definitions for the joints of the human upper body, among which the wrist and the TMC joint. The axes of the carpal bones are to be parallel with the ones of the radius. The TMC joint coordinate system is defined separately: it is to be the same as the one proposed by Cooney et al [CLCL81], but the axes order is changed.

Cheze et al. [CDC⁺09] refined the ISB system, their axes becoming more coherent with the thumb main degrees of freedom. However their joint reference systems are still based on anatomical landmarks and are thus subjected to variability for their identification. Variability due to landmark identification was studied by Della Croce et al. [DCLCC05]. They addressed the errors made through the selection of landmarks and reported their effects on the reliability and interpretation of joint kinematics. They advise for the use of more robust methods, based on automatic image processing for instance.

Coburn et al. [CUC07] introduced automatically computed coordinates systems for all wrist bones, based on the bones inertial axis arranged in order of ascending inertial magnitude. While easily reproducible, these axis are dependent on the bones global shape, and might be subjects to variations on the axis directions across wrists. Typically, a change of shape away from a joint surface may influence the location of the axes, making them less representative of the joint morphology. These axis also do not follow the ISB recommendations [WC95].

The latest proposal for TMC joint coordinate system computation is a semi-automated method introduced by Halilaj et al. [HRG⁺13]. It is based on the saddle-shaped articular geometry of the TMC joint (Fig. 1.4b). The articular surfaces of the trapezium and 1st metacarpal are manually selected, then fit with fifth order polynomial surfaces. Using the approximation, the principal directions of curvature of the articular surfaces are computed. The coordinate systems origins are the two saddle points, one on each bone. The axis are oriented along the principal directions of curvature of the saddles. The polynomial approximation and the definition of the axis from the principal directions of curvature make the method very specific to local geometry and the saddle-shaped articulation. At the same time, it has been proven that the actual kinematic rotation axis for extension-flexion and for abduction-adduction movements are not always the main directions of curvature of the saddle ([HBM⁺92], [CHM⁺15]).

We propose an alternative approach of axis computation based on correspondence between meshes. The joint coordinate system is the one defined by Halilaj et al. [HRG⁺13], based on the geometry of the articular surfaces of the articulation. We show that similar performances as [HRG⁺13] are achieved for the TMC joint, while having some additional benefit. Typically, the approach has the advantage of being easily adapted to any other system definition on any bone. No limitations to inertial description or local surface approximation allows definition of truly mechanically meaningful coordinates systems. However, we focus on the TMC joint because a comparison can be drawn with the proven approach of [HRG⁺13]. We evaluate the anatomical relevance

of the correspondence mapping method for the TMC joint thanks to a comparison to [HRG⁺13].

3.4.2 Coordinate System Computation

One of the key condition for joint coordinate systems definition is the reproducibility. It is therefore expected that if a system is defined for one instance of a shape class, we should be able to define the anatomically corresponding system on all other instances. Previous methods were either based on landmarks [CLCL81, WVdHV⁺05], but it is a source of variability [DCLCC05], or based on analytical analysis of the shapes [HRG⁺13]. Our method reproducibility capacity rests on correspondence between shapes.

We work with the meshes $M_{W,\{b,i\}}$, for which we have already computed correspondence relations (Chap. 2). They are such that each k^{th} vertex of bone b mesh is localized on the same anatomical point of the class across the instances (Sec. 1.4.4). Our method expects at least one instance of a coordinate system to be known originally. Then the example(s) is(are) transferred to all other instances:

The *origin of the system* is a point on the shape surface. It is either a vertex of the mesh, or a point of one of the mesh faces. In the case of a unique example, if the origin point is a vertex on the example shape, then the same vertex is the origin of the systems for all instances. It stems from the mesh correspondence properties that they are anatomically equivalent. If the example origin point is on one of the faces, its relative position on this face is computed. All origins are then located in the same position of this face, relatively to the face vertices. In the case of multiple examples, we expect the origins to be either all on the same face, or at least to be on neighboring faces. Otherwise, it would mean that the examples are already anatomically dissimilar. Let t_R be the triangular face on which the most centers are. t_R defines for each mesh a plane onto which the example centers are projected, the projection coordinates being expressed relatively to t_R vertices. The mean projected coordinates determine the coordinate system's center relatively to t_R vertices, and can be computed for every other database subjects.

The *directions of the system* can be computed based on various properties. It can either rest on the correspondence property of the meshes, similarly to the origin definition. The directions are expressed relatively to the plane defined by the face the origin belongs to. These orientations are copied for all other coordinate systems. In the case of multiple original examples, the average orientation is transferred. Or their computation can more generally rely on global properties of 3D meshes. For instance, Halilaj et al have to approximate the shape of the articulation surface to compute the principal directions of curvature. Yet curvature tensors could also be estimated from the mesh surface ([CSM03]) to compute the principal directions of curvature, once the saddle point has been defined.

Our method requires no other knowledge than at least one example of a system, when the database is in correspondence. Such an example can be algorithmically computed or be given by a user. The definition is free of a mathematical or algorithmic description that must work in all cases, and is independent of landmarks. It can therefore be customized to match as well as possible the actual biomechanical axis of rotation,

which are not exactly the main directions of curvature of the articulation surface in the case of the TMC joint. The results can be improved by inputting multiple examples, to limit the potential errors made both during the definition (external to our method) and the transfer phases. It is therefore recommended to define numerous example systems, though one is theoretically enough.

3.4.3 Comparison with Halilaj's results

In [HRG⁺13], Halilaj et al. introduced a joint coordinate system for the TMC articulation. It is composed of two coordinate systems called Segment Coordinate Systems (SCS) defined on the trapezium (TPM) and the first metacarpal (MC1) bones. We compare the results of the SCS computation using their analytic procedure (that we call A-SCS) with our own method, based on mesh coherence across the subjects (named M-SCS).

To test our method, annotated saddle points were needed to learn the average location. We have used the system of coordinates computed with Halilaj et al. method for 15 randomly chosen subjects for both articular surfaces of the TPM and MC1 as training set. From these examples, we estimated the M-SCS locations for all database meshes. Multiple options were viable for the directions computation. However, we are mostly interested in the evaluation of the correspondence quality between the meshes, and therefore chose to rely on the correspondence property for the axis calculation. Similarly to the system location, the system orientation is computed based on the training set of 15 wrists computed with Halilaj's method. The orientations of the example SCSs relatively to the mesh surface are transferred to the other subjects.

As in [HRG⁺13], the evaluation is made with respect to the steadiness of the M-SCS systems origins and orientations across the database. The database bones were all affinely aligned using ICP. Inter-subject variability is defined as the difference between individual M-SCS's locations and the average one, as well as the difference of orientation between each axis and the average one. Additionally to Halilaj's paper, we measure a global angle between each individual system and the average one. It provides more information than 3 rotation angles around the x , y and z axis. This global angle is the angle of rotation around the helical axis describing the relative motion between a system and the average one. The SCS systems using the analytical method were also computed, and we compare the results of the two approaches. The evaluation of the systems steadiness is not a perfect measure to validate the accuracy of the coordinate systems. Part of the instability is due to the differences of shape of the bones and not to the method. However no ideal error metric exists to separate the shape variability from the method variability. We propose a comparison of two methods on the same shapes.

The difference of location and orientation between individual and average M-SCS systems are presented in Table 3.8a. Globally both location and orientation results are slightly better for TPM bones than for MC1 ones. The mean location distances are of 0.59 mm for TPMs with a maximum value of 1.15 mm, and for MC1s, the mean distance is 0.76 mm with a maximum of 1.43 mm. The global angles between the systems orientations are 4.3° on average for TPM bones, the highest difference being 11.7° and those values are 6.1° and 11.5° for the MC1 bones.

Those values are compared with the ones obtained by computing A-SCS systems on our database. Both systems give results in the same order of magnitude. M-SCS gets slightly better results for the TPM bone, especially for the origin locations, with a mean error of 0.59 mm versus a mean error of 0.81 mm using A-SCS. On the opposite A-SCS get slightly better results for the MC1 origin locations. However the orientation are steadier for both bones using the correspondence based method, while the magnitude of errors remain the same.

An example of an SCS system can be observed in Fig. 3.7 for both TPM and MC1 bones.

		Location (mm)	Orientation (°)			
			X axis	Y axis	Z axis	Global angle
TPM	mean	0.585	3.477	3.533	3.241	4.327
	max	1.149	7.298	11.714	9.128	11.673
	std	0.237	1.647	2.056	1.777	1.961
MC1	mean	0.762	4.901	5.068	4.378	6.109
	max	1.434	8.856	11.509	9.072	11.541
	std	0.299	1.979	2.354	2.451	2.192

(a) SCS steadiness when computed with our correspondence-based method

		Location (mm)	Orientation (°)			
			X axis	Y axis	Z axis	Global angle
TPM	mean	0.814	6.293	5.353	4.864	6.987
	max	1.463	16.189	16.589	11.456	17.086
	std	0.315	3.455	3.104	2.570	3.347
MC1	mean	0.706	5.747	5.121	6.315	7.280
	max	1.614	10.773	10.468	11.091	12.425
	std	0.334	2.885	2.351	2.932	2.782

(b) SCS steadiness when computed with [HRG+13] analytical method

Table 3.8: Comparison between the analytical method of [HRG+13] and ours : study of the inter-subject variability of the joint coordinate systems location and orientation for the TPM and MC1 bones.

3.4.4 Discussion

We have proposed a method that is able to reproduce coordinate systems for all bones of our database when one or a few examples have been defined. The method rests on the correspondence relations between the meshes. We have tested it using a joint coordinate system definition given in [HRG+13] for the TMC joint. Systems based on this definition were computed using both their analytical method and our correspondence-based one. We prove that the steadiness of the systems are in the same

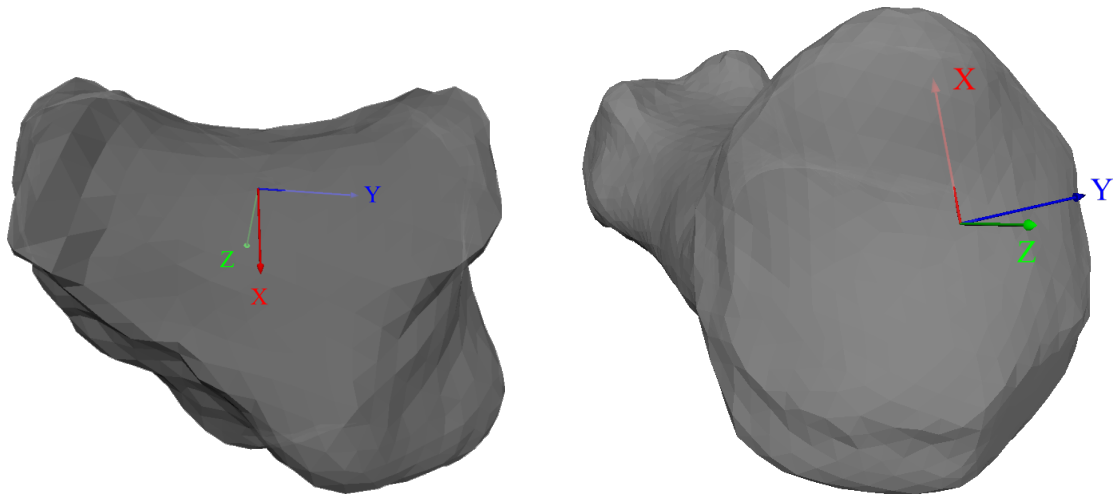


Figure 3.7: Examples of coordinates systems defined by [HRG⁺13] and computed with our method, for the TPM (left) and MC1 (right) bones of a subject.

range of values using both approaches, even slightly better for our procedure. Our method is completely based on the quality of the correspondence relations previously created, and gets equal results than another very specialized method. We deduce that the correspondence between meshes is to be trusted.

We have equivalent results than a local specialized method that is fit to compute one definition of coordinate systems for one articulation only. Yet our approach uses no prerequisite that makes it specific neither to this joint nor to this particular system definition based on principal curvatures. Any system described by a user on one or a few examples can be reproduced on any bone, for instance systems that are better adapted to the TMC joint. It has indeed been proven that the principal directions of curvature of the saddle-shaped surfaces of the TMC joint are not the actual kinematic rotation axis ([HBM⁺92], [CHM⁺15]). Any other wrist joint can be examined as well. We could imagine for example to define multiple joint coordinate systems to study the entire articular chain of the thumb in the wrist, including the radius and the scaphoid as suggested by [DDK⁺17].

This mapping of bones through dense correspondence can also have other applications. For example the location of the ligaments attachment to bones can naturally be transferred from one subject to all other. Simulations of tendons adapting to various shapes of wrist bones could be imagine as a possible application.

3.5 Conclusion

In this chapter we have proposed different applications of the database that was previously put in dense correspondence: the meshes can be used to create statistical models which can in turn be used to compute correspondence for new instances of the shapes, even when the latter are incomplete. The correspondence relations can also be used to transfer landmarks or coordinate systems from one or a few examples to all other occurrences of the database.

First we have studied the accuracy level that could be reached by statistical models for 3D shape registration. PCA-based models representing one bone have proven to be able to reach a good similarity with the target mesh, the mean error is below the accuracy of the original data. They have been further tested on a new database and enabled to reparameterize the latter to be in correspondence with the meshes of the first database. We have chosen to use an additional step of projection along the normals of the optimized models towards the target meshes. It was aimed at warping as well as possible the NIH meshes in order to use them later as training shapes with certainty that they faithfully represent the bones.

PCA-based statistical models were defined both for all wrist bones at once and for each bone separately. While the individual models have been shown to reach a good level of accuracy for 3D shape registration, the global model wasn't precise enough for the whole wrist registration. It is interesting to consider all bones at once, as they are really close from each other and the shape of one bone necessarily influences its neighbors shapes. However, the model has proved to need more principal modes than were available from the training set formed with the CMC database. Now that the NIH database is in correspondence with the CMC one, more data are available, a possible perspective would be to compute a new model for the whole wrist using both databases together as prior information. In addition to a larger span of shapes learned, more modes would be available, which could enable the model to reach a higher level of registration accuracy.

A second type of models were used: Gaussian Processes Morphable Models. Shapes are modeled as vertex deformations undergone by the mean shape. These models are promising: depending on the covariance function chosen, they can have various combined properties, and are not necessarily linear. Moreover, they adapt to posterior information, which allows human intervention in the results. A completely user-based registration approach was tested and was successful, really high similarity levels between shapes that can be reached as long as enough points are given by the user. However, we have concluded that in practice the algorithm cannot be used as is, it would require too many points hence too much time from a qualified person. In a second phase an all-automatic registration method based on a parametric approximation was tested, and achieved good results. They were not as good as the SSMs ones, but lack of time prevented us from optimizing the model parameters, and we believe that better similarity can be reached. We believe GPMMs to be promising and next steps would be to further test the model and maybe mix the all-automatic and all-user based methods.

Statistical models can have various utilizations. For example they can be employed for a quantitative analysis of bone shapes and allow the identification of phenotypes [CLW⁺14]. They are often used as prior knowledge for image segmentation [CGHM12, ARJ⁺14]: the models are being registered to the 2D or 3D images and provide simultaneously a segmentation of the object in the image and a 3D representation of it. Such applications are dependent on the quality of the model and its capacity to represent new shapes. Now that it has been assessed that the SSMs are quite precise, these applications could be implemented.

Finally a biomechanics oriented application was proposed. We have shown that based on the correspondence relations previously established, landmarks and orientations can be easily transferred from one or a few instances of the database to all others. We have proven that the reliability of our method is similar to another method proposed in the literature. This method happens to be to the best of our knowledge the only automatic method of joint coordinate system definition for the TMC joint, except for the method proposed in [CUC07] which does not follow the ISB prescriptions. Our method is less specialized than the one it was compared to and can therefore be employed on any other joint of the wrist. It can also be used for any other application requiring the transfer of points to other instances of a same shape. Additionally the reliability of the method was a proof of the quality of the correspondence relations defined in the previous chapter.

This chapter and the last one's purpose was to study the wrist bone shapes. In the next chapter we will present the work we have done about wrist movement. The ultimate goal is to be able to take the influence of wrist bones shapes into account when the movement is modeled.

CHAP. 4

STATISTICAL MOVEMENT MODEL

Contents

4.1	Introduction	122
4.2	State-of-the-art	123
4.3	Parametric model of the wrist motion	125
4.3.1	Multiple regression analysis	125
4.3.2	Parametric model	126
4.3.3	Model application	126
4.3.4	Model validation	127
4.4	Conclusion	134

4.1 Introduction

In this chapter, we are interested in the modeling of the wrist motion. More particularly, we observed that very few models of the wrist movement were proposed in the literature, and all of them are PCA-based. Similarly to the observation that lead to the GPMMs, we note that such models can only lead to fully automatic utilizations. The PCA-based modes are likely to blend multiple simple transformations such as flexion or radial deviation at once, which makes them unusable for a human user. We propose to use linear regression to build a parametric model described by meaningful predictors: the wrist and thumb degrees of freedom.

Human interaction with a model could have various applications. For instance a diagnosis tool could be composed of a model whose parameters are interpretable and easily measurable. An individual could be easily lead to take a few characterized poses, and the scans could be compared to the theoretical healthy wrist pattern defined by the model. An unhealthy wrist bone pattern could happen to be closely approximated by an all-automatic model, while the actual pose characteristics are different, which would be avoided with a manual model.

At first we present a brief state-of-the-art of existing works about carpal bones movement modeling. Then we introduce the mathematical theory behind the model, that is multiple regression analysis. Using the CMC database, we present a parametric model based on five predictors. We validate the definition of these parameters: they should be correlated to the poses and the model should have predictable changes when their values are modified. We test the generalization capacity of the model with the poses available. In the conclusion we discuss the need of another more complete database to build an exhaustive model and further test its capacities. The exploratory study presented in this chapter can integrate more data and suggests that the new proposed approach is a promising alternative to efficiently model carpal bones movement.

4.2 State-of-the-art

For some simple joints, such as the knee, *in vivo* measures can be taken using non-invasive surface markers placed on the skin, and it can be deduced what happens at the bone level of the joint. It is not the case for the wrist due to its complex bone structure. Therefore studies of wrist articulations for carpal bones kinematics understanding have rested for a long time on invasive *in vitro* examinations. The analysis of cadaveric kinematics typically combines markers fixed on the bones and medical imaging such as biplanar radiographs like in [RCIA⁺88, HGEA⁺91]. Non-invasive *in vivo* studies were performed such as in [PWMG85], in which wrist kinematics are being characterized using an electrogoniometer to measure the articulation degrees of freedom and their ranges. However the acquired information are insufficient to characterize the inside bone kinematics.

Non-invasive *in vivo* analysis of the carpal bones were made possible with the utilization of 3D CT scans or MRI instead of biplanar radiographs. It enabled the analysis of images with real 3 dimensions without overlapping shadows and unreliable angle measurements [BHL⁺91]. At first they were mostly used for carpal bone geometry analysis [BHL⁺88, PEVB95, VHE⁺93], but also normal carpal orientation and position characterization [BHL⁺91]. The first non-invasive methods to quantify *in vivo* 3D wrist bones kinematics was proposed by Crisco et al. in [CMW99]. They were inspired by similar existing methods for large joints such as the knee, that could not directly be applied to the wrist due to its complex small bones and narrow articular spaces. The method proposed rests on the imaging of the joint at multiple positions using CT scans. The bones are segmented based on a threshold value determined from the image histogram, manual intervention may be required to correct some results. An algorithm considering the centroid of each contour is used to label the bones. 3D motion is described by a rotation matrix and a translation vector in the space. Other studies later analyzed *in vivo* 3D kinematics of carpal bones including a series of papers by Moojen, Snel et al. [SVM⁺00, MSR⁺01, MSR⁺02a, MSR⁺02b] and a comparison of their results with the literature [MSR⁺03]. Foumani et al. for their part compared carpal bone kinematics results during dynamic motion and step-wise static poses, and concluded that no significant difference exists [FSJ⁺09]. These analysis mostly rest on deformable models for prior shape information to segment the images at various poses.

The thumb kinematics at wrist level, that is mostly the TMC joint kinematics, are often studied separately from the wrist kinematics. Due to the importance of the thumb for every day life and the effects of osteoarthritis on its mobility, the characterization of healthy motion is important. Late works on thumb kinematics include a study of Crisco et al. [CHM⁺15] to characterize the TMC joint during flexion-extension and adduction-abduction of the thumb. D'Agostino et al. proposed a similar study for the same thumb poses, but including the analysis of the whole chain of movement of the thumb in the wrist, including the radius and the scaphoid in addition to the trapezium and the 1st metacarpal [DDK⁺17].

When the kinematics of the carpal bones have been quantified, it is interesting to be able to model healthy motion. Concerning the wrist kinematics, Chen et al. [CGHM11, CGHM12] and Anas et al. [ARJ⁺14, ARS⁺16] propose two models, both

based on a principal component analysis of the rotations and translations of the bones between poses, the radius being the unmoving reference. Chen et al. propose an inter-subjects model, based on a PCA on all poses of all wrists in [CGHM11, CGHM12] which they use to infer carpal kinematics from single view fluoroscopic sequences. Anas et al. construct two models from the translations and rotations of the carpal bones at various poses of multiple subjects: one intra-subject model represents all possible poses of one person, while an inter-subject model describes the differences for one pose between the different wrists [ARJ⁺14, ARS⁺16]. The combination of these two models is used for the segmentation of new images at any wrist pose. Concerning the thumb kinematics at the wrist level, Crisco et al. [CPHM15] proposed a mathematical model describing the envelope of physiological motion of the TMC joint.

The few existing parametric models are based on a PCA, the principal components can describe any combination of motion between the different poses, which make them hard to interpret. We want to create a model of both wrist and thumb motion, adjustable with predictor variables that are observable and make sense for a human user. Therefore we propose a linear model whose parameters are the degrees of flexion-extension and adduction-abduction of the wrist and of the thumb. Additionally, we add a parameter describing whether the wrist is loaded or not.

4.3 Parametric model of the wrist motion

We aim at creating a parametric model of the wrist motion, such that the parameters are interpretable by a human user. The idea is to create an example of a healthy wrist, whose bones follow a standard motion. It can be used to help diagnose unhealthy wrist patterns, by comparison between the healthy model movement and the one observed from an individual. Such a model is based on the hypothesis that continuous movement can be inferred from some poses, which has already been discussed in [FSJ⁺09]. The necessity of interpretable parameters comes from the utilization of the model for diagnosis: if the parameters describe the angles of the wrist and thumb in flexion-extension and abduction-adduction, it is really easy for an individual to take a certain wrist pose and report the parameters into the model for comparison.

We base our method on a simple multiple regression analysis. First we briefly present the mathematical background of the model, then we describe how our model was constructed and the results obtained.

4.3.1 Multiple regression analysis

Multiple regression analysis is a supervised learning technique, whose purpose is to determine the relationship between some predictor (independent) variables \mathbf{x} and a dependent variable \mathbf{y} .

$$\mathbf{y} \approx f(\mathbf{x}, \beta) \quad (4.1)$$

We are only interested in linear regression, that is the dependent variables can be described as a linear combination of the regression parameters β . It is not necessarily a linear combination of the predictors and non linear functions Φ of each predictor can be used, such as any degree polynomial function or any kernel-based function [ZH17]. The major advantage of linear regression is that it can be efficiently solved using least-squares. In linear regression, equation (4.1) for p predictor variables and r dependent variables can be written as :

$$\mathbf{y}_k = \beta_{1,k}\Phi_1(x_1) + \beta_{2,k}\Phi_2(x_2) + \dots + \beta_{p,k}\Phi_p(x_p) \quad (4.2)$$

\mathbf{y}_k is the k^{th} dependent variable, $k \in \{1, \dots, r\}$. The parameters $\beta_{j,k}$ are computed using the training set, which is such that both observed predictors $\hat{\mathbf{x}}$ and the associated observed $\hat{\mathbf{y}}$ are known. Let Φ be the matrix such that $\Phi_{i,j} = \Phi_j(\widehat{x}_{i,j})$, $\widehat{x}_{i,j}$ is the i^{th} observation of the j^{th} predictor. In matrix notation,

$$Y = \Phi B \quad (4.3)$$

If there are n observations, p predictors and r dependent variables, then Φ is $n \times p$, Y is $n \times r$ and B is $p \times r$. The regression parameters are computed using:

$$B = (\Phi^t \Phi)^{-1} \Phi^t Y \quad (4.4)$$

A regularization parameter λ can be added to avoid overfitting:

$$B = (\Phi^t \Phi + \lambda I)^{-1} \Phi^t Y \quad (4.5)$$

In the next subsection, we describe how multiple regression analysis is used to model the wrist pose of all bones.

4.3.2 Parametric model

We want to parameterize the pose of a wrist with interpretable parameters, we define 5 of them: 4 parameters characterize the degrees of freedom of the thumb and wrist articulations: the degree of rotation in *flexion-extension of the wrist*, the degree of rotation in *radial-ulnar deviation of the wrist*, the degrees of rotation in *flexion-extension* and *abduction-adduction of the thumb*. A last boolean parameter describes whether the pose is *loaded*, that is if the individual puts some force in the pose or not. The parameters describe all degrees of freedom of the joints we aim at modeling. They should therefore be able to capture the whole range of possible poses. Additionally, they are easily measurable, both for a living human being, with a goniometer for instance, and for a computer wrist pose characterized by 3D meshes of the bones, as detailed in Table 4.1. It only requires to know the neutral pose, since the parameters are expressed relatively to it.

In both NIH and CMC databases, a pose is described as a list of matrices defining for each bone the rigid transformations from the neutral pose to the current one. We have to estimate the values of the model parameters from the wrist bones movements. The angles of rotation of the MC1 and MC3 bones are used to characterize respectively the thumb and the wrist angles. A system of coordinates is defined on the radius, as described in Sec. 2.2.2.c. A system of coordinates parallel to the radius one at neutral pose is defined on the MC3. The *global wrist angles* are calculated as the angles of the MC3 with respect to the radius [PNV⁺98], as listed in Table 4.1. For example, rotation about the Y axis describes the angle of flexion-extension, if the angle is positive, the wrist is in flexion, if negative the wrist is in extension. The rotations values are 0 when the wrist is in its neutral pose. For the description of the *thumb angle*, the movement of the MC1 relatively to the TPM is used. A joint coordinate system on the TMC joint is computed, its definition is the one described in Sec. 3.4, our method based on the correspondence property is applied. The thumb angles (Table 4.1) are described as defined in [HRG⁺13]. Once again, the angles are considered to be 0 at neutral pose.

4.3.3 Model application

We are interested in working both with wrist and thumb movements, therefore we work with the CMC database. The poses mostly are about thumb movement: the 10 poses, in addition to the neutral one are: thumb flexion and extension; thumb adduction and abduction; pinch, jar grasp and jar twist with and without load (Table 1.1). However, we observe a residual movement of the wrist, which is not completely motionless between poses. This residual movement consists mostly in extension and radial-ulnar deviation. It enables to consider that both wrist and thumb movements can

Parameter	Movement of	Relatively to	Rotation axis
Wrist flexion-extension	MC3	RAD	Y_{RAD}
Wrist deviation	MC3	RAD	X_{RAD}
Thumb flexion-extension	MC1	TPM	Z_{TPM}
Thumb abduction-adduction	MC1	TPM	X_{MC1}

Table 4.1: The parameters values are the angles of rotation of a bone relatively to another one, around particular axis of systems of coordinates defined in Sec. 4.3.2.

be modeled. The presence of residual wrist movement was confirmed using a PCA on the movement data. The NIH database for its part is composed of poses of the wrist movement, but thumb movements are absent.

It has been proved for example that two types of lunate exist, and the type of the bone influences the kinematics of the neighboring bones [NBP⁺00, GBM07, BCM⁺15]. Therefore each subject is considered separately, one model is created for each person. Ideally a future model will be able to consider all subjects together, by considering the bones shapes characterized by a statistical shape model as a parameter of the person. The model should be able to adapt the motion modeled to an individual's anatomy. However we have not yet succeeded in creating such a model.

A bone in pose P is characterized by the translation and rotation undergone from its neutral position and orientation to the pose P . It is a vector of size 6: $v = (r_x, r_y, r_z, t_x, t_y, t_z)$. The rotation is measured with Euler angles. One pose is represented by the concatenation of all bone vectors for this pose. It is a vector of size $6B$, with $B = 14$ the number of wrist bones (8 carpals, 5 metacarpals and the radius). The motion space defined by the poses of the data is calculated for one individual at a time, since we expect the motion to be dependent on the person. Using the same notations as in (4.4), $n = 11$ is the number of poses for one individual. $p = 5$ is the number of predictors: they are the interpretable parameters previously defined and calculated using MC1 and MC3 orientations. $r = 84$ is the number of dependent variables, that is to say the description of a pose using the translations and rotations undergone by every bone from the neutral pose. The matrix \mathbf{Y} describes the different poses based on the rotations and translations while the matrix \mathbf{X} , composed of all $x_{i,j}$ represents the same poses using the 5 parameters. At first we have chosen to define all Φ_j as the identity function, though later tests should include other functions, such as radial basis functions.

4.3.4 Model validation

We have chosen five parameters that can be easily measured for a human hand and that make sense for a user. However, it must be verified that they are indeed good parameters for the model. Predictors are supposed to be independent, which is a common assumption in real life for a joint's degrees of freedom. It must also be verified that there is actually a correlation between the angles previously defined and the poses, and that the correlation has the expected effect: if the first parameter, supposed to

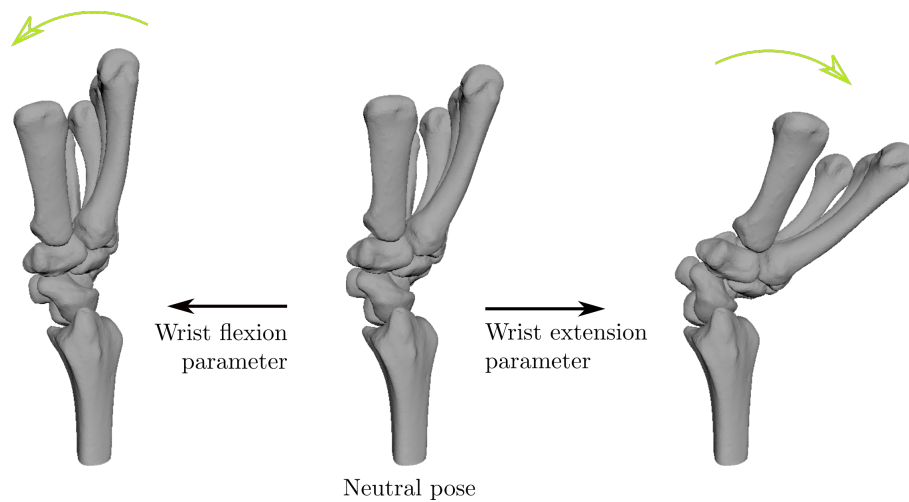


Figure 4.1: Wrist pose variations simulated by the model for the two extreme values of the wrist flexion-extension parameter

characterized the wrist flexion-extension, is modified, then we check that it indeed causes such a wrist movement.

Parameter verification is done by generating poses with all parameters values equal to 0, except for one of them, which is put in turn to its two extreme values. The most extreme wrist flexion value for instance is the higher flexion angle for the modeled individual among the 11 poses of the database. We present the effects of all five parameters for one model of a database's subject: Fig. 4.1 for the wrist flexion-extension; Fig. 4.2 for the wrist radial-ulnar deviation; Fig. 4.3 for the thumb flexion-extension; Fig. 4.4 for the thumb abduction-adduction and in Fig. 4.5 for the boolean *loaded* parameter. We verify that the movement between the two poses generated with the extreme values of the parameters is indeed the expected motion characterized by the parameter.

It can be observed in the figures that the model has globally the expected behaviour: the correct wrist or thumb movement is performed. In Fig. 4.5 the effects of the force parameter are difficult to observe: the carpal bones are slightly drawn closer from each other, on the images only the pisiform displacement is visible, pointed out by arrows. It can also be noted that in Fig. 4.1 the wrist flexion is barely visible. This is due to the absence of wrist flexion in the database poses. We observe a slight correlation between the wrists movements and the thumb ones: when the wrist is moved the thumb undergoes a light shift and the same happens in the other way around. It is hardly observable on the 2D pictures, for it is a very small fluctuation. The wrist and the finger movements are not completely decorrelated: it is the tenodesis effect. Due to the attachment of the finger tendons to the bones, the wrist joint movement influences the finger position [RS10]. It can be observed for example when the wrist is flexed, if the fingers are free they have a tendency to stretch out, while they bend with an extension movement. The correlation observed in the model must be further analyzed with additional data to check if it is completely due to the tenodesis effect, or if a part

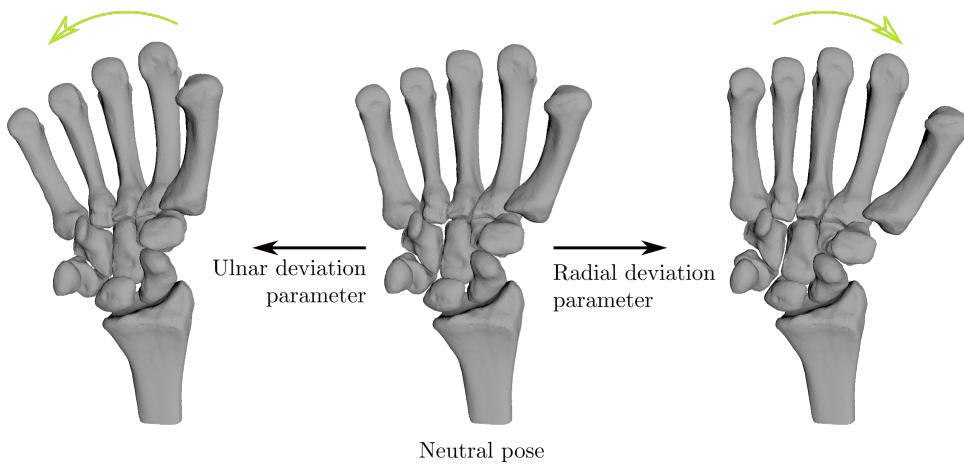


Figure 4.2: Wrist pose variations simulated by the model for the two extreme values of the wrist deviation parameter

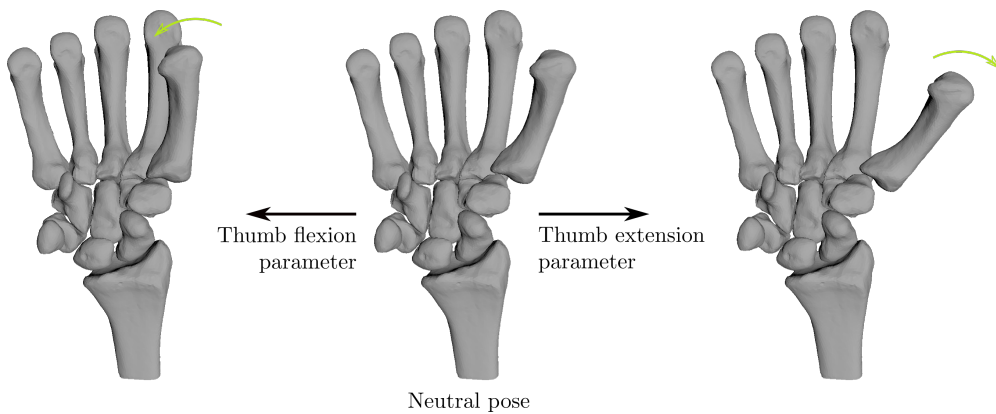


Figure 4.3: Wrist pose variations simulated by the model for the two extreme values of the thumb flexion-extension parameter

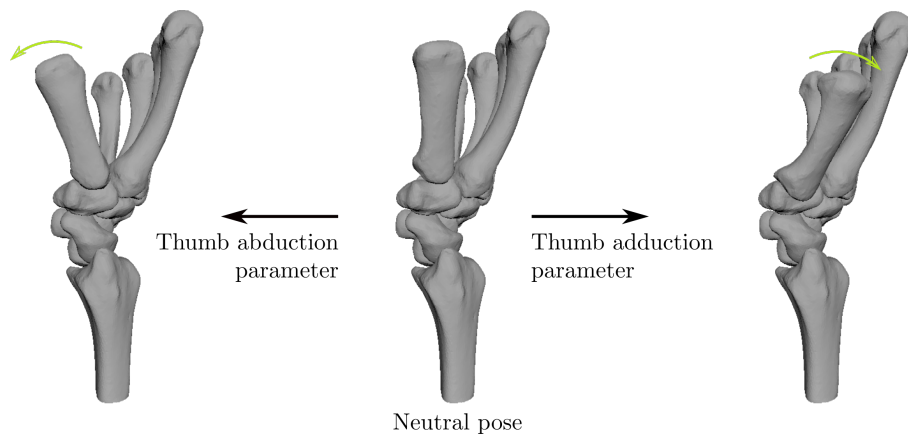


Figure 4.4: Wrist pose variations simulated by the model for the two extreme values of the thumb abduction-adduction parameter

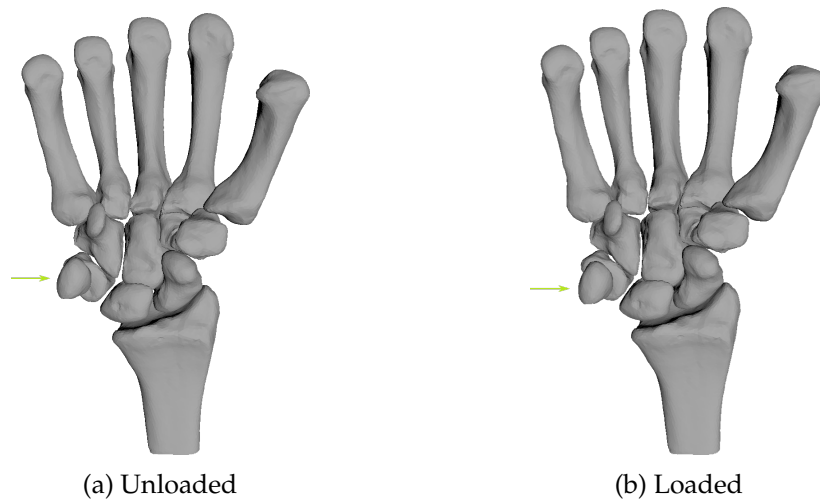


Figure 4.5: Wrist pose variations simulated by the model for the boolean *loaded* parameter

of it originates from the poses learned in the training set, which present no wrist only motion.

Different types of representation of the data were tested: in the example model in Fig. 4.1 to Fig. 4.5 each bone was considered independently of the others. Using hierarchy between the bones was also tried out: the movement of a bone is expressed relatively to the previous one in the chain of articulation. MC1 is dependent on TPM, MC2 depends on the trapezoid, MC3 is related to CAP and finally MC4 and MC5 are linked to HAM. The carpal bones relationships are too complex, we didn't try to create a hierarchy between them. This data representation didn't have much impact on the model and the parameters effects. Different functions Φ_j were also tested including radial basis functions and various values for the regularization parameter λ . We introduce two example models that were used to test the generalization capacity of the model.

Model 1

- $\Phi_j(x_j) = x_j$;
- $\lambda = 0$;
- No hierarchy between the bones

Model 2

- $\Phi_j(x) = \exp\left(-\frac{1}{2} \frac{\|x_j - \bar{x}_j\|^2}{\sigma^2}\right)$; \bar{x}_j is the mean value of the j^{th} predictor over all training observations
- $\sigma = 24.0$
- $\lambda = 0.05$;
- No hierarchy between the bones

The generalization capacity of the model was tested with the two parameterizations presented above. By turn one pose was left out of the training set of all poses for one individual, and using the predictor values, positions and orientations of the bones for the pose were calculated with the model. The values are compared to the experimental values obtained from the poses scans. The average position and orientation errors over all individuals are computed, the bones are considered separately. The difference of orientation is given as a global angle, the angle of rotation around the helical axis describing the motion to go from the computed orientation to the experimental one. The position error is given as a global distance in mm. We present the errors made with Model 1 and Model 2 for 4 bones: for MC1 in Table 4.2, for MC3 in Table X.5, for LUN in Table X.6 and finally for HAM in Table X.7. An example of an experimental and the equivalent calculated pose is presented in Fig. 4.6: the experimental bone positions and orientations are in orange, while the gray bones were calculated with Model 1 in the "Jar, no load" pose.

MC1 Pose	Model 1		Model 2	
	Translation (mm)	Rotation (°)	Translation (mm)	Rotation (°)
Neutral	1.104	1.547	1.151	4.800
Adduction	0.989	0.983	1.709	2.294
Abduction	0.945	0.296	1.652	1.637
Extension	0.884	0.822	1.519	1.886
Flexion	0.840	1.098	1.780	1.349
Pinch, no load	0.851	1.132	1.609	1.189
Pinch, loaded	0.808	0.837	1.514	1.148
Grasp, no load	0.804	0.734	1.448	1.012
Grasp, load	0.770	0.702	1.391	0.547
Jar, no load	0.745	0.682	1.350	0.413
Jar, load	0.731	0.526	1.372	0.126

Table 4.2: Average error over individuals between the experimental orientation and position of the MC1 and the values computed from the predictors, using two linear regression sets of parameters.

In Tables 4.2, X.5, X.6, X.7 are presented the average differences in location and orientation between the experimental poses and the ones calculated with linear regression for two sets of parameters for 4 bones: MC1, MC3, LUN and HAM. These values are hardly interpretable in themselves. In Tables 4.3 and X.8 are given as indications the mean translation and rotation values of the same bones between the neutral pose and all other poses. The errors must be compared relatively to the ranges of rotation and translations the bones undergo during motion.

It must be noted that there are few training poses and leaving one out to test the model necessarily skew the results. Some extreme poses such as the thumb flexion and extension ones should be used to define the space of possible poses. However there are not enough poses to both test the generalization capacity and leave all extreme poses out of the test procedure.

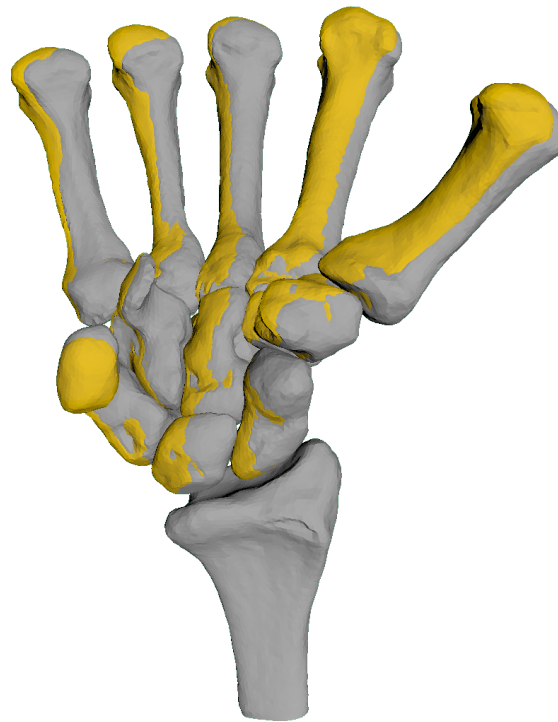


Figure 4.6: Simulation of the "Jar, no load" pose with the Model 1, while the pose was left out of the training set. In orange are the experimental bones as captured in the database, in gray the positions and orientations of the bones computed with a linear regression model, using the predictors values.

Pose	MC1		MC3	
	Translation (mm)	Rotation (°)	Translation (mm)	Rotation (°)
Thumb Adduction	3.18	9.73	0.64	2.23
Thumb Abduction	2.84	13.45	0.60	5.24
Thumb Extension	3.52	29.38	0.73	5.78
Thumb Flexion	3.19	10.78	0.66	5.38
Pinch, no load	2.54	20.61	0.79	7.95
Pinch, loaded	2.15	16.54	1.03	12.00
Grasp, no load	3.90	21.98	1.46	27.60
Grasp, load	6.59	40.11	1.37	37.60
Jar, no load	5.97	31.42	1.81	33.73
Jar, load	3.40	13.33	1.67	22.00

Table 4.3: Average rotation and translation in absolute values over individuals between the neutral pose and the other experimental poses for the MC1 and MC3 bones in the CMC database.

4.4 Conclusion

In this chapter we have presented the work done about wrist motion modeling. A parametric model based on a linear regression analysis is proposed. The parameters were chosen so they make sense to a human user, on the opposite of PCA modes which are likely to blend several meaningful transformations. They were also determined according to the ease with which these values can be measured, both for a real flesh wrist and for a computerized bony one. The degrees of freedom of the modeled joints have been selected to be the parameters, along with a boolean describing if force is put in the pose. Such a model would be useful for diagnosis, to compare a healthy modeled movement and the one of a subject. We have proven that the parameters seem to be acceptable predictors: the model reacts as expected to the changes of value of the parameters. For instance when the predictors supposed to describe the angles between the $MC3$ and the RAD are changed, the global wrist is indeed moved. We have also tested the generalization capacity of the model by measuring the difference between poses computed from the predictors values and the experimental poses as captured by CT scans.

The modeling is promising, however further analysis of the pertinence of such a model would require another database incorporating more poses per individual. Motion of the wrist alone without thumb activity are necessitated for a more complete description of the motion space. Intermediary poses would also be required both to decompose the path between two extreme complementary poses such as flexion and extension, and to further explore combinations of simple movements. Additionally these intermediary poses are necessary to further validate the model by measuring its generalization capacity while using extreme poses to define the space of possible poses. Further testing of the model on a more complete database would also enable optimization of the functions and parameters, and underline the necessity of yet another predictor if one is actually needed. However this preliminary work is interesting, it confirms the feasibility of the method.

We have restricted our model to define the motion space of one wrist at a time, on the opposite of the PCA-based model in [CGHM12]. Something we did not address but is interesting is the influence of bones shapes on the wrist movements. It would be very interesting once a more complete model of the wrist movement is achieved, to analyze similarities and differences of individual motions with respect to the bone shapes, to confirm or disprove this hypothesis. The bone shapes are not the only factors of influence on the carpal wrist motion, the ligaments for instance can also have an impact on the bones displacement patterns. For the moment, the movement model is still uncorrelated to the shape one. However, a future complete model, incorporating all subjects' bone shapes and motion could be computed. It would ideally adapt the modeled motion to the wrist anatomy.

CONCLUSION AND PERSPECTIVES

This thesis focuses on the modeling of the wrist bones shapes. It is part of a field in which few works were conducted and little suitable data were gathered. Reliable modeling can however have many useful applications such as diagnosis help functions or transplant customization. We propose a method to define relations between carpal bone meshes and attach importance to proving the reliability of our results. Statistical models are computed from the data, which provides the properties required for the intended applications. In this conclusion, we will come back over the work accomplished and explore the prospects and potential applications.

We have developed a method to represent wrists such that they are related by correspondence relations between all instances of a bone. It rests on the definition of common templates, that are deformed to match individual bone shapes. As was illustrated in the existing works review, correspondence between shapes is a powerful property, that is required for many applications in different domains. However it cannot be quantified or validated. It makes it difficult to work with, as its quality cannot be proven by direct measures. In this study indirect properties are used to assess correspondence relations quality, including characteristics of the statistical model generated based on the correspondence.

We propose various applications of the meshes previously computed, some of them being additionally useful to validate the correspondence relations: two statistical models, one based on a PCA and one on Gaussian Processes, are introduced. The first statistical model is later used for registering the wrists of a second database, extending the number of corresponding wrists available for later studies. A method for transferring systems of coordinates between individual's wrists is proposed, which can be useful for characterizing joint motion. This method is applied in a first attempt of modeling the wrist kinematics with meaningful predictors. The CMC database does not include enough poses for real applications, but we establish the feasibility as proof of concept.

We detail a method to obtain correspondence between wrist bones, which is a tricky task due to the complex carpal shapes. It is based on the definition of common reference templates that are non-rigidly registered towards the database meshes. We propose a partial validation of the results by proving that the generated reparameterized shapes at least describe the same 3D objects than the original meshes of the database: the average Hausdorff distance between the original database mesh and its equivalent deformed template is below 0.6 mm. We justify that all details are preserved and studying the resulting shapes is equivalent to studying the original ones, no shape information is lost. We attach importance to the simplicity and easy reproducibility of the approach. We didn't implement equivalent methods proposed by other authors to compare the results, and very few comparisons between methods have been proposed in general in the literature. An interesting future work would be to implement and compare all these works.

We propose some possible applications that require correspondence between shapes. We compute a statistical shape model based on a PCA. It is a quite classical application and all wrist shape models in the literature are either based on a PCA or a derivative method. The registration capacities of the model to new 3D shapes are tested. When its reliability is proven, we register it to a second database, which is in turn reparameterized to be in correspondence with the first one. It doubles the number of wrists available. Considering the limited number of individuals some carpal bone shape studies rest on, it would be interesting to verify that the same conclusions are reached with a wider sample group. In a second part, another statistical model is computed, based on Gaussian Processes, which were never previously applied to carpal bones. We are interested in the registration capacities of this model. It indeed offers multiple advantages over the PCA-based model, such as adaptation to posterior user information, and non-linearity. These two properties were tested separately. However a lack of time did not permit to thoroughly test the model possibilities, further analysis are required. We would also be very interested in combining the two methods proposed, in a user interactive registration. A third application is intended for biomechanical applications. Resting on the correspondence relations previously defined, we are able to transfer systems of coordinates, and more generally points and directions from a few example to all other individuals. Such systems are used in the analysis of joints motion, and are required to be reproducible, which usually limits the possible definitions to mathematical or anatomical remarkable points. However our method is not restricted to such landmarks, thanks to the correspondence relations previously created, and could be used to define optimal systems for the joints.

Finally the focus is on modeling of wrist motion. The few existing models in the literature are all PCA-based, and are not interfaced with explicit articular degrees of freedom. We have evaluated a direct application of linear regression to our mesh models, using meaningful parameters such as the wrist and the thumb flexion-extension angles. The 3D representation of wrist posture can be directly adjusted with these angular positions. However our validations are limited and the approach need to be tested with extended CT scan data to include intermediary poses and more complete finger movements. Our approach is applied to each individual wrist representation

and introduces the possibility to study motions with respect to the bone shapes, by comparison of individuals.

This conclusion describes the main lines of the work realized in this thesis. We have proposed various leads to continue what was done. However, more global perspectives could also be considered. To the best of our knowledge, if studies about each carpal bone shape exist, they are always considered separately. Yet these bones are so close to each other, and articulate in such an intricate way, that the shape of a bone necessarily influences its neighbors. It would be interesting to study the carp as a whole. This would mostly be useful for transplants, in order to customize the bone for the individual, so it has the optimal form considering the rest of the wrist. In a second phase, the influence of the bones shapes on the wrist movement could be studied, with the similar idea of customizing a healthy motion model that could be used for diagnosing.

APPENDIX

Contents

X.1	Volume dissimilarity: CMC resampling	142
X.2	Volume dissimilarity: template set creation	143
X.3	Volume dissimilarity: Laplacian deformation	144
X.4	Volume dissimilarity: Laplacian + projection registration	145
X.5	Statistical Movement Model: Generalization	146

X.1 Volume dissimilarity: CMC resampling

The volume dissimilarity between the CMC meshes $M_{O,\{b,i\}}$ and the resampled ones $M_{D,\{b,i\}}$ is measured with the Jaccard and Dice coefficients. These results are discussed in Sec. 2.3.1.b.

	Dice coef. (1.5)			Jaccard distance (1.4)		
	mean	max	std	mean	max	std
Radius	0.001	0.001	0.000	0.001	0.002	0.000
Scaphoid	0.001	0.002	0.000	0.002	0.003	0.000
Lunate	0.001	0.002	0.000	0.002	0.003	0.001
Triquetrum	0.001	0.002	0.000	0.002	0.003	0.001
Pisiform	0.001	0.002	0.000	0.003	0.004	0.001
Trapezoid	0.001	0.002	0.000	0.002	0.003	0.000
Trapezium	0.001	0.002	0.000	0.002	0.004	0.001
Capitate	0.001	0.002	0.000	0.002	0.003	0.000
Hamate	0.001	0.002	0.000	0.002	0.003	0.000
Metac. 1	0.001	0.002	0.000	0.001	0.004	0.002
Metac. 2	0.001	0.001	0.000	0.002	0.003	0.000
Metac. 3	0.001	0.002	0.000	0.002	0.005	0.001
Metac. 4	0.001	0.002	0.000	0.002	0.005	0.001
Metac. 5	0.001	0.001	0.000	0.002	0.003	0.000

Table X.1: Jaccard and Dice coefficients between the meshes $M_{O,\{b,i\}}$ and the resampled ones $M_{D,\{b,i\}}$ to regularize the vertices and edges repartition on the surface.

X.2 Volume dissimilarity: template set creation

The volume dissimilarity between the database meshes $M_{R,\{b,i\}}$ and the templates $M_{T,\{b\}}$ is measured with the Jaccard and Dice coefficients. These results are discussed in Sec. 2.3.2.

	Dice coef. (1.5)			Jaccard distance (1.4)		
	mean	max	std	mean	max	std
Radius	0.061	0.109	0.019	0.115	0.196	0.034
Scaphoid	0.078	0.121	0.017	0.144	0.216	0.030
Lunate	0.073	0.161	0.021	0.135	0.277	0.036
Triquetrum	0.079	0.151	0.020	0.146	0.262	0.033
Pisiform	0.079	0.134	0.020	0.145	0.237	0.033
Trapezoid	0.081	0.112	0.016	0.150	0.202	0.028
Trapezium	0.079	0.136	0.018	0.145	0.239	0.031
Capitate	0.070	0.130	0.015	0.131	0.230	0.025
Hamate	0.078	0.123	0.016	0.145	0.219	0.027
Metac. 1	0.073	0.193	0.026	0.134	0.324	0.042
Metac. 2	0.085	0.160	0.025	0.156	0.276	0.041
Metac. 3	0.084	0.180	0.028	0.153	0.306	0.047
Metac. 4	0.086	0.153	0.027	0.158	0.265	0.045
Metac. 5	0.085	0.160	0.024	0.156	0.276	0.040

Table X.2: Jaccard and Dice coeffs between the templates meshes $M_{T,\{b\}}$ and the database ones $M_{R,\{b,i\}}$.

X.3 Volume dissimilarity: Laplacian deformation

The volume dissimilarity between the database meshes $M_{R,\{b,i\}}$ and the templates registered using Laplacian deformation $M_{L,\{b,i\}}$ is measured with the Jaccard and Dice coefficients. These results are discussed in Sec. 2.3.3.a.

	Dice coef. (1.5)			Jaccard distance (1.4)		
	mean	max	std	mean	max	std
Radius	0.040	0.067	0.010	0.077	0.126	0.017
Scaphoid	0.042	0.055	0.005	0.081	0.103	0.009
Lunate	0.036	0.062	0.006	0.070	0.117	0.011
Triquetrum	0.051	0.074	0.006	0.097	0.138	0.012
Pisiform	0.044	0.057	0.005	0.083	0.108	0.009
Trapezoid	0.048	0.080	0.008	0.091	0.148	0.015
Trapezium	0.062	0.098	0.012	0.117	0.178	0.020
Capitate	0.046	0.055	0.005	0.088	0.105	0.009
Hamate	0.054	0.075	0.007	0.102	0.140	0.013
Metac. 1	0.046	0.063	0.006	0.089	0.118	0.011
Metac. 2	0.047	0.055	0.003	0.090	0.104	0.006
Metac. 3	0.045	0.055	0.004	0.087	0.105	0.008
Metac. 4	0.054	0.069	0.007	0.102	0.129	0.013
Metac. 5	0.050	0.064	0.005	0.096	0.120	0.009

Table X.3: Jaccard and Dice coeffs between the database meshes $M_{R,\{b,i\}}$ and the Laplacian deformed templates $M_{L,\{b,i\}}$.

X.4 Volume dissimilarity: Laplacian + projection registration

The volume dissimilarity between the database meshes $M_{R,\{b,i\}}$ and the templates registered using a combination of Laplacian deformation and projection along the normals $M_{W,\{b,i\}}$ is measured with the Jaccard and Dice coefficients. These results are discussed in Sec. 2.3.3.b.

	Dice coef. (1.5)			Jaccard distance (1.4)		
	mean	max	std	mean	max	std
Radius	0.007	0.014	0.004	0.013	0.027	0.007
Scaphoid	0.008	0.011	0.001	0.017	0.023	0.002
Lunate	0.009	0.015	0.002	0.017	0.030	0.004
Triquetrum	0.012	0.019	0.002	0.024	0.037	0.004
Pisiform	0.012	0.020	0.002	0.023	0.038	0.005
Trapezoid	0.012	0.019	0.003	0.023	0.037	0.005
Trapezium	0.013	0.021	0.003	0.025	0.040	0.006
Capitate	0.008	0.010	0.001	0.016	0.019	0.002
Hamate	0.009	0.016	0.002	0.018	0.031	0.003
Metac. 1	0.007	0.010	0.001	0.013	0.021	0.003
Metac. 2	0.007	0.011	0.001	0.015	0.022	0.003
Metac. 3	0.008	0.010	0.001	0.015	0.019	0.002
Metac. 4	0.009	0.011	0.001	0.018	0.023	0.003
Metac. 5	0.009	0.013	0.002	0.017	0.026	0.003

Table X.4: Jaccard and Dice coeffs between the database meshes $M_{R,\{b,i\}}$ and the final deformed templates $M_{W,\{b,i\}}$.

X.5 Statistical Movement Model: Generalization

In Tables X.5, X.6, X.7 are presented measures of the generalization capacity of the movement model by linear regression. For each individual separately, each pose was by turn left out of the training set and the bones orientations and locations were calculated from the predictor values. These orientation and location values are compared to the experimental ones. The results are discussed in Sec. 4.3.4.

MC3 Pose	Model 1		Model 2	
	Translation (mm)	Rotation (°)	Translation (mm)	Rotation (°)
Neutral	0.391	0.296	0.561	0.201
Adduction	0.329	0.230	0.657	1.452
Abduction	0.308	0.261	0.634	2.260
Extension	0.306	0.200	0.613	2.365
Flexion	0.309	0.178	0.631	2.724
Pinch, no load	0.354	0.178	0.649	2.346
Pinch, loaded	0.359	0.068	0.627	2.098
Grasp, no load	0.376	0.050	0.646	1.938
Grasp, load	0.374	0.038	0.625	1.790
Jar, no load	0.366	0.043	0.620	1.916
Jar, load	0.364	0.094	0.643	2.090

Table X.5: Average error over individuals between the experimental orientation and position of the MC3 and the values computed from the predictors, using two linear regression sets of parameters.

LUN Pose	Model 1		Model 2	
	Translation (mm)	Rotation (°)	Translation (mm)	Rotation (°)
Neutral	0.219	0.345	0.207	1.062
Adduction	0.187	0.412	0.234	1.542
Abduction	0.169	0.297	0.242	2.108
Extension	0.159	0.355	0.219	1.723
Flexion	0.156	0.320	0.238	1.851
Pinch, no load	0.157	0.221	0.236	1.621
Pinch, loaded	0.160	0.258	0.250	1.842
Grasp, no load	0.161	0.243	0.261	1.950
Grasp, load	0.158	0.271	0.261	1.946
Jar, no load	0.153	0.255	0.270	2.015
Jar, load	0.157	0.294	0.308	2.403

Table X.6: Average error over individuals between the experimental orientation and position of the LUN and the values computed from the predictors, using two linear regression sets of parameters.

HAM Pose	Model 1		Model 2	
	Translation (mm)	Rotation (°)	Translation (mm)	Rotation (°)
Neutral	0.274	0.714	0.419	1.039
Adduction	0.234	0.513	0.435	0.865
Abduction	0.230	0.490	0.442	2.117
Extension	0.213	0.405	0.407	1.716
Flexion	0.205	0.385	0.441	2.288
Pinch, no load	0.212	0.369	0.433	2.002
Pinch, loaded	0.222	0.309	0.445	2.122
Grasp, no load	0.232	0.236	0.458	2.235
Grasp, load	0.239	0.119	0.445	2.143
Jar, no load	0.236	0.123	0.445	2.287
Jar, load	0.234	0.131	0.475	2.495

Table X.7: Average error over individuals between the experimental orientation and position of the HAM and the values computed from the predictors, using two linear regression sets of parameters.

Pose	LUN		HAM	
	Translation (mm)	Rotation (°)	Translation (mm)	Rotation (°)
Thumb Adduction	0.21	1.30	0.60	3.29
Thumb Abduction	0.24	2.25	0.47	2.98
Thumb Extension	0.28	2.38	0.60	5.67
Thumb Flexion	0.28	2.40	0.55	5.21
Pinch, no load	0.29	4.93	0.63	7.26
Pinch, loaded	0.35	6.75	0.72	12.98
Grasp, no load	0.52	10.82	0.91	23.78
Grasp, load	0.62	20.74	1.16	38.83
Jar, no load	0.81	18.66	1.47	34.33
Jar, load	0.98	17.30	1.56	22.24

Table X.8: Average rotation and translation in absolute values between the neutral pose and the other poses for the LUN and HAM bones.

BIBLIOGRAPHY

- [ADVDI05] Pierre Alliez, Éric Colin De Verdière, Olivier Devillers, and Martin Isenburg. Centroidal voronoi diagrams for isotropic surface remeshing. *Graphical models*, 67(3):204–231, 2005.
- [ARJ⁺14] Emran Mohammad Abu Anas, Abtin Rasoulia, Paul St John, David Pichora, Robert Rohling, and Purang Abolmaesumi. A statistical shape+pose model for segmentation of wrist ct images. In *Medical Imaging 2014: Image Processing*, volume 9034, page 90340T. International Society for Optics and Photonics, 2014.
- [ARJ⁺15] Emran Mohammad Abu Anas, Abtin Rasoulia, Paul St John, David Pichora, Parvin Mousavi, Victoria A Lessoway, Alexander Seitel, Ilker Hacihaliloglu, Robert Rohling, and Purang Abolmaesumi. Scaphoid fracture fixation: localization of bones through statistical model to ultrasound registration. In *Medical Imaging 2015: Image-Guided Procedures, Robotic Interventions, and Modeling*, volume 9415, page 94150P. International Society for Optics and Photonics, 2015.
- [ARS⁺16] Emran Mohammad Abu Anas, Abtin Rasoulia, Alexander Seitel, Kathryn Darras, David Wilson, Paul St John, David Pichora, Parvin Mousavi, Robert Rohling, and Purang Abolmaesumi. Automatic segmentation of wrist bones in ct using a statistical wrist shape + pose model. *IEEE transactions on medical imaging*, 35(8):1789–1801, 2016.
- [ASM⁺19] Nadim Aizarani, Antonio Saviano, Laurent Mailly, Sarah Durand, Josip S Herman, Patrick Pessaux, Thomas F Baumert, Dominic Grün, et al. A human liver cell atlas reveals heterogeneity and epithelial progenitors. *Nature*, page 1, 2019.
- [ASR⁺16] Emran Mohammad Abu Anas, Alexander Seitel, Abtin Rasoulia, Paul St John, Tamas Ungi, Andras Lasso, Kathryn Darras, David Wilson, Victoria A Lessoway, Gabor Fichtinger, et al. Registration of a statistical

model to intraoperative ultrasound for scaphoid screw fixation. *International journal of computer assisted radiology and surgery*, 11(6):957–965, 2016.

- [BBD12] Ian M Bullock, Júlia Borràs, and Aaron M Dollar. Assessing assumptions in kinematic hand models: a review. In *2012 4th IEEE RAS & EMBS International Conference on Biomedical Robotics and Biomechanics (BioRob)*, pages 139–146. IEEE, 2012.
- [BCM⁺15] Gregory I Bain, Harry DS Clitherow, Stuart Millar, François Fraysse, John J Costi, Kevin Eng, Duncan T McGuire, and Dominic Thewlis. The effect of lunate morphology on the 3-dimensional kinematics of the carpus. *The Journal of hand surgery*, 40(1):81–89, 2015.
- [BGK95] Ch Brechbühler, Guido Gerig, and Olaf Kübler. Parametrization of closed surfaces for 3-d shape description. *Computer vision and image understanding*, 61(2):154–170, 1995.
- [BGSWI07] Serdar K Balci, Polina Golland, Martha Shenton, and William M Wells III. Free-form b-spline deformation model for groupwise registration. *Med Image Comput Comput Assist Interv*, 10(WS):23–30, 2007 2007.
- [BHL⁺88] Robert J Belsole, Don R Hilbelink, J Anthony Llewellyn, Stephen Stenzler, Thomas L Greene, and Mark Dale. Mathematical analysis of computed carpal models. *Journal of Orthopaedic Research*, 6(1):116–122, 1988.
- [BHL⁺91] Robert J Belsole, Don R Hilbelink, J Anthony Llewellyn, Mark Dale, and John A Ogden. Carpal orientation from computed reference axes. *Journal of Hand Surgery*, 16(1):82–90, 1991.
- [BHP⁺04] K. K. Bhatia, J. V. Hajnal, B. K. Puri, A. D. Edwards, and D. Rueckert. Consistent groupwise non-rigid registration for atlas construction. In *Proceedings of the IEEE Symposium on Biomedical Imaging (ISBI)*, pages 908–911, 2004.
- [BKA11] Anil K Bhat, Bhaskaranand Kumar, and Ashwath Acharya. Radiographic imaging of the wrist. *Indian journal of plastic surgery: official publication of the Association of Plastic Surgeons of India*, 44(2):186, 2011.
- [BM92] Paul J Besl and Neil D McKay. Method for registration of 3-d shapes. In *Sensor Fusion IV: Control Paradigms and Data Structures*, volume 1611, pages 586–607. International Society for Optics and Photonics, 1992.
- [BV⁺99] Volker Blanz, Thomas Vetter, et al. A morphable model for the synthesis of 3d faces. In *Siggraph*, volume 99, pages 187–194, 1999.
- [CBS⁺05] Bart Carelsen, Niels H Bakker, Simon D Strackee, Sjirk N Boon, Mario Maas, Jörg Sabczynski, Cornelis A Grimbergen, and Geert J Streekstra. 4d rotational x-ray imaging of wrist joint dynamic motion. *Medical physics*, 32(9):2771–2776, 2005.

- [CCMU05] Joseph J. Crisco, James C. Coburn, Douglas C. Moore, and Mohammad A. Upal. Carpal bone size and scaling in men versus in women. *The Journal of Hand Surgery*, 30(1):35 – 42, 2005.
- [CDC⁺09] Laurence Cheze, Raphaël Dumas, Jean-Jacques Comtet, Claude Rumelhart, and Michel Fayet. A joint coordinate system proposal for the study of the trapeziometacarpal joint kinematics. *Computer methods in biomechanics and biomedical engineering*, 12(3):277–282, 2009.
- [CGHM11] Xin Chen, Jim Graham, Charles Hutchinson, and Lindsay Muir. Inferring 3d kinematics of carpal bones from single view fluoroscopic sequences. In *International Conference on Medical Image Computing and Computer-Assisted Intervention*, pages 680–687. Springer, 2011.
- [CGHM12] Xin Chen, Jim Graham, Charles Hutchinson, and Lindsay Muir. Automatic inference and measurement of 3d carpal bone kinematics from single view fluoroscopic sequences. *IEEE transactions on medical imaging*, 32(2):317–328, 2012.
- [CGHM13] Xin Chen, Jim Graham, Charles Hutchinson, and Lindsay Muir. Automatic generation of statistical pose and shape models for articulated joints. *IEEE transactions on medical imaging*, 33(2):372–383, 2013.
- [CHM⁺15] Joseph J Crisco, Eni Halilaj, Douglas C Moore, Tarpit Patel, Arnold-Peter C Weiss, and Amy L Ladd. In vivo kinematics of the trapeziometacarpal joint during thumb extension-flexion and abduction-adduction. *The Journal of hand surgery*, 40(2):289–296, 2015.
- [CHTH94] Timothy F Cootes, Andrew Hill, Christopher J Taylor, and Jane Haslam. Use of active shape models for locating structures in medical images. *Image and vision computing*, 12(6):355–365, 1994.
- [CJS⁺08] Bart Carelsen, Remmet Jonges, Simon D Strackee, Mario Maas, Patricia van Kemenade, Cornelis A Grimbergen, Marcel van Herk, and Geert J Streekstra. Detection of in vivo dynamic 3-d motion patterns in the wrist joint. *IEEE Transactions on Biomedical Engineering*, 56(4):1236–1244, 2008.
- [CLCL81] William P Cooney, Michael J Lucca, EY Chao, and RL Linscheid. The kinesiology of the thumb trapeziometacarpal joint. *J Bone Joint Surg Am*, 63(9):1371–1381, 1981.
- [CLW⁺14] Abhijit J Chaudhari, Richard M Leahy, Barton L Wise, Nancy E Lane, Ramsey D Badawi, and Anand A Joshi. Global point signature for shape analysis of carpal bones. *Physics in Medicine & Biology*, 59(4):961, 2014.
- [CM92] Yang Chen and Gérard Medioni. Object modelling by registration of multiple range images. *Image and vision computing*, 10(3):145–155, 1992.
- [CMW99] Joseph J Crisco, Robert D McGovern, and Scott W Wolfe. Noninvasive technique for measuring in vivo three-dimensional carpal bone kinematics. *Journal of orthopaedic research*, 17(1):96–100, 1999.

- [CPHM15] Joseph J Crisco, Tarpit Patel, Eni Halilaj, and Douglas C Moore. The envelope of physiological motion of the first carpometacarpal joint. *Journal of biomechanical engineering*, 137(10):101002, 2015.
- [CRZL04] H. Chui, A. Rangarajan, J. Zhang, and C. M. Leonard. Unsupervised learning of an atlas from unlabeled point-sets. *IEEE Transactions on Pattern Analysis and Machine Intelligence*, 26(2):160–172, Feb 2004.
- [CSM03] David Cohen-Steiner and Jean-Marie Morvan. Restricted delaunay triangulations and normal cycle. In *Proceedings of the nineteenth annual symposium on Computational geometry*, pages 312–321. ACM, 2003.
- [CT95] Timothy F Cootes and Christopher J Taylor. Combining point distribution models with shape models based on finite element analysis. *Image and Vision Computing*, 13(5):403–409, 1995.
- [CTCG95] Timothy F Cootes, Christopher J Taylor, David H Cooper, and Jim Graham. Active shape models-their training and application. *Computer vision and image understanding*, 61(1):38–59, 1995.
- [CUC07] James C Coburn, Mohammad A Upal, and Joseph J Crisco. Coordinate systems for the carpal bones of the wrist. *Journal of biomechanics*, 40(1):203–209, 2007.
- [DCLCC05] Ugo Della Croce, Alberto Leardini, Lorenzo Chiari, and Aurelio Cappozzo. Human movement analysis using stereophotogrammetry: Part 4: assessment of anatomical landmark misplacement and its effects on joint kinematics. *Gait & posture*, 21(2):226–237, 2005.
- [DCT01] Rhodri H Davies, Tim F Cootes, and Chris J Taylor. A minimum description length approach to statistical shape modelling. In *Biennial International Conference on Information Processing in Medical Imaging*, pages 50–63. Springer, 2001.
- [DDK⁺17] Priscilla D’agostino, Benjamin Dourthe, Faes Kerkhof, Filip Stockmans, and Evie E Vereecke. In vivo kinematics of the thumb during flexion and adduction motion: Evidence for a screw-home mechanism. *Journal of Orthopaedic Research*, 35(7):1556–1564, 2017.
- [DPTA09] Stanley Durrleman, Xavier Pennec, Alain Trouvé, and Nicholas Ayache. Statistical models of sets of curves and surfaces based on currents. *Medical Image Analysis*, 13(5):793 – 808, 2009. Includes Special Section on the 12th International Conference on Medical Imaging and Computer Assisted Intervention.
- [DTC⁺02] Rhodri H Davies, Carole J Twining, Tim F Cootes, John C Waterton, and Chris J Taylor. 3d statistical shape models using direct optimisation of description length. In *European conference on computer vision*, pages 3–20. Springer, 2002.

- [DTCT09] Rhodri H Davies, Carole J Twining, Timothy F Cootes, and Chris J Taylor. Building 3-d statistical shape models by direct optimization. *IEEE Transactions on Medical Imaging*, 29(4):961–981, 2009.
- [DTS03] Christos Davatzikos, Xiaodong Tao, and Dinggang Shen. Hierarchical active shape models, using the wavelet transform. *IEEE transactions on medical imaging*, 22(3):414–423, 2003.
- [DTT08] Rhodri Davies, Carole Twining, and Chris Taylor. *Statistical models of shape: Optimisation and evaluation*. Springer Science & Business Media, 2008.
- [Duv14] David Duvenaud. *Automatic model construction with Gaussian processes*. PhD thesis, University of Cambridge, 2014.
- [EK06] Anders Ericsson and Johan Karlsson. Benchmarking of algorithms for automatic correspondence localisation. In *BMVC*, pages 759–768, 2006.
- [FJB⁺18] Brent Foster, Anand A Joshi, Marissa Borgese, Yasser Abdelhafez, Robert D Boutin, and Abhijit J Chaudhari. Wrist: A wrist image segmentation toolkit for carpal bone delineation from mri. *Computerized Medical Imaging and Graphics*, 63:31–40, 2018.
- [FSJ⁺09] M Foumani, SD Strackee, R Jonges, L Blankevoort, AH Zwinderman, B Carelsen, and GJ Streekstra. In-vivo three-dimensional carpal bone kinematics during flexion–extension and radio–ulnar deviation of the wrist: Dynamic motion versus step-wise static wrist positions. *Journal of biomechanics*, 42(16):2664–2671, 2009.
- [GBM07] Ian Galley, Gregory I Bain, and James M McLean. Influence of lunate type on scaphoid kinematics. *The Journal of hand surgery*, 32(6):842–847, 2007.
- [GLU12] Andreas Geiger, Philip Lenz, and Raquel Urtasun. Are we ready for autonomous driving? the kitti vision benchmark suite. In *2012 IEEE Conference on Computer Vision and Pattern Recognition*, pages 3354–3361. IEEE, 2012.
- [GM98] Ulf Grenander and Michael I Miller. Computational anatomy: An emerging discipline. *Quarterly of applied mathematics*, 56(4):617–694, 1998.
- [GS83] Edward S Grood and Wilfredo J Suntay. A joint coordinate system for the clinical description of three-dimensional motions: application to the knee. *Journal of biomechanical engineering*, 105(2):136–144, 1983.
- [GSJ⁺01] Guido Gerig, Martin Styner, D Jones, Daniel Weinberger, and Jeffrey Lieberman. Shape analysis of brain ventricles using spharm. In *Proceedings IEEE Workshop on Mathematical Methods in Biomedical Image Analysis (MMBIA 2001)*, pages 171–178. IEEE, 2001.
- [HAC⁺15] DJ Hunter, N Arden, F Cicuttini, MD Crema, B Dardzinski, J Duryea, A Guermazi, IK Haugen, M Kloppenburg, E Maheu, et al. Oarsi clinical

trials recommendations: hand imaging in clinical trials in osteoarthritis. *Osteoarthritis and cartilage*, 23(5):732–746, 2015.

- [HBM⁺92] Anne Hollister, William L Buford, Loyd M Myers, David J Giurintano, and Andrew Novick. The axes of rotation of the thumb carpometacarpal joint. *Journal of Orthopaedic Research*, 10(3):454–460, 1992.
- [HGEA⁺91] E Horii, M Garcia-Elias, KN An, Allen Thorp Bishop, WP Cooney, RL Linscheid, and EYS Chao. A kinematic study of luno-triquetral dissociations. *The Journal of hand surgery*, 16(2):355–362, 1991.
- [HM09] Tobias Heimann and Hans-Peter Meinzer. Statistical shape models for 3d medical image segmentation: a review. *Medical image analysis*, 13(4):543–563, 2009.
- [HMK⁺02] Peter Heinze, Dietmar Meister, Rudolf Kober, Jörg Raczekowsky, and H Worn. Atlas-based segmentation of pathological knee joints. *Studies in health technology and informatics*, pages 198–203, 2002.
- [HMP⁺14] Eni Halilaj, Douglas C Moore, Tarpit K Patel, David H Laidlaw, Amy L Ladd, Arnold-Peter C Weiss, and Joseph J Crisco. Thumb carpometacarpal joint congruence during functional tasks and thumb range-of-motion activities. In *2014 36th Annual International Conference of the IEEE Engineering in Medicine and Biology Society*, pages 4354–4357. IEEE, 2014.
- [HPE⁺08] Heike Hufnagel, Xavier Pennec, Jan Ehrhardt, Nicholasand Ayache, and Heinz Handels. Generation of a statistical shape model with probabilistic point correspondences and the expectation maximization- iterative closest point algorithm. *International Journal of Computer Assisted Radiology and Surgery*, 2(5):265–273, Mar 2008.
- [HRG⁺13] Eni Halilaj, Michael J Rainbow, Christopher J Got, Douglas C Moore, and Joseph J Crisco. A thumb carpometacarpal joint coordinate system based on articular surface geometry. *Journal of biomechanics*, 46(5):1031–1034, 2013.
- [HRG⁺14] Eni Halilaj, Michael J Rainbow, Christopher Got, Joel B Schwartz, Douglas C Moore, Arnold-Peter C Weiss, Amy L Ladd, and Joseph J Crisco. In vivo kinematics of the thumb carpometacarpal joint during three isometric functional tasks. *Clinical Orthopaedics and Related Research*[®], 472(4):1114–1122, 2014.
- [HWM06] Tobias Heimann, Ivo Wolf, and Hans-Peter Meinzer. Optimal landmark distributions for statistical shape model construction. In *Medical Imaging 2006: Image Processing*, volume 6144, page 61441J. International Society for Optics and Photonics, 2006.
- [JCL⁺10] Anand A Joshi, Abhijit J Chaudhari, Changqing Li, Joyita Dutta, Simon R Cherry, David W Shattuck, Arthur W Toga, and Richard M Leahy.

- Digiwarp: a method for deformable mouse atlas warping to surface topographic data. *Physics in Medicine & Biology*, 55(20):6197, 2010.
- [JL06] Lynette A Jones and Susan J Lederman. *Human hand function*. Oxford University Press, 2006.
- [JLBC16] Anand A. Joshi, Richard M. Leahy, Ramsey D. Badawi, and Abhijit J. Chaudhari. Registration-Based Morphometry for Shape Analysis of the Bones of the Human Wrist. *IEEE Transactions on Medical Imaging*, 35(2):416–426, February 2016.
- [Jol11] Ian Jolliffe. *Principal component analysis*. Springer, 2011.
- [KOT⁺18] Yohei Kawanishi, Kunihiro Oka, Hiroyuki Tanaka, Kiyoshi Okada, Kazuomi Sugamoto, and Tsuyoshi Murase. In vivo 3-dimensional kinematics of thumb carpometacarpal joint during thumb opposition. *The Journal of hand surgery*, 43(2):182–e1, 2018.
- [KPL⁺03] Michael R Kaus, Vladimir Pekar, Cristian Lorenz, Roel Truyen, Steven Lobregt, and Jürgen Weese. Automated 3-d pdm construction from segmented images using deformable models. *IEEE Transactions on Medical Imaging*, 22(8):1005–1013, 2003.
- [KSCP11] Martin Koch, Alexander G Schwing, Dorin Comaniciu, and Marc Pollefeys. Fully automatic segmentation of wrist bones for arthritis patients. In *2011 IEEE International Symposium on Biomedical Imaging: From Nano to Macro*, pages 636–640. IEEE, 2011.
- [KWT88] Michael Kass, Andrew Witkin, and Demetri Terzopoulos. Snakes: Active contour models. *International Journal of Computer Vision*, 1(4):321–331, Jan 1988.
- [Lé] Bruno Lévy. Graphite.
- [Lav11] Guillaume Lavoué. A multiscale metric for 3d mesh visual quality assessment. In *Computer Graphics Forum*, volume 30, pages 1427–1437. Wiley Online Library, 2011.
- [LC87] William E Lorensen and Harvey E Cline. Marching cubes: A high resolution 3d surface construction algorithm. In *ACM siggraph computer graphics*, volume 21, pages 163–169. ACM, 1987.
- [LFGV17] Marcel Lüthi, Andreas Forster, Thomas Gerig, and Thomas Vetter. Shape modeling using gaussian process morphable models. In *Statistical Shape and Deformation Analysis*, pages 165–191. Elsevier, 2017.
- [LGJV17] Marcel Lüthi, Thomas Gerig, Christoph Jud, and Thomas Vetter. Gaussian process morphable models. *IEEE transactions on pattern analysis and machine intelligence*, 40(8):1860–1873, 2017.
- [LJV13] Marcel Lüthi, Christoph Jud, and Thomas Vetter. A unified approach to shape model fitting and non-rigid registration. In *International workshop on machine learning in medical imaging*, pages 66–73. Springer, 2013.

- [LRR⁺17] Or Litany, Tal Remez, Emanuele Rodolà, Alex Bronstein, and Michael Bronstein. Deep functional maps: Structured prediction for dense shape correspondence. In *Proceedings of the IEEE International Conference on Computer Vision*, pages 5659–5667, 2017.
- [MCTL07] Douglas C Moore, Joseph J Crisco, Theodore G Trafton, and Evan L Leventhal. A digital database of wrist bone anatomy and carpal kinematics. *Journal of biomechanics*, 40(11):2537–2542, 2007.
- [MDBG97] M Maas, PF Dijkstra, KE Bos, and F Groenevelt. Dynamics of the painful wrist—a video fluoroscopic approach. *Proceedings of ECR*, page A008, 1997.
- [MDW08] Brent C Munsell, Pahal Dalal, and Song Wang. Evaluating shape correspondence for statistical shape analysis: A benchmark study. *IEEE Transactions on Pattern Analysis and Machine Intelligence*, 30(11):2023–2039, 2008.
- [MSR⁺01] Thybout M Moojen, Jeroen G Snel, Marco JPF Ritt, Henk W Venema, Gerard J den Heeten, and Kurt E Bos. Pisiform kinematics in vivo. *The Journal of hand surgery*, 26(5):901–907, 2001.
- [MSR⁺02a] Thybout M Moojen, Jeroen G Snel, Marco JPF Ritt, Henk W Venema, John MG Kauer, and Kurt E Bos. Scaphoid kinematics in vivo. *The Journal of hand surgery*, 27(6):1003–1010, 2002.
- [MSR⁺02b] TM Moojen, JG Snel, MJPF Ritt, JMG Kauer, HW Venema, and KE Bos. Three-dimensional carpal kinematics in vivo. *Clinical Biomechanics*, 17(7):506–514, 2002.
- [MSR⁺03] Thybout M Moojen, Jeroen G Snel, Marco JPF Ritt, Henk W Venema, John MG Kauer, and Kurt E Bos. In vivo analysis of carpal kinematics and comparative review of the literature. *The Journal of hand surgery*, 28(1):81–87, 2003.
- [MSR⁺15] Stefano Moriconi, Elisa Scalco, Tiziana Rancati, Antonella Messina, Tommaso Giandini, Riccardo Valdagni, and Giovanna Rizzo. Application and evaluation of wavelet-based surface reconstruction for contour propagation in radiotherapy. In *Proceedings of MICCAI workshop on imaging and computer assistance in radiation therapy (ICART)*, volume 9, pages 58–65, 2015.
- [MT07] P A J McNee and J Teh. Imaging of the wrist. *Imaging*, 19(3):208–219, 2007.
- [MvdWN⁺10] Michelle Marshall, Danielle van der Windt, Elaine Nicholls, Helen Myers, and Krysia Dziedzic. Radiographic thumb osteoarthritis: frequency, patterns and associations with pain and clinical assessment findings in a community-dwelling population. *Rheumatology*, 50(4):735–739, 2010.
- [NBP⁺00] Koji Nakamura, Moroe Beppu, Rita M Patterson, Curtis A Hanson, Paul J Hume, and Steven F Viegas. Motion analysis in two dimensions

of radial-ulnar deviation of type i versus type ii lunates. *The Journal of hand surgery*, 25(5):877–888, 2000.

- [NHBT07] Delphine Nain, Steven Haker, Aaron Bobick, and Allen Tannenbaum. Multiscale 3-d shape representation and segmentation using spherical wavelets. *IEEE Transactions on Medical Imaging*, 26(4):598–618, 2007.
- [PEVB95] Rita M Patterson, Karen W Elder, Steven F Viegas, and William L Buford. Carpal bone anatomy measured by computer analysis of three-dimensional reconstructions of computed tomography images. *The Journal of hand surgery*, 20(6):923–929, 1995.
- [PML16] Valentina Pedoia, Sharmila Majumdar, and Thomas M Link. Segmentation of joint and musculoskeletal tissue in the study of arthritis. *Magnetic Resonance Materials in Physics, Biology and Medicine*, 29(2):207–221, 2016.
- [PNV⁺98] Rita M Patterson, Clarence L Nicodemus, Steven F Viegas, Karin W Elder, and Judah Rosenblatt. High-speed, three-dimensional kinematic analysis of the normal wrist. *The Journal of hand surgery*, 23(3):446–453, 1998.
- [PWMG85] Andrew K Palmer, Frederick W Werner, Dennis Murphy, and Richard Glisson. Functional wrist motion: a biomechanical study. *Journal of Hand Surgery*, 10(1):39–46, 1985.
- [RCIA⁺88] LK Ruby, WP Conney III, KN An, RL Linscheid, and EYS Chao. Relative motion of selected carpal bones: a kinematic analysis of the normal wrist. *The Journal of hand surgery*, 13(1):1–10, 1988.
- [RDD⁺14] Jordan Ringenberg, Makarand Deo, Vijay Devabhaktuni, Omer Berenfeld, Brett Snyder, Pamela Boyers, and Jeffrey Gold. Accurate reconstruction of 3d cardiac geometry from coarsely-sliced mri. *Computer methods and programs in biomedicine*, 113(2):483–493, 2014.
- [RIB⁺17] Pranav Rajpurkar, Jeremy Irvin, Aarti Bagul, Daisy Ding, Tony Duan, Hershel Mehta, Brandon Yang, Kaylie Zhu, Dillon Laird, Robyn L Ball, et al. Mura: Large dataset for abnormality detection in musculoskeletal radiographs. *arXiv preprint arXiv:1712.06957*, 2017.
- [RRA12] Abtin Rasoulian, Robert Rohling, and Purang Abolmaesumi. Group-wise registration of point sets for statistical shape models. *IEEE transactions on medical imaging*, 31(11):2025–2034, 2012.
- [RS10] M Revol and J-M Servant. Les ténodèses en chirurgie de la main. *Chirurgie de la main*, 29(1):1–9, 2010.
- [Rus07] Raif M Rustamov. Laplace-beltrami eigenfunctions for deformation invariant shape representation. In *Proceedings of the fifth Eurographics symposium on Geometry processing*, pages 225–233. Eurographics Association, 2007.

- [SCOL⁺04] Olga Sorkine, Daniel Cohen-Or, Yaron Lipman, Marc Alexa, Christian Rössl, and H-P Seidel. Laplacian surface editing. In *Proceedings of the 2004 Eurographics/ACM SIGGRAPH symposium on Geometry processing*, pages 175–184. ACM, 2004.
- [SD04] Y Shang and O Dossel. Statistical 3d shape-model guided segmentation of cardiac images. In *Computers in Cardiology, 2004*, pages 553–556. IEEE, 2004.
- [SHD01] Dinggang Shen, Edward H Herskovits, and Christos Davatzikos. An adaptive-focus statistical shape model for segmentation and shape modeling of 3-d brain structures. *IEEE transactions on medical imaging*, 20(4):257–270, 2001.
- [SOX⁺06] Martin Styner, Ipek Oguz, Shun Xu, Christian Brechbühler, Dimitrios Pantazis, James J Levitt, Martha E Shenton, and Guido Gerig. Framework for the statistical shape analysis of brain structures using spharm-pdm. *The insight journal*, (1071):242—250, 2006.
- [SRN⁺03] Martin A Styner, Kumar T Rajamani, Lutz-Peter Nolte, Gabriel Zsemlye, Gábor Székely, Christopher J Taylor, and Rhodri H Davies. Evaluation of 3d correspondence methods for model building. In *Biennial International Conference on Information Processing in Medical Imaging*, pages 63–75. Springer, 2003.
- [SVG02] Jeroen G Snel, Henk W Venema, and Cornelis A Grimbergen. Deformable triangular surfaces using fast 1-d radial lagrangian dynamics-segmentation of 3-d mr and ct images of the wrist. *IEEE transactions on medical imaging*, 21(8):888–903, 2002.
- [SVM⁺00] Jeroen G Snel, Henk W Venema, Thybout M Moojen, Marco JPF Ritt, Cornelis A Grimbergen, and Gerard J den Heeten. Quantitative in vivo analysis of the kinematics of carpal bones from three-dimensional ct images using a deformable surface model and a three-dimensional matching technique. *Medical physics*, 27(9):2037–2047, 2000.
- [VdBA⁺04] FM Vos, Paul W de Bruin, JGM Aubel, Geert J Streekstra, Mario Maas, Lucas J van Vliet, and Albert M Vossepoel. A statistical shape model without using landmarks. In *Proceedings of the 17th International Conference on Pattern Recognition, 2004. ICPR 2004.*, volume 3, pages 714–717. IEEE, 2004.
- [vdGFS⁺10] Martijn van de Giessen, Mahyar Foumani, Geert J Streekstra, Simon D Strackee, Mario Maas, Lucas J van Vliet, Kees A Grimbergen, and Frans M Vos. Statistical descriptions of scaphoid and lunate bone shapes. *Journal of biomechanics*, 43(8):1463–1469, 2010.
- [vdGFV⁺11] Martijn van de Giessen, Mahyar Foumani, Frans M Vos, Simon D Strackee, Mario Maas, Lucas J Van Vliet, Cornelis A Grimbergen, and Geert J Streekstra. A 4d statistical model of wrist bone motion patterns. *IEEE Transactions on Medical Imaging*, 31(3):613–625, 2011.

- [vdGSS⁺09] Martijn van de Giessen, Nienke Smitsman, Simon D Strackee, Lucas J Van Vliet, Kees A Grimbergen, Geert J Streekstra, and Frans M Vos. A statistical description of the articulating ulna surface for prosthesis design. In *2009 IEEE International Symposium on Biomedical Imaging: From Nano to Macro*, pages 678–681. IEEE, 2009.
- [VHE⁺93] Steve F Viegas, Gilbert R Hillman, Karin Elder, David Stoner, and Rita M Patterson. Measurement of carpal bone geometry by computer analysis of three-dimensional ct images. *The Journal of hand surgery*, 18(2):341–349, 1993.
- [vKZHCO11] Oliver van Kaick, Hao Zhang, Ghassan Hamarneh, and Daniel Cohen-Or. A survey on shape correspondence. In *Computer Graphics Forum*, volume 30, pages 1681–1707. Wiley Online Library, 2011.
- [WC95] Ge Wu and Peter R Cavanagh. Isb recommendations for standardization in the reporting of kinematic data. *Journal of biomechanics*, 28(10):1257–1261, 1995.
- [WCT⁺15] Justyna Włodarczyk, Kamila Czaplicka, Zbysław Tabor, Wadim Wojciechowski, and Andrzej Urbanik. Segmentation of bones in magnetic resonance images of the wrist. *International journal of computer assisted radiology and surgery*, 10(4):419–431, 2015.
- [WS00] Yongmei Wang and Lawrence H Staib. Boundary finding with prior shape and smoothness models. *IEEE Transactions on Pattern Analysis and Machine Intelligence*, 22(7):738–743, 2000.
- [WS01] Christopher KI Williams and Matthias Seeger. Using the nyström method to speed up kernel machines. In *Advances in neural information processing systems*, pages 682–688, 2001.
- [WVdHV⁺05] Ge Wu, Frans CT Van der Helm, HEJ DirkJan Veeger, Mohsen Makhsous, Peter Van Roy, Carolyn Anglin, Jochem Nagels, Andrew R Karduna, Kevin McQuade, Xuguang Wang, et al. Isb recommendation on definitions of joint coordinate systems of various joints for the reporting of human joint motion—part ii: shoulder, elbow, wrist and hand. *Journal of biomechanics*, 38(5):981–992, 2005.
- [ZAT05] Zheen Zhao, Stephen R. Aylward, and Eam Khwang Teoh. A novel 3d partitioned active shape model for segmentation of brain mr images. In James S. Duncan and Guido Gerig, editors, *Medical Image Computing and Computer-Assisted Intervention – MICCAI 2005*, pages 221–228, Berlin, Heidelberg, 2005. Springer Berlin Heidelberg.
- [ZH17] Xiahai Zhuang and Yipeng Hu. Chapter 2 - statistical deformation model: Theory and methods. In Guoyan Zheng, Shuo Li, and Gabor Székely, editors, *Statistical Shape and Deformation Analysis*, pages 33 – 65. Academic Press, 2017.

- [ZT05] Zheen Zhao and Eam Khwang Teoh. A novel framework for automated 3d pdm construction using deformable models. In *Medical Imaging 2005: Image Processing*, volume 5747, pages 303–315. International Society for Optics and Photonics, 2005.

The wrist is an essential joint, source of the large range of motion of the hand. It is also a complex joint, composed of eight small bones, connected to five metacarpal bones and two forearm bones. The complexity of the joint is not only due to the high number of interconnected bones, but also to the small size of the carpal bones and their elaborate shapes interlocked with each other, that move in an intricate way around each other. In this thesis we are interested in modeling the 3D wrist bone shapes. Not many works on wrist bones modeling have been conducted yet and little data have been collected into databases exploitable for computer models. The latter can be used to take measurements, serve as basis for the creation of automated IT tools, or else be integrated into software for diagnosis support for example. The quality of the results of such applications depends on the quality of the model. We therefore attach a special importance to the validation of our work, while such assessment cannot directly be measured and must be proven by indirect metrics. Interest was taken in tools for the modeling of 3D shapes, especially in techniques of correspondence between 3D meshes. We propose a method to transform raw meshes extracted from CT scans into bones representations with correspondence relations. The dense correspondence relations computed make possible many applications, that serve as further validation of the correspondence results. We propose several utilizations. Variability among bones is analyzed with statistical procedures such as the Principal Component Analysis (PCA) and another one based on Gaussian Processes. The registration capacities of the first model are employed for defining correspondence with a second database. We propose a method to easily transfer systems of coordinates or other landmarks from a few example towards the rest of the database, a convenient function for biomechanical wrist motion study. In a last phase, we are concerned with modeling wrist bones motions with a parametric model based on meaningful and easily measurable predictors.

* * *

Le poignet humain est une articulation essentielle, car il est à l'origine de la grande amplitude de mouvement de la main. C'est également une articulation complexe, composée de huit petits os carpiens, qui sont connectés aux cinq métacarpes et aux deux os de l'avant-bras. La complexité de l'articulation est non seulement due à ce grand nombre d'os, mais également à la petite taille des os carpiens et à leurs formes élaborées, qui rendent le mouvement des os les uns autour des autres également complexe. Dans cette thèse, nous nous sommes intéressés à la modélisation 3D de la forme des os. Peu de travaux ont été menés jusqu'à présent sur la modélisation des os du poignet, et peu de données exploitables pour des modèles informatiques ont été collectées. Or de tels modèles informatiques peuvent avoir de nombreuses applications : ils peuvent servir de base pour la création d'outils informatiques automatisés ou encore être intégrés dans des logiciels servant de support au diagnostic. La qualité des résultats de telles applications dépend de la qualité du modèle utilisé. C'est pourquoi nous attachons une attention particulière à la validation de notre travail, alors même qu'il n'existe pas de mesure directe pour l'évaluation, et qu'il faut utiliser des métriques indirectes. Nous nous sommes intéressés à des outils pour la modélisation 3D, particulièrement aux techniques de correspondance entre maillages. Nous présentons une méthode pour transformer des maillages bruts directement créés à partir de tomographies en nouveaux maillages représentant les mêmes os tout en définissant des relations de correspondance. Une fois définies, ces relations rendent possibles de nombreuses applications, qui permettent une validation supplémentaire des correspondances. Nous présentons plusieurs applications. La variabilité de la forme des os est analysée à l'aide d'outils statistiques tels que l'Analyse en Composantes Principales (ACP) ainsi qu'un outil basé sur les Processus Gaussiens. Les capacités d'adaptation du modèle ACP à de nouvelles formes sont utilisées pour définir des relations de correspondance avec une seconde base de données. Nous proposons également une méthode pour transférer simplement des systèmes de coordonnées ou tout autre point remarquable défini pour quelques exemples vers le reste de la base de données. Une telle application est utile pour des études biomécaniques de mouvement du poignet. Finalement, dans une dernière étape, nous nous sommes intéressés à la modélisation des mouvements des os du poignet à l'aide d'un modèle paramétrique basé sur des prédicteurs significatifs et facilement mesurables.